===== **PHYSICS** =====

Relaxation Spectra of Polymers and Their Relation to the Deformation Mode

V. I. Irzhak

The concept of spectra of relaxation times is commonly used to characterize the viscoelastic behavior of polymers. For a given spectrum with the parameters related to structural features of the polymer system, it is usually thought that the relaxation characteristics can be predicted under virtually any experimental conditions [1, 2]. At the same time, it is well known that the relaxation spectra of, for example, the Rouse chain are different for the strain and stress relaxation modes [2]: the time correlation function for the chain length varies in time as

$$\sum_{p = 1, 3, \dots} p^{-2}\exp\left(-\frac{t}{\tau_{\mathrm{p}}}\right),$$

whereas stress relaxation is determined by the sum

$$\sum_{p = 1, 2, \dots} \exp\left(-\frac{t}{\tau_{\mathrm{p}}}\right).$$

Hence, the spectra of relaxation times (pre-exponential factors) for the same chain are different for these two cases, although they have the same set of relaxation times τ_{p}.

In this paper, we analyze the effect of the deformation mode on the relaxation spectrum of the modified Rouse chain [3, 4].

The chain is modeled by n frictional elements connected in series by $n - 1$ elastic elements characterized by elastic modulus E. At the initial moment of time, force $F(0)$ is applied to the chain end via the similar elastic spring. Relaxation in the system causes a stress drop at this spring; that is, stress relaxation occurs. If the force applied at the initial instant is absent further on, there is a relaxation of the chain length (strain). The chain structure is characterized by the values of friction coefficients for each link of the chain: for the ith link,

the relaxation time is specified as $\tau_i = \dfrac{\eta_i}{E}$.

Institute of Problems of Chemical Physics,
Russian Academy of Sciences,
Chernogolovka, Moscow oblast, 142432 Russia

The dynamics of the model are described by the set of differential equations [1–4] involving the variation in coordinates s_i of the links and force F applied to the first link. Initial conditions, namely, $s_i(0)$ and $F(0) = F_0$, are arbitrary. A solution to the set can be found both as function $F(t)$ and in the form $L(t) = s_n - s_1$, i.e., as the change in the chain length. The solution is represented as the series of exponentials

$$F = F_0\sum_{i = 1}^{n} f_i\exp\{-p_i t\}, \tag{1}$$

$$L = L_0\sum_{i = 1}^{n} h_i\exp\{-p_i t\} \tag{2}$$

and is determined by the roots $z_i = \tau_i p_i$ of the corresponding polynomial D_n [3, 4] related to the Rouse determinant (3)

$$B_n = \begin{vmatrix} z_1 - 2 & 1 & 0 & 0 \dots 0 & 0 & 0 \\ 1 & z_2 - 2 & 1 & 0 \dots 0 & 0 & 0 \\ 0 & 1 & z_3 - 2 & 1 \dots 0 & 0 & 0 \\ \hdotsfor{6} \\ 0 & 0 & 0 & 0 \dots 1 & z_{n-1} - 2 & 1 \\ 0 & 0 & 0 & 0 \dots 0 & 1 & z_n - 1 \end{vmatrix}$$

$$= (z_1 - 2)B_{n-1} - B_{n-2}, \tag{3}$$

as $D_n = z_1 B_n$ for the case of stress relaxation, and $D_n = (z_1 - 1)B_{n-1} - B_{n-2} = B_n + B_{n-1} = 0$ for the case of strain.

As was shown in [3, 4], B_n can be easily calculated using the recurrence relation

$$B_1 = z_n - 1,$$

$$B_2 = (z_{n-1} - 2)B_1 - 1,$$

$$B_3 = (z_{n-2} - 2)B_2 - B_1,$$

$$\dots, \tag{4}$$

$$B_i = (z_i - 2)B_{i-1} - B_{i-2},$$

$$\dots,$$

$$B_n = (z_1 - 2)B_{n-1} - B_{n-2}.$$

Table 1. Initial values of kth time derivatives of stress and strain $r_i = \tau_i^{-1}$; $\quad q = 1 - \dfrac{Eh}{F_0}$; $\quad h = \dfrac{L_0}{n-1}$

k	$\dfrac{F^{(k)}(0)}{F_0}$	$\dfrac{L^{(k)}(0)}{L_0}$
0	1	1
1	$-r_1 q$	$-\dfrac{r_1 + r_n}{n-1}$
2	$2r_1^2 q$	$\dfrac{r_1^2 + r_n^2}{n-1}$
3	$-r_1^2(4r_1 + r_2)q$	$-\dfrac{r_1^2(r_1 + r_2) + r_n^2(r_{n-1} + r_n)}{n-1}$
4	$2r_1^2(4r_1^2 + 2r_1 r_2 + r_2^2)q$	$\dfrac{1}{n-1}[r_1^2(r_1^2 + 2r_1 r_2 + 2r_2^2) + r_n^2(2r_{n-1}^2 + 2r_{n-1}r_n + r_n^2)]$
5	$-2r_1^2(8r_1^3 + 8r_1^2 r_2 + 4r_1 r_2^2 + r_2^3 + r_2^2 r_3)q$	$-\dfrac{1}{n-1}[r_1^2(r_1^3 + 3r_1^2 r_2 + 5r_1 r_2^2 + 4r_2^3 + r_2^2 r_3) + r_n^2(r_{n-2}r_{n-1}^2 + 4r_{n-1}^3 \, 5r_{n-1}^2 r_n$ $+ \, 3r_{n-1}r_n^2 + r_n^3)]$

It is clear that factors p_i of the exponentials are uniquely related to τ_i, i.e., to the structure and length n of the chain.

Thus, the set of relaxation times for the chain $\lambda_i = p_i^{-1}$ is independent of the deformation mode.

To determine pre-exponential factors f_i and h_i, it is necessary to take into account the initial state of the chain. Indeed, to find n coefficients, we must solve the set of n equations for the initial values $F^{(k)}(0)$ and $L^{(k)}(0)$ of the kth time derivatives of F and L

$$F(0) = F_0 \sum_{j=1}^{n} f_i,$$

$$F^{(1)}(0) = F_0 \sum_{j=1}^{n} p_j f_j,$$

$$F^{(2)}(0) = F_0 \sum_{j=1}^{n} p_j^2 f_j,$$

$$\dots,$$

$$F^{(k)}(0) = F_0 \sum_{j=1}^{n} p_j^k f_j,$$

$$\dots,$$

$$F^{(n)}(0) = F_0 \sum_{j=1}^{n} p_j^n f_j;$$

$$L(0) = L_0 \sum_{j=1}^{n} h_i,$$

$$L^{(1)}(0) = L_0 \sum_{j=1}^{n} p_j h_j,$$

$$L^{(2)}(0) = L_0 \sum_{j=1}^{n} p_j^2 h_j,$$

$$\dots,$$

$$L^{(k)}(0) = L_0 \sum_{j=1}^{n} p_j^k h_j,$$

$$\dots,$$

$$L^{(n)}(0) = L_0 \sum_{j=1}^{n} p_j^n h_j. \tag{5}$$

Table 1 presents the values of these derivatives for the first five terms of these series. We can see that these values depend not only on the corresponding relaxation times but, in the case of the relaxation mode (first column), on the chain strain $h = |x_i - x_{i-1}| = \dfrac{L(0)}{n-1}$ and the
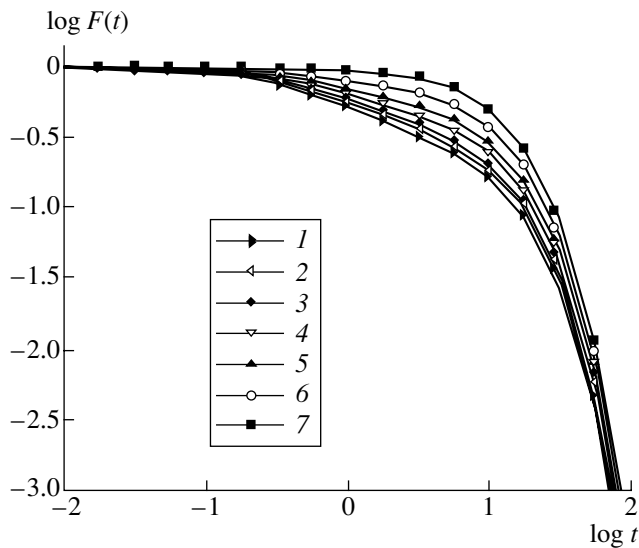
Fig. 1. Stress relaxation curves for different initial strains: (*1*) 0, (*2*) 0.05, (*3*) 0.1, (*4*) 0.2, (*5*) 0.3, (*6*) 0.5, and (*7*) 0.8.
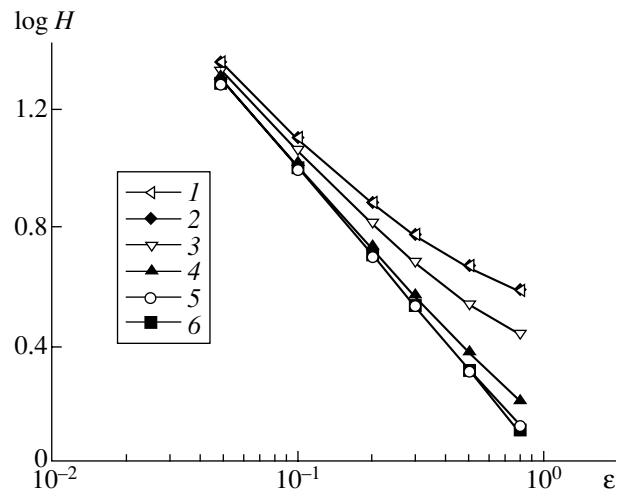

Fig. 2. Relative elastic modulus versus initial strain for different time points (in arbitrary units): (*1*) 0.01, (*2*) 0.0562, (*3*) 0.3162, (*4*) 0.5625, (*5*) 10, and (*6*) 56234.

$\dfrac{E}{F_0}$ ratio as well. This means that the coefficients f_i determined from the solution of system (5) for F should depend on these parameters. Therefore, the spectrum of relaxation times characterizes not only the chain structure, as is typical for a set of relaxation modes, but also strain in the initial state. For the strain relaxation mode, the characteristic features of the spectrum are independent of the initial state but are uniquely determined by the chain length and by the relaxation parameters of chain links. This is also clear from Table 1 (second column). Thus, for the deformation mode (relaxation of the chain length), the relaxation spectrum uniquely characterizes the system structure through the set of relaxation times and pre-exponential factors. For the stress relaxation mode, the structure is characterized only by the set of relaxation times. In this case, the pre-exponential factors are not the statistical weight of the corresponding mode of motion.

It is clear that the data on stress relaxation for the two-stage deformation of polymers can be considered first of all from this viewpoint (see, e.g., [5, 6]). Theory based on the reptation model [2] ignores those circumstances.

As an example, let us determine the relaxation behavior for the model five-link Rouse chain. Table 2 presents the parameters λ_i and f_i characterizing the spectrum of relaxation times for the five-link chain with different strains (all τ_i are equal to unity). We see that the characteristics of the spectrum change considerably with increasing strains, and negative coefficients arise. It is evidently unreasonable to consider this set of numbers as certain structural characteristics. The curves for the strain relaxation for different initial strains are shown in Fig. 1. The characteristic feature of these curves is a significant increase in the length of the high-elasticity plateau with increasing initial strains. Figure 2 demonstrates that the dependence of the relative value of the relaxation elastic modulus $H(t, \varepsilon) = \dfrac{F(t, \varepsilon)}{\varepsilon F(t, 0)}$ on strain ε varies with time. Although the form of these curves differs from that observed in experiment [6], the existence of time dependence does not agree with the theoretical predictions [2].

Therefore, analyzing different loading regimes for polymers, we should not neglect the dependence of the

Table 2. Parameters of the relaxation spectrum of the five-link Rouse chain corresponding to the stress relaxation mode. The initial strain is indicated in brackets

Mode no.	λ_i	$f_i(0)$	$f_i(0.05)$	$f_i(0.1)$	$f_i(0.2)$	$f_i(0.3)$	$f_i(0.5)$	$f_i(0.8)$
1	12.346	0.356	0.401	0.446	0.535	0.625	0.804	1.073
2	1.449	0.301	0.268	0.234	0.168	0.102	−0.031	−0.229
3	0.583	0.208	0.205	0.203	0.198	0.193	0.183	0.168
4	0.353	0.106	0.098	0.089	0.072	0.055	0.022	−0.029
5	0.271	0.029	0.028	0.027	0.026	0.025	0.022	0.018

relaxation spectrum [or, more precisely, of the form of function $F(t)$] on the deformation conditions.

REFERENCES

1. G. V. Vinogradov and A. Ya. Malkin, *Rheology of Polymers* (Khimiya, Moscow, 1977).

2. M. Doi and S. Edwards, *The Theory of Polymer Dynamics* (Clarendon, Oxford, 1986; Mir, Moscow, 1998).

3. V. I. Irzhak, Dokl. Akad. Nauk **379**, 613 (2001) [Dokl. Phys. **46**, 544 (2001)].

4. V. I. Irzhak, Dokl. Akad. Nauk **380**, 31 (2001) [Dokl. Phys. **46**, 609 (2001)].

5. C. M. Vrentas and W. W. Graessley, J. Rheol. **26** (4), 359 (1982).

6. F. A. Morrison and R. G. Larson, J. Polym. Sci., Part B: Polym. Phys. **30** (9), 943 (1992).

Translated by K. Kugel

Theory of Longitudinal Plasma Waves in the Electron–Positron Plasma

G. N. Kichigin

Presented by Academician G.A. Zherebtsov March 4, 2002

Received March 13, 2002

The electron–positron plasma has recently attracted considerable interest, because it is a source of high-intensity electromagnetic radiation inherent in many cosmic objects such as the magnetospheres of pulsars, active galactic nuclei, including the center of the Galaxy, the early Universe, etc. The origin of observed radiation is assumed to be substantially determined by the oscillation and wave properties of the electron–positron plasma. In this study, we analyze the characteristics of nonlinear longitudinal plasma waves propagating in a cold collisionless electron–positron plasma.

Theoretical investigations of stationary waves in a plasma were summarized in detail in fundamental work [1], where the authors considered plane waves in an unbounded plasma consisting of cold electrons and infinitely heavy ions at rest.

The basic feature of the electron–positron plasma is that the mass and absolute value of the charge of an electron are equal to the respective values for an ion. Therefore, the ion and electron components must be considered simultaneously. Moreover, a definite symmetry can be expected. Thus, the problem of the propagation of plasma waves is examined similarly to [1] but with allowance for the motion of ions in a wave. Waves whose electric field and displacements of particles are parallel to the wavevector are called longitudinal waves. We consider the propagation of steady-state plane waves along the x axis in the absence of an external magnetic field.

It is convenient to consider a steady-state wave in the wave reference frame, where the problem is stationary and all desired quantities depend only on the coordinate x. To solve the problem, it is necessary to apply Maxwell's equations, the relativistic equation of motion, and continuity equations for electrons and ions.

We seek a solution to these equations in the form of a periodic alternating potential wave. The electric field has extrema at points that lie between neighboring

maxima and minima of the potential and are spaced by the wavelength λ. It follows from the Maxwell equation for the electric field,

$$\frac{dE(x)}{dx} = 4\pi e[(n_i(x) - n_e(x))], \tag{1}$$

that the ion density $n_i(x)$ at these points is equal to the electron density $n_e(x)$. Let $x = 0$ be an extremal point. Then, $n_i(0) = n_e(0) = n$ and $E(0) = E_0$, where E_0 is the extremal electric field. Without loss of generality, the wave potential $\varphi(x)$ at extrema is taken to be equal to zero; i.e., $\varphi(0) = 0$.

It follows from the continuity equations for electrons $\dfrac{d(n_e v_e)}{dx} = 0$ and ions $\dfrac{d(n_i v_i)}{dx} = 0$ that $n_i(x)v_i(x) = C_1$ and $n_e(x)v_e(x) = C_2$, where $v_e(x)$ and $v_i(x)$ are the velocity of electrons and ions, respectively, and constants $C_1 = nv_i(0)$ and $C_2 = nv_e(0)$ are found at $x = 0$, where $n_i(0) = n_e(0) = n$. Let $v_e(0) = v_i(0)$. Then, the total current at all points of the wave profile is equal to zero:

$$e[n_i(x)v_i(x) - n_e(x)v_e(x)] = 0.$$

In this case, as in [1], the perturbed magnetic field is absent for longitudinal waves.

For a cold plasma in the absence of a magnetic field, the motion of electrons and ions in the electric field of the wave can be described in the one-particle approximation by the relativistic equations of motion, which have the following form in the wave reference frame:

$$
\begin{aligned}
v_e(x)\frac{dp_e(x)}{dx} &= mc^2\frac{d\gamma_e(x)}{dx} = -eE(x), \\
v_i(x)\frac{dp_i(x)}{dx} &= mc^2\frac{d\gamma_i(x)}{dx} = eE(x),
\end{aligned}
\tag{2}
$$

where p_e and p_i are the momenta of electrons and ions, respectively; m and e are the mass and absolute value of

Institute of Solar–Terrestrial Physics, Siberian Division,
Russian Academy of Sciences, Irkutsk, 664082 Russia
E-mail: king@iszf.irk.ru

the charges of particles, respectively;

$$\gamma_e(x) = \frac{1}{\sqrt{1 - \beta_e^2(x)}}, \quad \gamma_i(x) = \frac{1}{\sqrt{1 - \beta_i^2(x)}},$$

$$\beta_e(x) = \frac{v_e(x)}{c}, \text{ and } \beta_i(x) = \frac{v_i(x)}{c}.$$

Substituting the relation $E(x) = -\dfrac{d\varphi(x)}{dx}$ into Eq. (2), we obtain the laws of energy conservation for ions and electrons in the form

$$mc^2\gamma_i(x) + e\varphi(x) = C_3, \quad mc^2\gamma_e(x) - e\varphi(x) = C_4, \quad (3)$$

where constants C_3 and C_4 can be found by determining the energy and potential at $x = 0$, where $\varphi(0) = 0$ and $v_e(0) = v_i(0) = u$. As a result, $C_3 = C_4 = mc^2\gamma$, where $\gamma = \dfrac{1}{\sqrt{1 - \beta^2}}$ with $\beta = \dfrac{u}{c}$. The problem under consideration obviously has physical meaning only for velocities u less than the speed of light.

Let us substitute the electron $n_e(x) = \dfrac{nu}{v_e(x)}$ and ion $n_i(x) = \dfrac{nu}{v_i(x)}$ densities into Eq. (1), then multiply this equation by $E(x)$, and express $\dfrac{eE(x)}{v_e(x)}$ and $\dfrac{eE(x)}{v_i(x)}$ from Eqs. (2) in terms of the momenta of electrons and ions. As a result, we arrive at the relation

$$\frac{d}{dx}\{E^2 - 8\pi nu[p_e(x) + p_i(x)]\} = 0,$$

from which we find one more conservation law:

$$[E(x)]^2 - 8\pi nu[p_e(x) + p_i(x)] = C_5, \quad (4)$$

where constant $C_5 = E_0^2 - 16\pi n\gamma mu^2$ is found at $x = 0$. The set of Eqs. (1)–(4) solves the problem in question.

We introduce the dimensionless coordinate $\xi = \dfrac{1}{c}x\omega_p\sqrt{\dfrac{\beta}{2}}$, where $\omega_p = \sqrt{\dfrac{8\pi e^2 n}{m}}$ is the plasma frequency of linear waves in electron–positron plasma, and dimensionless potential $\psi(\xi) = \dfrac{\varphi(x)}{mc^2}$. By expressing the momenta of electrons and ions in terms of the potential from Eqs. (3), Eq. (4) is represented in dimensionless variables as

$$V(\psi) = \varepsilon - \frac{1}{2}\left[\frac{d\psi(\xi)}{d\xi}\right]^2$$
$$= 2\beta\gamma - \sqrt{\beta^2\gamma^2 - \psi(2\gamma - \psi)} - \sqrt{\beta^2\gamma^2 + \psi(2\gamma + \psi)}, \quad (5)$$

where $\varepsilon = \dfrac{1}{2}\left(\dfrac{d\psi}{d\xi}\right)_0^2$ is the dimensionless energy density of the electric field at $\xi = 0$ where $\psi = 0$ and the electric field is maximal.

The potential and electric field as functions of the coordinate can be determined from Eq. (5). To appreciate the general properties of a desired solution, it is convenient to apply the formalism that was developed in classical mechanics for analyzing the motion of particles in a potential well [2]. In the case under consideration, the function $V(\psi)$, which is the dimensionless energy density of the electric field, obviously satisfies the equation $\dfrac{d^2\psi}{d\xi^2} = -\dfrac{dV}{d\psi}$, where $V(\psi)$ is the potential energy of the system for the problem of the motion of a unit-mass particle, whereas ψ and ξ are the coordinate and time, respectively.

The function $V(\psi)$ is defined in the interval $\psi_-^* \le \psi \le \psi_+^*$, where $\psi_-^* = 1 - \gamma$ and $\psi_+^* = \gamma - 1$. The appearance of the limiting values ψ_-^* and ψ_+^* can be understood by analyzing the motion of particles in the potential wave. If the oscillation amplitude exceeds the limiting values, the wave turns over, which gives rise to multiflow motion. Therefore, the laminar motion of particles, which is necessary for the existence of the steady-state wave under consideration, is violated.

Thus, for potential amplitudes exceeding ψ_-^* or ψ_+^*, the function $V(\psi)$ is indefinite, as follows from the analysis of its existence area, and the propagation of nonlinear laminar plasma waves is impossible as is indicated by an analysis of the motions of particles in the potential wave.

The plot of the function $V(\psi)$ is a well symmetric about the point $\psi = 0$. The maximum well depth is obviously determined by the values ψ_-^* and ψ_+^*. Denoting $V(\psi) = \varepsilon_m$ for $\psi = \psi_-^*$ or $\psi = \psi_+^*$, we can obtain from Eq. (5) the limiting value of the parameter ε and, therefore, the limiting value of the electric field amplitude in the wave:

$$\varepsilon_m = 2\sqrt{\gamma - 1}(\sqrt{\gamma + 1} - \sqrt{\gamma}). \quad (6)$$

From Eq. (6), ε_m is determined for nonrelativistic waves ($\beta \ll 1$, $\gamma \approx 1 + \dfrac{\beta^2}{2}$) as $\varepsilon_m \approx \dfrac{\beta}{2}$ corresponding to the dimensional formula

$$\frac{E_0^2}{8\pi} \approx \frac{n_0 mu^2}{2}.$$

For relativistic waves ($\beta \approx 1$, $\gamma > 1$), we have

$$\varepsilon_m \approx \sqrt{\frac{\gamma - 1}{\gamma}}. \quad (7)$$

The parameter ε is the total energy of a particle moving in the potential well under consideration. It is known that particle motion can be qualitatively determined from the plot of the potential energy of the system; i.e., the desired function $\psi = \psi(\xi)$ can be found from the form of $V(\psi)$. The analysis of the function $V(\psi)$ indicates that, with increasing parameter γ, the potential-well profile changes so that it becomes virtually square for $\gamma > 5$. In a square well, the particle moves with constant velocity. Therefore, for $\gamma > 5$, when the well shape is close to square, the potential has a sawtooth shape, and the electric field in the wave has the form of alternating positive- and negative-polarity squares of the same amplitude and shape.

In order to determine the amplitude of the potential-wave oscillations, we note that the total swing of the potential is determined from Eq. (5) at $V(\psi) = \varepsilon$. For low wave velocities ($\beta \ll 1$, $\gamma \approx 1 + \dfrac{\beta^2}{2}$, $\varepsilon \approx \dfrac{\beta}{2}$), the oscillation amplitude is small. Let us find the shape of the potential well for small oscillations. Expanding the right-hand side of Eq. (5) near $\psi = 0$ ($\psi \ll \beta \ll 1$) for given ε and β, we obtain

$$V(\psi) \approx \frac{\psi^2}{\beta^3}. \tag{8}$$

Therefore, small oscillations occur in a parabolic potential well. The amplitude of small harmonic oscillations is determined from the relation $\varepsilon = V(\psi)$: $\psi_+ \approx \psi_- \approx \dfrac{\beta^2}{\sqrt{2}}$.

For relativistic waves ($\gamma \gg 1$), when the amplitude of oscillations is close to the maximum ($\varepsilon \approx \varepsilon_m$), the periodic wave becomes strongly nonlinear. In this case, from the equation

$$[\beta^2\gamma^2 - \psi(2\gamma - \psi)]^{1/2}$$
$$+ [\beta^2\gamma^2 + \psi(2\gamma + \psi)]^{1/2} - 2\beta\gamma + \varepsilon = 0$$

at given parameters γ and ε, the absolute value of the amplitude of the potential oscillations is determined as

$$\psi^m = \frac{(2\beta\gamma - \varepsilon)}{2} \sqrt{\frac{4\beta\gamma\varepsilon - \varepsilon^2}{4 + 4\beta\gamma\varepsilon - \varepsilon^2}}.$$

Therefore, the amplitudes are $\psi_+ = \psi^m$ and $\psi_- = -\psi^m$. Substituting $\varepsilon = \varepsilon_m$ from Eq. (6) into the formula for ψ^m, we obtain $\psi^m = \gamma - 1$. Thus, the form and amplitude of the oscillations of the potential and the electric field of the wave have been found. The spatial period of

the oscillations of the potential and electric field in the wave is found in the wave reference frame as

$$\lambda = \frac{2c}{\sqrt{\beta}\,\omega_p} \int_{\psi_-}^{\psi_+} \frac{d\psi}{\sqrt{\varepsilon - V(\psi)}},$$

where $V(\psi)$ is determined from Eq. (5).

One more reference frame in the problem moves with the velocity u with respect to the wave reference frame. We refer to this frame as the laboratory coordinate system, where the wave moves with the velocity u in the negative direction of the x axis and has the wavelength λ^L, and the period of oscillations of the potential and electric field in the wave is $T = \dfrac{u}{\lambda^L}$.

The wave number $k = \dfrac{2\pi}{\lambda}$ and frequency are transformed as $k^L = \gamma k$ and $0 = \gamma(\omega + uk^L)$, where k^L and $\omega = \dfrac{2\pi}{T}$ are, respectively, the wave number and frequency of the wave in the laboratory coordinate system. The frequency in the wave reference frame is reasonably taken to be equal to zero. Therefore, $u = -\dfrac{\omega}{k^L}$ is the phase velocity of the wave in the laboratory coordinate system.

The plasma is quasi-neutral at $x = 0$ in the wave reference frame and, therefore, in all inertial reference frames including the laboratory coordinate system. It is remarkable that ions and electrons at this point are at rest in the laboratory coordinate system. Therefore, when a wave and corresponding field disturbances are absent, all electrons and ions of the plasma are at rest in the laboratory coordinate system, plasma is quasi-neutral, and particle density is $n_0 = \dfrac{n}{\gamma}$.

Thus, in the laboratory coordinate system, n_0 is the density of the plasma undisturbed by the wave, the wave has the frequency ω, wave number k^L and phase velocity $u = -\dfrac{\omega}{k^L}$. It follows from Eq. (7) that the limiting electric field in the wave with $\gamma \gg 1$ in the laboratory coordinate system is $(E_0)_m \approx \dfrac{mc}{e}\omega_{p0}\sqrt{\gamma}$, where $\omega_{p0} = \sqrt{\dfrac{8\pi n_0 e^2}{m}}$ is the plasma frequency in the laboratory coordinate system. This $(E_0)_m$ value coincides with the limiting electric field found in [1], where the problem of the propagation of longitudinal waves in a plasma was solved in the laboratory coordinate system. The wave frequency in the laboratory coordinate sys-

tem is found from the formula $\omega = \dfrac{2\pi u \gamma}{\lambda}$. We obtain the relation

$$\omega = \omega_{p0} \frac{\pi(\beta\gamma)^{3/2}}{\displaystyle\int_{\psi_-}^{\psi_+} \frac{d\psi}{\sqrt{\varepsilon - V(\psi)}}}. \tag{9}$$

The frequency ω can be approximately estimated in two limiting cases, where $\gamma \approx 1$ and $\gamma \gg 1$. All calculations and estimations will be made for plasma waves with the maximum amplitude, i.e., for $\varepsilon = \varepsilon_m$. For small oscillations ($\gamma \approx 1$, $\beta \ll 1$), when $\varepsilon_m \approx \dfrac{\beta}{2}$, $\psi_+ \approx \psi_- \approx \dfrac{\beta^2}{\sqrt{2}}$, the function $V(\psi)$ is determined by Eq. (8), the integral entering into Eq. (9) can be calculated, and we find that the oscillation frequency is equal to the Langmuir frequency, i.e., $\omega = \omega_{p0}$.

For relativistic plasma waves ($\beta \approx 1$, $\gamma \gg 1$), the integral in Eq. (9) can be estimated by taking into account the fact that the potential well is of an almost square shape for $\gamma > 5$. Therefore, for the limiting amplitudes of the electric field, the radicand in Eq. (9) $\varepsilon_m - V(\psi) \approx 1$ for almost all ψ values, and Eq. (9) yields the estimate

$$\omega \approx \frac{\omega_{p0}\pi(\beta\gamma)^{3/2}}{\psi_+^* - \psi_-^*},$$

which gives $\omega \approx \dfrac{1}{2}\pi\omega_{p0}\sqrt{\gamma}$; i.e., the wave frequency increases as $\gamma^{1/2}$ with γ and the wavelength decreases. Thus, as the phase velocity of a longitudinal plasma wave tends to the speed of light, the wave frequency increases infinitely. This dependence of the frequency on γ is opposite to the behavior $\gamma \sim \gamma^{-1/2}$ obtained in [1], where the motion of ions in the wave was ignored.

In summary, analyzing the properties of high-amplitude plasma waves in the electron–positron plasma, we determined the wave profile by qualitative consideration and found the frequency and wavelength as well as the amplitudes of the potential and electric field of the wave. The dependence of the wave frequency on the wave velocity is most surprising: for $\gamma > 1$, the frequency of high-amplitude longitudinal plasma waves is always higher than the plasma frequency typical for the harmonic linear plasma oscillations. The results are important as an insight into the processes of the propagation of high-amplitude plasma waves in the electron–positron plasma.

REFERENCES

1. A. I. Akhieser and R. V. Polovin, Zh. Éksp. Teor. Fiz. **30**, 915 (1956) [Sov. Phys. JETP **3**, 696 (1956)].

2. L. D. Landau and E. M. Lifshitz, *Mechanics* (Nauka, Moscow, 1965; Pergamon Press, Oxford, 1976).

Translated by R. Tyapaev

=== **PHYSICS** ===

Dynamics of a Cavitation Bubble with Allowance for Translational Motion

I. M. Margulis and M. A. Margulis

Presented by Academician Yu. V. Gulyaev April 12, 2002

Received April 15, 2002

Calculations on the basis of ordinary equations describing cavitation-bubble dynamics show that, under certain conditions, the maximum temperature T_{max} in the bubble at the instant of the largest contraction can be as high as a few thousand degrees [1, 2]. However, at least 19 groups of experimental data on multibubble cavitation reveal that high T_{max} values are not achieved in bubbles and that the mechanism of sonoluminescence (SL) and sonochemical reactions is electric rather than thermal [3]. At the same time, high T_{max} values can be obtained under specific conditions, e.g., when a bubble contracts in a single-bubble chamber [4, 5] or when a spherically symmetric laser bubble contracts [6]. In this case, luminescence occurs only if the bubbles in question are at rest. If a single bubble is entrained by a liquid flow or if a laser bubble moves toward a solid wall, this luminescence disappears, although ordinary equations of cavitation dynamics suggest no changes in this case. We assumed that in order to adequately describe the dynamics of a bubble, it was necessary to take into account its translational motion, and we obtained the corresponding set of equations in the form

$$
r\ddot{r}\left(1 - \frac{\dot{r}}{c_0}\right) + \frac{3}{2}\dot{r}^2\left(1 - \frac{\dot{r}}{3c_0}\right) + \frac{u^2}{4} + \frac{r\dot{u}}{6} + \frac{\dot{r}u}{2}
$$

$$
= \frac{1}{\rho_L}\left(1 - \frac{\dot{r}}{c_0}\right)\left[p_\infty\left(t + \frac{r}{c_0}\right) - p_b(t)\right] + \frac{r}{\rho_L c_0}\frac{dp_b(t)}{dt}, \quad (1)
$$

$$
\mathbf{u} = \frac{1}{V}\left(-\frac{2}{\rho_L}\int_0^t (\nabla p_\infty V + 4\pi r\mu\mathbf{u})dt + \mathbf{u}(0)V(0)\right), \quad (2)
$$

$$
p_b(t) = (p_g + p_v) + \frac{2\sigma}{r} - \frac{4\mu\dot{r}}{r} - \frac{\mu u}{3r}, \quad (3)
$$

where t is time; r and V are the radius and volume of the bubble, respectively; $\dot{r}$ and u are the radial and transla-

tional velocities, respectively; p_∞ and p_b are the pressure in a liquid and in the bubble, respectively; ρ_L, μ, and σ are the density, viscosity, and surface tension of the liquid, respectively; and c_0 is the speed of sound in the liquid without bubbles. According to [7], the sum of the gas and vapor pressures is

$$
p_g + p_v = \left(p_{g0} + \frac{2\sigma}{r_0}\right)\left(\frac{r_0^3}{r^3 - b_1^3}\right)^\gamma + p_s. \quad (4)
$$

Here, r_0 is the initial radius; γ is the heat-capacity ratio; p_{g0} and p_s are, respectively, the gas pressure at $t = 0$ and the saturated-vapor pressure at constant temperature T_∞ of the liquid; and $b_1^3 = \frac{3nb}{4\pi}$, where b and n are the van der Waals constant and the number of moles of gas, respectively. However, when Eq. (4) is used, T_{max} is independent of the temperature of the liquid, T_∞, which contradicts experimental data. Formula (4) is valid only in the case of bubble expansion. In contrast, when the bubble rapidly contracts, evaporation and condensation have no time to occur, and the vapor behaves as a gas. Therefore, we have [8]

$$
p_g + p_v = \left[\left(p_{g0} + \frac{2\sigma}{r_0}\right)\left(\frac{r_0}{R_m}\right)^3 + p_s\right]\left(\frac{R_m^3}{r^3 - b_1^3}\right)^\gamma. \quad (5)
$$

In this case, the dependence of T_{max} on T_∞ is in agreement with experimental data, and the temperature T_{max} decreases by a factor of about $\frac{p_s + p_g(R_m)}{p_g(R_m)}$.

When a cavitation bubble moves at an antinode of a standing wave, the bubble is at rest; i.e., $u = 0$. In this case, the set of Eqs. (1)–(3) reduces to one Keller–Miksis equation or, in the limit of incompressible liquid ($c_0 \longrightarrow \infty$), to the Rayleigh–Plesset equation [1]. Further, when the bubble radius is constant and $\mu = 0$, $u(t) \approx 2u_\infty(t)$ and the set of Eqs. (1)–(3) reduces to the ordinary equation of motion for a massless rigid ball [9]. In investigating high-energy cavitation effects, one
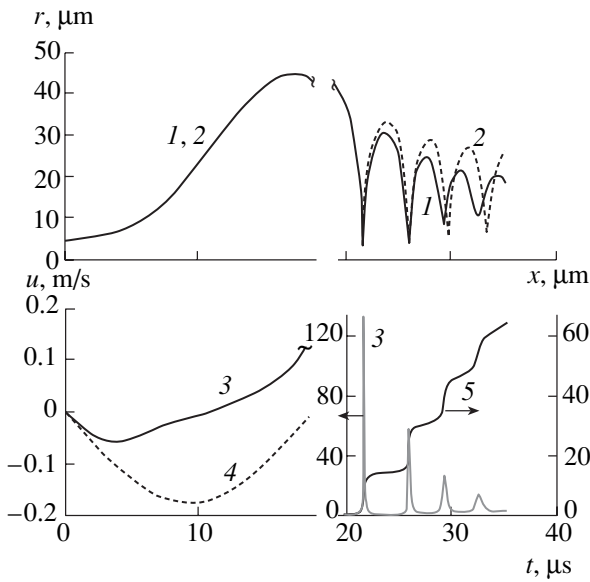
Fig. 1. Numerical results for oscillations of a vapor–gas bubble of initial radius $r_0 = 4.5 \, \mu m$ in water ($c = 1500 \, \text{m s}^{-1}$, $\rho_L = 10^3 \, \text{kg m}^{-3}$, $\sigma = 73 \, \text{mN m}^{-1}$, $\mu = 10^{-3} \, \text{kg s}^{-1} \, \text{m}^{-1}$) at a temperature of 293 K ($p_s = 0.025$ atm) in a traveling harmonic plane wave ($p_h = 1$ atm, $p_m = 1.325$ atm, $\omega = 2\pi \times 26.5$ kHz): (*1, 2*) time dependence of the cavitation-bubble radius, respectively, without and with allowance for the translational motion; (*3, 4*) time dependence of the translational velocity, respectively, with and without allowance for the radial motion; and (*5*) time dependence of the translational displacement. In the lower right part of the figure, we changed the ordinate scale and shifted the zero value of *u* along the vertical.

considers the fast contraction of a bubble by a factor of 10 to 20 in radius (T_{max} can be high only under such conditions). In this case, its translational momentum remains constant and velocity *u*, as well as the energy of the translational motion, increases in inverse proportion to $\sim V^{-1}$ by a factor of 10^3 to 10^4, and part of the energy of its radial motion is effectively converted into the energy of its translational motion. Therefore, temperature T_{max} is expected to decrease.

In order to describe the translational motion of an oscillating bubble under the action of an external pressure gradient, the oscillation-period-averaged (Bjerkness) force acting on the bubble is usually defined as [10]

$$F_{\text{B}} = -\langle \nabla p_{\infty}(x, t) V(t) \rangle_t. \tag{6}$$

Dividing F_{B} by the period-averaged added mass $\dfrac{\rho_L \langle V \rangle}{2}$, one obtains the bubble acceleration $\dfrac{\langle F_{\text{B}} \rangle}{\langle m \rangle}$. However, this approach is not applicable to the actual pulsations of the bubble if its radius and, hence, the added mass change, because the average of a ratio is

generally not equal to the ratio of averages; that is,

$$\langle u \rangle = -\frac{2}{\rho_L} \left\langle \frac{1}{V} \left(\int_0^t (\nabla p_{\infty} V) dt \right) \right\rangle$$

$$\neq -\frac{2}{\rho_L} \frac{\langle \nabla p_{\infty}(x, t) V(t) \rangle_t t}{\langle V \rangle_t}; \tag{7}$$

where $\langle u \rangle$ is the translational velocity averaged over a period. It is more correct to determine directly the time dependence of the bubble displacement or, at a constant sound frequency, to determine $u(t)$ according to Eq. (2) and the left-hand side of Eq. (7).

Let a bubble move in the field of a traveling harmonic plane wave. In this case,

$$p_{\infty} = p_h - p_m(\sin \omega t - kx),$$
$$u_{\infty} = -u_m \sin(\omega t - kx), \tag{8}$$

where p_h is the hydrostatic pressure; p_m and $u_m = \dfrac{p_m}{\rho_L c}$ are the amplitudes of the sound pressure and velocity, respectively; ω is the angular frequency; and *c* is the speed of sound in a liquid with bubbles. This speed is one to two orders of magnitude less than c_0 (e.g., $c_0 = 1500 \, \text{m s}^{-1}$ in a liquid without bubbles, whereas *c* reaches 10–100 and 40–100 m s^{-1} theoretically [11] and experimentally [12], respectively). In the case of acoustic oscillations of the bubble, translational and radial oscillations are almost independent, and we have

$$\langle u \rangle \approx u_m \frac{p_m}{\gamma p_h \left(\left(\dfrac{r}{r_{\text{res}}} \right)^2 - 1 \right)}, \tag{9}$$

where $r_{\text{res}} = \dfrac{1}{\omega} \left(\dfrac{3\gamma p_h}{\rho_L} \right)^{1/2}$ is the resonance radius [13]. The bubble moves away from an emitter if $r < r_{\text{res}}$ and to the emitter in the opposite case. We note that, although $F_{\text{B}} = 0$ and $u(0) = 0$, $\langle u \rangle$ is nonzero. This result can be obtained only if we average Eq. (2) over time, whereas the calculation with F_{B} from Eq. (6) would give a result such that the bubble is at rest. In general, the velocity satisfies the condition $\langle u \rangle \ll u_m$, but $\langle u \rangle \sim u_m$ for $r \longrightarrow r_{\text{res}}$.

Figure 1 shows the numerical results obtained for nonlinear oscillations of a vapor–gas bubble in the pressure field (8) when the interplay of the translational and radial motions is and is not taken into account. When the bubble expands, the translational and radial motions are virtually independent (curves *1* and *2* coincide with each other). At the same time, the radial motion considerably affects the translational motion, and the dependence $u(t)$ with allowance for the radial motion differs

considerably from the function $u(t) = -2u_m \sin \omega t$ obtained when the radial motion is ignored (curves *3*, *4*). In particular, in the expansion phase at $r > 33$ μm, the bubble would move toward the emitter (curve *4*) if radial motion were not taken into account; however, the bubble moves in fact away from the emitter (curve *3*).

When the bubble rapidly contracts, the translational momentum remains approximately constant throughout the contraction time, whereas the translational velocity increases sharply, $u \approx u(R_m) \left(\dfrac{R_m}{r} \right)^3$. According to our calculations, u increases from 0.1 m s^{-1} at $r = R_m$ to 135 m s^{-1} at the instant of maximal contraction. When the translational motion is taken into account, T_{max} decreases from 4200 to 2800 K, i.e., by a factor of 1.5. If, instead of the more correct Eq. (5), Eq. (4) is applied to describe bubble contraction, as is usually done, T_{max} decreases from 21 000 to 3900 K, i.e., by a factor of 5.5, when the translational motion is taken into account. Despite a considerable change in $p_g + p_v$, T_{max} changes only slightly when the translational motion is taken into account. The point is that the minimal bubble radius r_m and T_{max} are determined not only by the gas and vapor pressure but also by the velocity of the translational motion. This conclusion is corroborated by calculating the additional extension pressure p_{transl}, which is associated with the translational motion and, under conditions being considered, achieves 80 atm, i.e., is of the same order of magnitude as the maximal pressure of a vapor–gas mixture (180 atm). The calculations for various r_0 and p_m demonstrate that the effect of p_{transl} is so strong that $\dfrac{R_m}{r_m} \leq 14$ even for empty-bubble contraction.

For the same conditions as in Fig. 1, Fig. 2 shows T_{max} and the maximum radial velocity $\dot{r}_{max}$, which were calculated as functions of the sound pressure p_m in traveling wave (8) when translational motion was and was not taken into account. The inclusion of the translational motion leads to a decrease in T_{max} from 7700 to 2800 K (i.e., by nearly a factor of 3), and $\dot{r}_{max}$ decreases from 560 to 140 m s^{-1} (i.e., by nearly a factor of 4). In a liquid containing bubbles, the effect of the speed of sound c on the maximum parameters in the bubble is significant, because, with decreasing c at $p_m = $ const, the velocity u_m and, proportionally, the translational momentum of the bubble increase [see Eq. (8)]. The calculations show that a collapse accompanied by the generation of high T_{max} does not occur for $c \leq 500$ m s^{-1}. The calculations ignored both heat transfer in bubble contraction (it reduces T_{max} approximately by a factor of 2 [14]) and the deviations from the spherical bubble shape upon bubble contraction (this effect also reduces T_{max}). Thus, even if the decrease in the speed of sound in a liquid containing bubbles is disregarded, the maximum
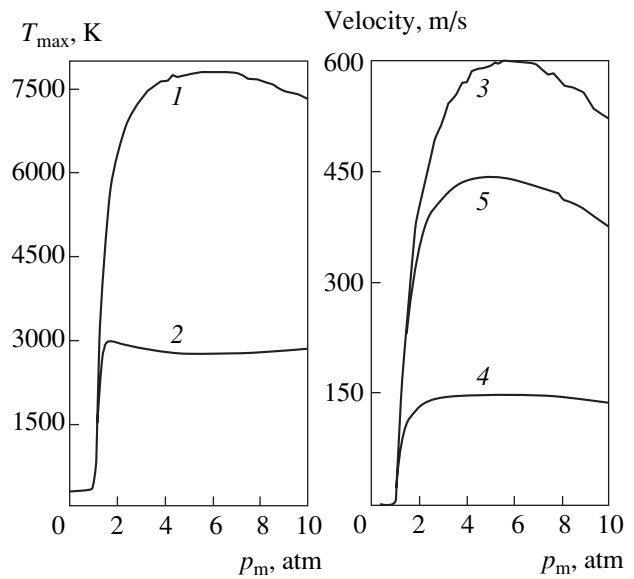
Fig. 2. (*1*, *2*) Maximal temperature, (*5*) the maximum translational velocity, and (*3*, *4*) the radial velocity vs. the amplitude of the sound-wave pressure (the remaining parameters are the same as in Fig. 1). Curves *1* and *3* were obtained by ignoring the translational motion, while curves *2*, *4*, and *5* were calculated with allowance for the translational motion.

temperature in actual cavitation bubbles is bounded as $T_{max} \leq 1000$ K in the field of a traveling wave.

The calculations demonstrate that, for nonlinear bubble oscillations (Fig. 1, curve *5*), the translational motion is jumplike, in contrast to the case of small oscillations, where the translational motion of the bubble with respect to the liquid proceeds smoothly. While expanding, the bubble behaves as if it stopped; in the case of quick contraction, it moves fast with continuously increasing velocity—this is a jump, which is followed by a decrease in u nearly down to zero. The apparent smooth translational motion of bubbles is in fact a sequence of jumps occurring one or a few times per period of acoustic oscillation (for each quick contraction); throughout the remaining time, bubbles are virtually at rest. According to generally accepted concepts, the Bjerkness force $F_B = 0$ for bubbles in the traveling-wave field; that is, the total displacement of the bubble over a period is $\Delta x = 0$. However, the calculations have revealed that $\Delta x \sim 65$ μm (Fig. 1, curve *5*), which is much greater than the amplitude of the incident wave, $\dfrac{p_m}{\rho_L c \omega} = 0.5$ μm. The computed value of $\langle u \rangle = \Delta x \dfrac{\omega}{2\pi} = 1.7$ m s^{-1} corresponds to the experimental values of 1 to 2 m s^{-1} [15].

Thus, we have derived a new set of equations that describes cavitation-bubble dynamics and takes into account the radial and translational motions of a bubble. We have shown that, in the case of quick bubble

contraction, the energy of the radial motion of the bubble is effectively converted into the energy of its translational motion. The apparent smooth translational motion of the nonlinearly oscillating bubble is actually a sequence of jumps that occur once or a few times per period for each quick contraction of bubbles, and bubbles are virtually at rest throughout the remaining time. Upon bubble contraction, the maximum translational velocity can be as high as a few hundred meters per second. The computed period-averaged translational velocity agrees with experimental data.

In the case of nonlinear oscillations of a bubble, its translational motion strongly affects the radial pulsations of the bubble, namely, considerably damps the adiabatic contraction of the bubble and reduces both the maximum temperature T_{max} in the bubble by approximately a factor of 3 (to 2800 K) and the maximum radial velocity by a factor of 4 (to 140 m s^{-1}). With allowance for heat transfer, deviations from the spherical shape upon bubble contraction, and interactions with other bubbles and liquid flows, the maximum temperature T_{max} of the bubble in the case of multibubble cavitation in the field of a traveling wave cannot be higher than 1000 K. Under such conditions, luminescence with a maximum at 5000 K is impossible.

A description of the translational motion of an oscillating bubble with the aid of the period-averaged Bjerkness force can lead to incorrect results even in the case of linear oscillations. It is more appropriate to determine the time dependence of the average displacement or the average velocity of the bubble directly from the proposed set of equations.

REFERENCES

1. M. A. Margulis, *Sonochemistry and Cavitation* (Gordon and Breach, London, 1996), p. 543.
2. M. A. Margulis, Usp. Fiz. Nauk **170** (3), 263 (2000).
3. M. A. Margulis and I. M. Margulis, Ultrason. Sonochem. **9**, 1 (2002).
4. D. F. Gaitan, L. A. Crum, C. C. Churh, and R. A. Roy, J. Acoust. Soc. Am. **91**, 3166 (1992).
5. B. P. Barber, R. A. Hiller, R. Lofstedt, *et al.*, Phys. Rep. **281**, 65 (1997).
6. C.-D. Ohl, T. Kurz, R. Geisler, and W. Lauterborn, Philos. Trans. R. Soc. London **357**, 269 (1999).
7. B. E. Noltingk and E. A. Neppiras, Proc. Phys. Soc. London, Sect. B **63**, 674 (1950).
8. I. M. Margulis and M. A. Margulis, Zh. Fiz. Khim. **75** (3), 527 (2001).
9. L. D. Landau and E. M. Lifshitz, *Mechanics of Continuous Media* (Gos. Izd. Tekh. Teor. Lit., Moscow, 1954), p. 795.
10. R. I. Nigmatulin, I. Sh. Akhatov, N. K. Vakhitova, and R. T. Lahey, Dokl. Akad. Nauk **348**, 768 (1996).
11. G. K. Betchelor, Mekhanika, No. 3, 65 (1968).
12. V. E. Nakoryakov, B. G. Pokusaev, and I. R. Shreiber, *Wave Dynamics of Gas– and Vapor–Liquid Media* (Énergoatomizdat, Moscow, 1990), p. 246.
13. M. Minnaert, Philos. Mag. **16** (7), 235 (1933).
14. M. A. Margulis and A. F. Dmitrieva, Zh. Fiz. Khim. **56** (2), 323 (1982).
15. K. J. Ebeling, Proc. Soc. Photo-Opt. Instrum. Eng. **136**, 348 (1977).

Translated by T. Syromyatnikova

=========== **PHYSICS** ===========

Change in the Parameters
of Surface Thermal Decomposition
# of Energy-Intensive Materials near the Phase-State Boundary

O. F. Shlenskiĭ and Yu. V. Zelenev

Presented by Academician Yu.A. Osip'yan January 16, 2002

Received February 1, 2002

When the surface of nonvolatile thermally unstable substances is intensely heated, temperatures in the chemical-reaction zone can be sufficiently high and reach the temperature boundary of the phase state (BPS), i.e., spinodal, up to which a condensed system conserves thermodynamic stability [1]. In the vicinity of the BPS, the rates of thermal decomposition reactions increase abruptly by several orders of magnitude. This behavior allows the parameters of the BPS to be determined experimentally from the temperature of accessible overheating T_1 [2–6], which differs only slightly from the temperature in the spinodal [2]. The familiar solutions to the problem of the thermal decomposition of materials [7, 8] were obtained disregarding the parameters of the BPS and lead to considerable errors in the high-temperature range. In this study, we develop a simple mathematical model describing the surface thermal decomposition of materials with inclusion of the BPS parameters.

The quasi-stationary process of surface thermal decomposition is described by the equation

$$\lambda \frac{d^2 T}{dx^2} + F(T) - \rho C_p u \frac{dT}{dx} = 0,$$

$$u \frac{d\alpha}{dx} + k(T)\alpha = 0. \tag{1}$$

Here, C_p is the constant-pressure heat capacity, α is the depth of decomposition, u is the velocity of the thermal decomposition front, and $F(T) = Qk(T)$ is the heat-release function, where Q is the heat release of the reaction [8, 9] and $k(T)$ is the reaction-rate constant whose temperature dependence with allowance for the BPS is

represented by the modified Arrhenius equation [4]

$$k(T) = BK \exp\left(-\frac{E}{RT}\right), \tag{2}$$

with $K = \exp\left(\frac{T}{T_1}\right)^n$ or $[1 - (T/T_1)^m]^{-1}$, where B, E, and n are parameters.[1] For a thermal process occurring in a half-space, Eq. (1) must be complemented by two boundary conditions: $\frac{dT}{dx} \longrightarrow 0$ for $x \longrightarrow \infty$ and heat flux $q_w = -\frac{\lambda dT}{dx}$, where λ is the thermal conductivity coefficient, for $x = 0$ (on the free surface of the half-space). Since function (2) is of a complex form, the set of equations (1) cannot be solved analytically. For this reason, we derive the approximate solution of the problem on the basis of the familiar solutions from [8, 9]. Following [9], we separate two regions: the heating zone of the original chemically stable material ($x > \delta$) and the narrow reaction zone of heat release ($x < \delta$) (see Fig. 1). For the heating zone of the original chemically stable material, $F = 0$, and the solution of Eq. (1) has the form of the Mikhel'son exponential [7–9]

$$T(x) = T_0 + (T_s - T_0) \exp\left(-u\left(x - \frac{\delta}{a}\right)\right), \tag{3}$$

where $a = \frac{\lambda}{C_p \rho}$, T_s is the surface temperature, and T_0 is the initial temperature. Equation (3) is corroborated by numerous experimental data [8].

In the absence of flux q_w (heating in vacuum), the temperature gradient near the surface is also absent, and temperature throughout the surface layer δ can be

---

Mendeleev University of Chemical Technology,
Miusskaya pl. 9, Moscow, 125190 Russia

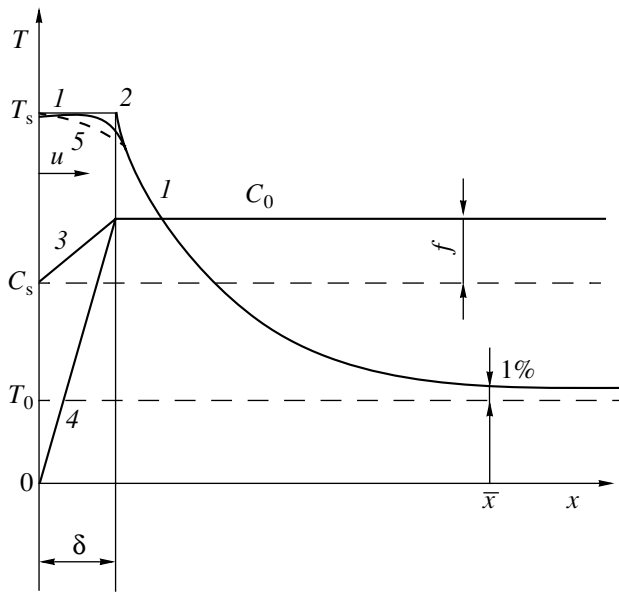[1] Temperature T_1 for polymers was called limiting temperature in [8].

Fig. 1. Distributions of the temperature and concentration of the reactant upon the thermal decomposition of a polymer near the free surface: (*1*) the actual profile of temperature in the material; (*2*) the step-model approximation of the temperature distribution; (*3*) and (*4*) the distribution of the concentration C of the reactant for $T_s < T_1$ and $T_s \approx T_1$, respectively; and (*5*) temperature distribution with allowance for the supply of a heat flux to the surface.

approximately considered as being equal to the temperature of the surface ($T = T_s$). Then,

$$u = \int_0^\delta k\,dx = k\delta, \qquad (4)$$

because $k(T) = \text{const}$ in this layer. In this case, the time of front passage is $t = \dfrac{\delta}{u}$.

For temperatures close to the BPS, homogeneous nuclei are intensely formed and uniformly occupy substance bulk [2, 3]. The number of nuclei with time reaches the limiting value for a certain porosity Π (relative volume of inclusions), when the walls of nuclei touch each other, and uncoupled particles of the incompletely decomposed substance are formed in bulk (i.e., the dispersion effect) [8, 9]. For a chaotic random distribution of nuclei over volume, $\Pi = 0.64$ [10]. As a result of the removal of particles, the reaction involves not all of the substance but only its fraction $f < 1$. If the velocities of gas flows are low, we have $f = f_0 \approx \Pi$. With allowance for the incompleteness of thermal decomposition, the concentration of a substance reacted in time t is $C_0 - C = 1 - f = 1 - kt$, where C_0 is the initial con-

centration. Therefore, $f = kt = \dfrac{k\delta}{u}$, and Eq. (4) takes the form

$$u = \frac{k\delta}{f}. \qquad (5)$$

Quantities δ and T are found from the equation of balance between the heat release and heat spent in heating the substance from the initial to final temperature: $Qkt\rho\delta = \rho\int_0^\infty C_p(T(x) - T_0)\,dx$. Substituting the function $T(x)$ from Eq. (3) into the integrand, we obtain

$$Qk\delta t = C_p(T_s - T_0)\frac{a}{u}. \qquad (6)$$

Substituting time $t = \dfrac{\delta}{u}$ into the left-hand side of Eq. (6), we find

$$\delta = \sqrt{\frac{C_p(T_s - T_0)a}{kQ}}. \qquad (7)$$

In order to determine the surface temperature, we write the equation of the heat flux at the boundary $x = \delta$ between two temperature zones:

$$Q\delta\rho k = \lambda\left|\frac{dT}{dx}\right|_{x=\delta} = \lambda(T_s - T_0)\frac{u}{a} = uC_p(T_s - T_0)\rho. \qquad (8)$$

Here, the temperature gradient $\dfrac{dT}{dx} = (T_s - T_0)\dfrac{u}{a}$ was obtained by differentiating Eq. (3) with respect to coordinate x. Therefore, $u = \dfrac{Q\delta k}{C_p(T_s - T_0)}$.

The substitution of $\delta = \dfrac{fu}{k}$ from Eq. (5) into the last relation and further manipulations yield

$$T_s = \frac{fQ}{C_p} + T_0. \qquad (9)$$

In the absence of nucleation, $f = 1$, and the surface temperature corresponds to the so-called adiabatic temperature in reacting gas mixtures $T_{ad} = \dfrac{Q}{C_p} + T_0$. The substitution of Eq. (9) into Eq. (7) yields

$$\delta = \sqrt{\frac{fa}{k}}. \qquad (10)$$

Then, substituting Eq. (10) into Eq. (5), we find the

desired velocity

$$u = \frac{k\delta}{f} = \frac{\sqrt{ak}}{f} = \frac{a}{\delta}. \tag{11}$$

We now consider examples of calculations and compare the results with experimental data. The table presents temperatures T_1 determined for some substances by the contact thermal analysis with an accuracy of 1.5%. According to [8], the parameters for nitrocellulose at temperature $T_s = 300°C$ are $a = 1.2 \times 10^{-3}$ cm²/s, $E = 44\,600$ cal/mol, $B = 10^{17}$ s⁻¹, and $T_1 = 320°C$. With these values and for $f = \Pi = 0.6$, Eqs. (2) and (11) give the value $u = 7.7 \times 10^{-2}$ cm/s, which is close to the experimental velocity of surface motion for low pressure $u = 8 \times 10^{-2}$ cm/s [8]. The velocity similarly calculated disregarding the BPS was found to be $u = 3.4 \times 10^{-2}$ cm/s, which is equal to half the experimental value.

Let us estimate the thickness of the surface layer δ for the process under consideration. The substitution of a and k values into Eq. (10) yields $\delta = 0.224$ mm. We now determine the heated-layer thickness x for which temperature differs from the initial value by 0.01 (1%). According to Eq. (3), $\ln(0.01) = -u(x - \delta)$. Therefore, $x = 1.22$ mm for velocity $u = 6.05 \times 10^{-3}$ cm/s. Thus, the thickness of the reaction layer is equal to 18% of the heated-layer thickness, which corresponds to Fig. 1. The calculation results for other materials and composites based on nitrocellulose are similar.

As the next example, we calculate the velocity of the thermal-decomposition front for mercury fulminate in vacuum. According to [9], the characteristics of mercury fulminate are $\rho = 3.8$ g/cm³, $a = 1.46 \times 10^{-3}$ cm²/s, $E = 25\,000$ kcal/mol, and $B = 10^{9.0}$ s⁻¹. For temperature $T_s = 633$ K, the calculation gives $u = 0.41$ cm/s, which almost coincides with the experimental value $u = 0.40$ cm/s [9]. At the same time, the velocity similarly calculated disregarding the BPS parameters is equal to $u = 0.1$ cm/s [9], which is a quarter of the experimental value.

As the surface temperature rises, e.g., as a result of the supply of heat flux q_w, and approaches the BPS, the velocity of produced gases increases, and the force of their action on particles of unreacted substance, which is proportional to the square of the gas flow velocity V, increases as well. The rise in the carry-over of particles by the flow reduces the coefficient f. According to the equation of gas-medium continuity, velocity V is related to velocity u as $V = \frac{u\rho}{\rho_g}$, where ρ_g is the gas density. Therefore, the amount of a substance carried over by the flow is also proportional to the square of velocity u, i.e., is equal to cu^2 [11], where c is a coefficient.
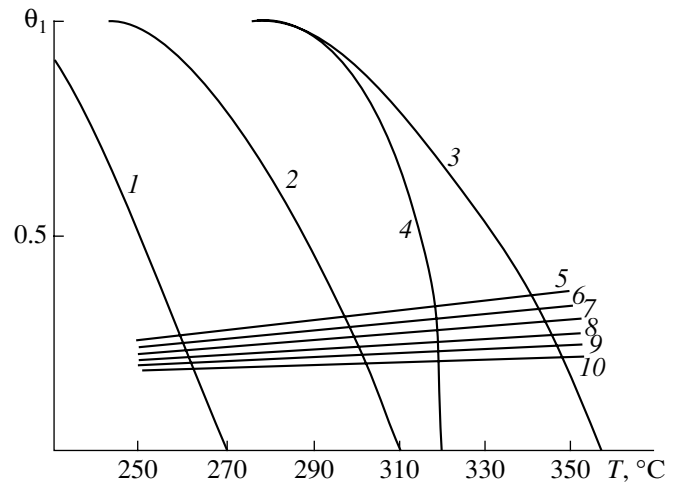
Fig. 2. Plots of the (*1–4*) right-hand and (*5–10*) left-hand sides of Eq. (13) with the use of (*1–3*) Arrhenius equation and (*4*) Eq. (2) for $ca = (1)$ 1, (*2*) 0.1, and (*3*) 0.01 and for $T_{ad} = (5)$ 900, (*6*) 1000, (*7*) 1100, (*8*) 1200, (*9*) 1300, and (*10*) 1400 K.

Then, $f = f_0(1 - cu^2)$, where f_0 is the f value for $u = 0$. Substituting this value into Eq. (9), we obtain $T_s = Qf\dfrac{1 - cu^2}{C_p} + T_0$. Taking into account that $u = \dfrac{ka}{f}$ according to Eq. (11), we arrive at the equation

$$T_s = Qf\frac{1 - cak/f}{C_p} + T_0. \tag{12}$$

Equation (12) is transcendent with respect to the desired temperature T_s entering into the temperature dependence $k(T)$ and can be solved either by iteration

Temperature T_1 at atmospheric pressure for some energy-intensive compounds [4]

Substance	T_1, °C	Substance	T_1, °C
Ammonium nitrate	340	Nitrocellulose (film)	320–330
Ammonium perchlorate	495	Pyroxyline	280
Ammonium bichromate	295	Load azide	395
Load stifnat	355	Potassium azide	550
Celluloid	320	Cadmium azide	340
Mercury fulminate	385	Silver azide	415
Mercury azide	425	Phenol formaldehyde with ammonium perchlorate	496

on a computer or graphically. Figure 2 illustrates the graphical solution to Eq. (12). This equation was preliminarily transformed to the dimensionless form

$$\theta = \frac{T_s - T_0}{T_{ad} - T_0} = \left(1 - \frac{cak}{f}\right)f_0. \qquad (13)$$

The function $k(T)$ shown in Fig. 2 was determined by Eq. (2) for the parameters $E = 35\,000$ cal/mol, $B = 10^{14}$ s^{-1}, $n = 50$, and $T_s = 320°C$ and for a number of ca values for nitrocellulose-based materials. As is seen in Fig. 2, the temperature T_s, which is the abscissa of the point of line intersection near the BPS, depends only slightly on the coefficient c, and the inaccuracy of choosing this coefficient weakly affects the results calculated for T_s. The plot $\theta(T)$ falls sharply near the BPS and closely approaches T_1. Therefore, the temperature T_s in approximate calculations can be taken to be equal to T_1, which gives an underestimation of only 2 to 7 K. Figure 2 also shows T_s calculated from the conventional Arrhenius equation, which is free of information about the BPS and follows from Eq. (2) for $K = 1$. In this case, T_s exceeds T_1 by almost 40 K. Therefore, the calculation disregarding the BPS parameters is physically meaningless. Numerous experimental data corroborate the fact that the surface temperature is below T_1. In particular, for ammonium perchlorate, celluloid, and nitrocellulose, $T_s = 490$, 310, and $300°C$, whereas $T_1 = 495$, 320, and $320°C$, respectively [4, 8, 9, 12].

Equation (11) explains why velocity u depends on the initial temperature of a material. Since the coefficient a for many materials increases with heating, velocity u increases with the initial temperature of a material. This behavior is corroborated by numerous experimental data [8]. Upon removal from the surface, particles of the material are decomposed in the surrounding medium, whose temperature can reach T_{ad}, which gives rise to the heat flux q_w on the surface. In this case, the plot of temperature in the surface layer deviates from the horizontal position as is shown in Fig. 2. We introduce the mean value of the velocity constant as $\chi = \frac{1}{\delta}\int_0^\delta k\,dx$ and, correspondingly, supplement Eq. (6) by a term presenting the additional heat supply $q_w t$ to the reaction layer:

$$Q\chi t\rho\delta + q_w t = \rho C_p(T_s - T_0)\frac{a}{u}.$$

Replacing t by $\frac{\delta}{u}$, we obtain a square equation having two roots (δ_1 and δ_2) among which only one is of

physical meaning:

$$\delta_1 = \frac{-q_w + \sqrt{q_w^2 + 4Q\chi\rho^2 C_p(T_s - T_0)a}}{2Q\chi\rho}. \qquad (14)$$

Thus, with allowance for heat transfer on the surface, the velocity of the thermal-decomposition front is

$$u_1 = \frac{\chi\delta}{f}. \qquad (15)$$

In the particular case where $q_w (q_w \ll 4fQ\chi\rho C_p(T_s - T_0))$, the radicand in Eq. (14) is simplified, and we have $\delta_1 = \delta - \frac{q_w}{2fQ\chi\rho}$ and $u_1 = \frac{\chi\delta}{f} - \frac{q_w}{2f^2 Q\rho}$. A similar result is obtained by substituting the value q_w into the left-hand side of Eq. (8): $fQ\rho\delta\chi + q_w = \lambda(T_s - T_0)\frac{u}{a}$, which corroborates the correctness of the calculation. Therefore, the supply of a heat flux to the surface decreases the thickness of the reaction layer. Nevertheless, velocity u increases, because the surface temperature rises. With allowance for the additional heat flux $q_w t/\rho\delta = q_w/\rho u$, this temperature is $T_s = (f^2 Q + q_w/\rho u_1)/C_p + T_0$, which corresponds to T_s calculated in [9] by another method. Since velocity u enters into the denominator of the second term, temperature T_s for high velocities u observed near the BPS is virtually independent of q_w and of the increase caused in the coefficient of heat release by the increase in medium pressure. At the same time, since the temperature T_1 rises with pressure, the surface temperature increases according to this mathematical model. This behavior corresponds to numerous experimental data [8]. As follows from the above relations, the change in the parameters of the surface decomposition of a material is induced by nucleation processes and by variation in the rate of the reactions of thermal decomposition and dispersion, which increases when approaching the BPS.

CONCLUSIONS

(i) Formulas for the characteristics of the surface thermal decomposition of energy-intensive materials were derived with the inclusion of the parameters of the phase-state boundary.

(ii) By the examples of the thermal decomposition of nitrocellulose and mercury fulminate for low pressures, the calculations were shown to agree qualitatively and quantitatively with experimental data for the velocity of the front of surface thermal decomposition, dispersion degree, and surface temperature.

REFERENCES

1. A. Münster, *Chemical Thermodynamics* (Academie, Berlin, 1969; Mir, Moscow, 1971).

2. V. P. Skripov, E. N. Sinitsyn, P. A. Pavlov, *et al.*, *Thermophysical Properties of Liquids in a Metastable State* (Atomizdat, Moscow, 1980).

3. E. D. Nikitin, P. A. Pavlov, and A. P. Popov, Teplofiz. Vys. Temp. **26** (6), 1090 (1988).

4. O. F. Shlenskiĭ, N. V. Afanas'ev, and A. G. Shashkov, *Thermal Decomposition of Materials* (Énergoatomizdat, Moscow, 1996).

5. O. F. Shlenskiĭ, Dokl. Akad. Nauk **378**, 141 (2001).

6. O. F. Shlenskiĭ, Dokl. Akad. Nauk **380**, 262 (2001).

7. Yu. V. Polezhaev and F. B. Yurevich, *Thermal Defense* (Énergiya, Moscow, 1976).

8. K. K. Andreev, *Thermal Decomposition and Combustion of Explosives* (Nauka, Moscow, 1966).

9. V. A. Strunin, Zh. Fiz. Khim. **10** (2), 433 (1965).

10. V. P. Skripov and V. P. Koverda, *Spontaneous Crystallization of Supercooled Liquids* (Nauka, Moscow, 1964).

11. Yu. I. Dytnerskiĭ, *Processes and Apparatus of Chemical Technology* (Khimiya, Moscow, 1992).

12. D. A. Frank-Kamenetskiĭ, *Diffusion and Heat Exchange in Chemical Kinetics* (Nauka, Moscow, 1967; Princeton Univ. Press, 1955).

Translated by R. Tyapaev

<center>═══════════════ **PHYSICS** ═══════════════</center>

Diffusion Phase Transformations in Nanocrystalline Alloys under Severe Plastic Deformation

V. L. Gapontsev* and V. V. Kondrat'ev**

Presented by Academician V.P. Skripov April 1, 2002

Received March 22, 2002

1. To date, severe plastic deformation is widely used to obtain alloys with a nanocrystalline structure [1]. In these alloys, anomalous diffusion transformations are found such as, e.g., the formation of solid solutions from components that are usually immiscible and modulated structures typical of spinodal decomposition [1, 3]. The physical interpretation of these phase transformations is currently still lacking.

From the analysis of the experiments performed in [1–3], it follows that, when the maximum fragmentation of an alloy, which corresponds to its nanocrystalline state, is attained, the grain boundaries are the main sources and sinks for vacancies. As was shown in [4], the diffusion of vacancies toward the sinks (for different mobilities of components) can cause the layering of an alloy and lead to consecutive phase transformations. The development of an adequate theory implies the generalization of the classical Lifshitz theory for diffusion creep [5] to the case of multicomponent nanophase materials.

In this study, we propose a theoretical approach to describe the process of diffusion in nanocrystalline systems under severe plastic deformation. The specific features of such systems are small grain sizes and a high degree of nonequilibrium of their boundaries. In this case, the supersaturation of the boundaries by vacancies can reach values close to the material melting point. The approach represents the extension of the hole-gas theory [6, 7] to the case of the formation of heterogeneous and, in particular, modulated structures [8, 9]. When solving the diffusion problem, we used mathematical methods for the solution of singular problems [10]. The development of the Cahn–Hilliard theory of spinodal decomposition, which allows for flows of nonequilibrium vacancies, is of interest in its own right.

2. For simplicity, the problem is analyzed in the framework of a one-dimensional diffusion model ($0 < x < L$, where L is the grain size). When finding the diffusion flow of the ith component ($i = A, B$) in a binary A–B alloy, the expression for the probability of the atom–vacancy exchange

$$\tau_i^{-1}(x) \sim \exp\frac{E_i(x)}{kT} \tag{1}$$

is used. Here, the potential energies E_i are determined within the quasi-chemical approximation [6]

$$E_i(x) = Z \sum_{j=A,B} C_j(x)\Phi_{ji}, \tag{2}$$

where Z is the coordination number and Φ_{ij} are the pairwise interaction energies of nearest atoms. We can show that, in approximation (2), the equilibrium state of an alloy is only homogeneous.

For heterogeneous structures, we need to allow for the nonlocal dependence of the energy on the concentration. In the general case, we can represent this dependence in the form

$$E_i = E_i(\sigma_i(x)), \quad \sigma_i(x) = \int_{-\infty}^{+\infty} C_i(x')\tilde{\delta}(x'-x)dx'. \tag{3}$$

Here, the functional kernel $\tilde{\delta}(x)$ has the shape of the delta function with the decay radius $R \sim a$ (a is the lattice parameter). As $R \longrightarrow 0$, we have the conventional version of the hole-gas method [6].

We now consider the final stage of the process, when the displacement velocity U of a grain in its arbitrary cross section is identical and equal to that of the reverse flow $-J_V$ of vacancies. Then, in a coordinate system

―――――――――――――
 * *Ural State Vocational-Pedagogical University,*
  ul. Mashinostroiteleĭ 11, Yekaterinburg,
  620083 Russia
** *Institute of Metal Physics, Ural Division,*
  Russian Academy of Sciences,
  ul. S. Kovalevskoĭ 18, Yekaterinburg, 620219 Russia

moving with a velocity U, we find for the flow of the A component:

$$J_A = (\omega_A' - \omega_B')C_A C_B \frac{\partial C_V}{\partial x} - D\frac{\partial C_A}{\partial x}$$

$$- \lambda^2 C_V \frac{C_A C_B}{kT}\left(\sum_{i=A,B} \omega_i' \frac{dE_i}{dC_i}\right)\frac{\partial^3 C_A}{\partial x^3}. \qquad (4)$$

Here, $x \longrightarrow (x - Ut)L^{-1}$; $\lambda = RL^{-1}$, $\omega_i' = an_0\tau_i^{-1}$ are the component mobilities; n_0 is the density of the lattice sites; and $D = C_V(\omega_A C_B + \omega_B C_A)$ is the interdiffusion coefficient [7], where

$$\omega_i = \omega_i'\left(1 + \frac{C_i}{kT}\frac{\partial E_i}{\partial C_i}\right).$$

Note that the first two terms in Eq. (4) provide the expression for the flow in the hole-gas method [6] and the last term coincides with the corresponding expression in the Cahn–Hilliard theory [9].

3. We now consider two-phase steady states arising under the action of a stationary vacancy flow J_V through the interphase boundary. Let $C_{A\alpha}^e$ and $C_{A\beta}^e$ be equilibrium concentrations of the component A in the α- and β-phases, respectively. Excluding the vacancy concentration gradient from Eq. (4), we arrive at the relation

$$\Psi\lambda^2\frac{d^3 C_A}{dx^3} - \frac{(1 - \Psi C_A C_B)}{C_A C_B}\frac{dC_A}{dx}$$

$$- ((\omega_B')^{-1} - (\omega_A')^{-1})\frac{J_V}{C_V} = 0, \qquad (5)$$

where $\Psi = \frac{2Z}{kT}\left(\Phi_{AB} - \frac{\Phi_{AA} + \Phi_{BB}}{2}\right)$ is the dimensionless mixing energy of the alloy. Equation (5) belongs to the class of singularly perturbed equations. They can be solved by joining asymptotic expansions [10]. According to this method, Eq. (5) within the singularity region near the interphase boundary (phase interface) is represented in a "stretched" coordinate system $X = \frac{x}{\lambda}$. In its initial form, Eq. (5) is valid outside the singularity region. Applying the method of [10], we obtain, in the zeroth approximation in the parameter λ, the external C_A^{ex} and internal C_A^{in} solutions (outside and inside the singularity region, respectively) for the concentration
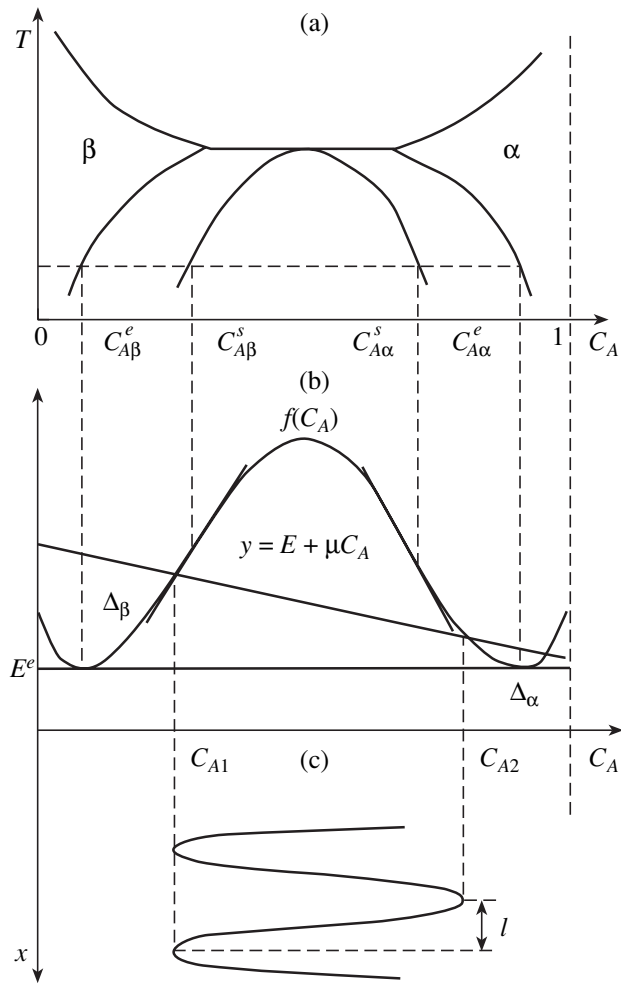

Fig. 1. (a) Equilibrium phase diagram of a regular solid solution with a limited solubility of components; (b) curve $f(C_A)$ for the energy density of the solid solution; and (c) concentration curve of the component of A in the region of singular inhomogeneity.

of the A component. After double integration of the internal equation, we arrive at

$$\frac{1}{2}\Psi\left(\frac{\partial C_A^{in}}{\partial X}\right)^2 = f(C_A^{in}) - \mu C_A^{in} - E, \qquad (6)$$

$$f(C_A^{in}) = \frac{1}{2}\Psi C_A^{in}(1 - C_A^{in})$$

$$+ (1 - C_A^{in})\ln(1 - C_A^{in}) + C_A^{in}\ln C_A^{in}, \qquad (7)$$

where $kTf(C_A)$ is the energy density of the regular solid solution and μ corresponds to the chemical potential [9].

Figure 1 schematically shows the T–C diagram for a solid solution at $\Psi > 4$. Plots for the functions $f(C_A)$ and $y(C_A) = E + \mu C_A$ are also given. The equilibrium state is determined by the position of the straight line $y(C_A) =$
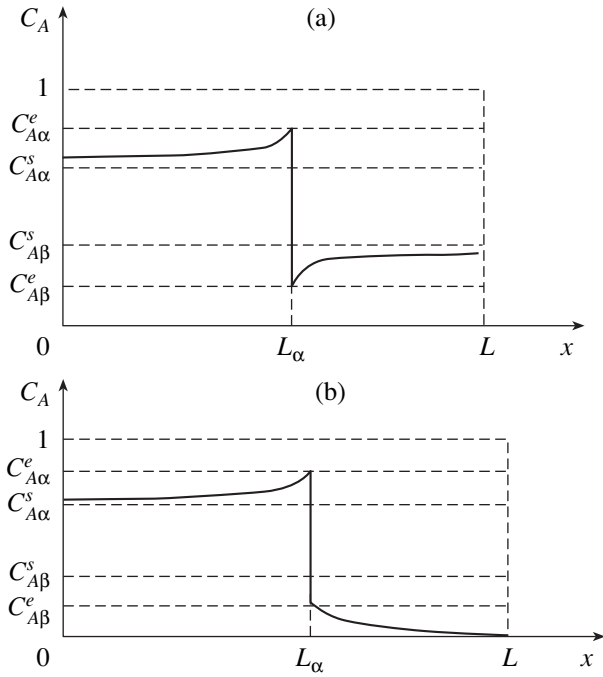
Fig. 2. Curve shapes for concentration distributions of a component for different values of the parameter S: (a) outside the interval (0, 1) and (b) inside the spinodal at $C_{V\alpha}^s \leq S \leq C_{V\beta}^s$.

$E^e + \mu^e C_A$, which is tangent to $f(C_A)$ at the points $C_{A\alpha}^e$ and $C_{A\beta}^e$. In the presence of a vacancy flow, the quantities E and μ, as well as the straight line itself, deviate from the equilibrium position. As a result, for the deviations $\Delta_{\alpha,\beta} = y(C_{A\alpha,\beta}^e) - E^e$, we have

$$\Delta_{\alpha,\beta} = B^2,$$

$$B = \left(\lambda \frac{L J_V}{C_V}\right)^2 \frac{(\omega_A' - \omega_B')^2 C_A^2 (1 - C_A)^2}{2(\omega_A' \omega_B')^2 (1 - \Psi C_A (1 - C_A))^2}. \qquad (8)$$

It is evident that the straight line $y = E + \mu C_A$ shifts upward, and the cuspidal point $C_{A1,2}$ lies within the concentration range ($C_{A\beta}^e$, $C_{A\alpha}^e$).

4. In the qualitative consideration of the problem, we restrict our analysis to small vacancy flows ($\Delta_{\alpha,\beta} \ll 1$). We also assume the concentrations at the phase interface to be in equilibrium, $C_{A\alpha,\beta}^f = C_{A\alpha,\beta}^e$, and the diffusivities and mobility coefficients of the components in each of the phases are constant. In addition, if we take the coordinate dependence of the vacancy concentration to be a linear function, then it is possible to obtain the analytical expression for the alloy component concentrations. Analysis of these expressions indi-

cates that the character of concentration distributions in the phases is associated with the position of the point S, which is a root of the equation ($\omega_A' - \omega_B'$) = 0. If the point S lies outside the interval (0, 1), the difference in the values of mobilities does not change its sign within the entire range of the concentrations. This situation, shown in Fig. 2a, corresponds to an extension of the solubility region of the solid solution and was discussed in [3] for the Al/Fe system. At a certain critical difference in the vacancy concentration within the sink region, the component concentration can reach the spinodal boundary. As a result, the stationary regime becomes unstable, and a new phase interface must appear from which an increase of the α-phase begins in the region of a sink and its decrease in the region of the vacancy source. The final stage in the development of this process must be a state in which the α- and β-phases interchange.

The alternative case occurs when S lies within the spinodal defined by the equation $\Psi C_A (1 - C_A) = 1$ ($C_{A\alpha}^s < S < C_{A\beta}^s$). In this case, the sign of the difference in the mobilities of the system phases is different (Fig. 2b). As is seen, in the vacancy-sink and vacancy-source regions, the concentration curve moves away and towards the spinodal, respectively. For the opposite initial disposition of the phases, this feature is preserved. The formation of a new interphase boundary is unlikely in this case.

For large difference in the vacancy concentrations, the displacements $\Delta_{\alpha,\beta}$ far from the vacancy source can also be large, which results in the mutual approaching of points C_{A1} and C_{A2} and a decrease in the structure period l (the expression for l is given in [9]). As a result, at $l < L$, we can expect the formation of modulated structures. Analysis shows that the maximum change in the structure period l occurs even for small deviations of the straight line $y = E + \mu C_A$ from the equilibrium state. Furthermore, the period l attains a value on the order of $\sim R$ and remains virtually unchanged.

Note that, in the case under consideration (unlike classical spinodal decomposition), the vacancy-induced decomposition of the equilibrium or metastable two-phase state of the alloy occurs. This transformation was apparently observed in the Cu/Co system [2] in which a modulated structure with a nanometer-length scale appeared under plastic deformation.

In conclusion, we draw attention to the following facts. If diffusion processes are initiated by a pulse vacancy flow, then the stationary states considered in this study are "ultimate," since the intermediate states at room temperature are proved to be "frozen" after the deformation has ceased to act [4]. The model of a regular solid solution, which was used in this study, does not affect the main results obtained here. In the general

case, it is sufficient to apply the functional dependence in the form (3) for the component mobilities.

REFERENCES

1. R. Z. Valiev and I. V. Aleksandrov, *Nanostructure Materials Produced by Intense Plastic Deformation* (Logos, Moscow, 2000).
2. C. E. Rodriquez Torres, F. N. Sanches, and L. A. Mendoza Zeilis, Phys. Rev. B: Condens. Matter **51**, 12142 (1995).
3. V. A. Ivchenko, N. Wanderka, U. Czubayko, *et al.*, Mater. Sci. Forum **343**/**346**, 709 (2000).
4. A. E. Ermakov, V. L. Gapontsev, V. V. Kondrat'ev, and Yu. N. Gornostyrev, Fiz. Met. Metalloved. **88** (3), 5 (1999).
5. I. M. Lifshitz, Zh. Éksp. Teor. Fiz. **44**, 1349 (1963) [Sov. Phys. JETP **17**, 909 (1963)].
6. *Interdiffusion Processes in Alloys*, Ed. by K. P. Gurov (Nauka, Moscow, 1973).
7. K. P. Gurov, B. A. Kartashkin, and Yu. É. Ugaste, *Interdiffusion Processes in a Multiphase Metal Systems* (Nauka, Moscow, 1981).
8. V. P. Skripov and A. V. Skripov, Usp. Fiz. Nauk **128**, 193 (1979) [Sov. Phys. Usp. **22**, 389 (1979)].
9. A. G. Khachaturyan, *Theory of Phase Transformations and Structure of Solid Solutions* (Nauka, Moscow, 1974).
10. A. Nayfeh, *Introduction to Perturbation Techniques* (Wiley, New York, 1981; Mir, Moscow, 1984).

Translated by Yu. Vishnyakov

======================= **PHYSICS** =======================

Description of Diffusion in Fractal Media on the Basis of the Klimontovich Kinetic Equation in Fractal Space

Ya. L. Kobelev, L. Ya. Kobelev, V. L. Kobelev,
and Corresponding Member of the RAS E. P. Romanov

Received March 20, 2002

INTRODUCTION

Diffusion processes in media possessing memory, in particular, in fractal media (i.e., when the diffusion is described by differential equations with fractional derivatives), have recently attracted considerable attention [1–7]. This is associated with the fact that equations with fractional derivatives make it possible to describe the temporal behavior of both the mean-square deviation of diffusing particles and a number of other physical quantities in gels, aerosols, solutions of high-molecular compounds, etc. All these quantities were observed to decrease with time more slowly than is predicted by the ordinary diffusion equation. This suggests that Levi-type, rather than Gaussian, distributions should be used for describing diffusion processes in such media. These processes usually obey either the Langevin equation with regard to white or color noise or kinetic equations. In so doing, either the diffusion in momentum space or that in coordinate space is considered. A kinetic equation describing processes in plasma, fluids, rarefied gases, etc., was proposed in a series of papers [8–11] by Klimontovich. The equation allows for diffusion in both momentum and coordinate spaces and thereby more adequately takes into account actual features of physical processes in the above media. In the absence of external forces, Klimontovich's equation in the diffusion approximation takes the form

$$
\frac{\partial}{\partial t} f(r, p, t) = \frac{\partial}{\partial x_\alpha}\left[D^r_{\alpha\beta}(r, p)\frac{\partial}{\partial x_\beta} f(r, p, t) \right]
$$
$$
+ \frac{\partial}{\partial p_\alpha}\left[D^p_{\alpha\beta}(r, p)\frac{\partial}{\partial p_\beta} f(r, p, t) \right]. \tag{1}
$$

Here, x and p are the coordinates and momenta of particles; $f(x, p, t)$ is the distribution function; $r = (x, y, z)$ (the summation over the subscripts α and β {$\alpha, \beta = (x, y, z)$} is implied); and D^r and D^p are the diffusion

coefficients in coordinate and momentum spaces, respectively. The substantiation of this equation for a wide class of physical problems was also given in [8–11].

The goal of the present paper is to analyze the one-dimensional Klimontovich equation with fractional derivatives with respect to time, coordinates x, and momenta p. The equation is suitable for describing processes in disordered media, in the vicinity of rough surfaces (described in terms of fractal geometry), in gels and aerosols, etc. Thus, we deal with processes in media for which the relaxation and diffusion are not Debye processes. In this case, the mean-square particle displacement is proportional to a fractional power of time. In what follows, such media will be referred to as fractal media. The one-dimensional Klimontovich equation for such media takes the form (with the diffusion coefficients independent of x, p, and t)

$$
\frac{\partial^\nu}{\partial t^\nu} f(x, p, t)
$$
$$
= D^x \frac{\partial^{2\gamma}}{\partial x^{2\gamma}} f(x, p, t) + D^p \frac{\partial^{2\xi}}{\partial p^{2\xi}} f(r, p, t), \tag{2}
$$

where γ, ν, and ξ are fractional numbers satisfying the conditions $\gamma \le 1$, $0 \le \nu \le 1$, and $\xi \le 1$. When allowing for relaxation processes, the corresponding term should be introduced into Eq. (2):

$$
\frac{\partial^\nu}{\partial t^\nu} f(x, p, t) = D^x \frac{\partial^{2\gamma}}{\partial x^{2\gamma}} f(x, p, t)
$$
$$
+ D^p \frac{\partial^{2\xi}}{\partial p^{2\xi}} f(r, p, t) - \tau^{-1} f(x, p, t), \tag{3}
$$

where τ is the relaxation time. As was noted by Klimontovich, formally introducing a relaxation term [see Eq. (3)] into Eq. (2) is accompanied by a difficulty concerning the normalization of the distribution function: the normalization factor proves to be dependent on time. On the one hand, this results in a widening of the range of problems described by this equation (including problems with a nonconserved number of particles, e.g., certain problems of chemical kinetics). On the

Ural State University,
pr. Lenina 51, Yekaterinburg, 620083 Russia

other hand, problems based on Eq. (3) and requiring that the number of particles in the system be conserved (i.e., the normalization factor be constant) have a physical sense only in the limit $\tau = \infty$. Since Eq. (3) is more general than Eq. (2), solutions to Eq. (2) can be obtained from those of Eq. (3) as a particular case corresponding to $\tau = \infty$. It is worth noting that the Klimontovich equation in fractal media completely allows for the diffusion in both coordinate and momentum spaces. The relaxation time τ can be written out in the form $\tau^{-1} = \tau_p^{-1} + \tau_x^{-1}$, where τ_p and τ_x are the relaxation times in momentum and coordinate spaces, respectively. This makes it possible to take into account either both of the relaxation types or any one of them.

INITIAL CONDITIONS AND AN EXACT SOLUTION TO THE KLIMONTOVICH EQUATION

To solve Eq. (3), we impose the initial conditions $f(x, p, t)_{t=0} = f_0(x, p)$ and rewrite Eq. (3) in the form

$$\frac{\partial^\nu}{\partial t^\nu}[f(x, p, t) - f_0(x, p)] = D^x \frac{\partial^{2\gamma}}{\partial x^{2\gamma}} f(x, p, t)$$

$$+ D^p \frac{\partial^{2\xi}}{\partial p^{2\xi}} f(r, p, t) - \tau^{-1} f(x, p, t). \tag{4}$$

We perform the Laplace transformation of Eq. (4) with respect to t and the integral Fourier transformation with respect to p and x. We also take into account the definition of fractional derivatives [12]

$$_0D_t^\nu g = \frac{\partial^\nu g}{\partial t^\nu} = \frac{1}{\Gamma(-\nu + n)}\left(\frac{d}{dt}\right)^n \int_0^t dt' \frac{g(t')}{(t - t')^{\nu - n + 1}}, \tag{5}$$

$$n - 1 \le \nu < n$$

and the rule for the fractional differentiation of a constant f_0 with respect to time

$$_0D_t^\nu f_0 = f_0 \frac{t^{-\nu}}{\Gamma(1 - \nu)}, \tag{6}$$

where $_0D_t^\nu \, _0D_t^{-\nu} = 1$ and $\Gamma(x)$ is the gamma function. As a result, we find from Eq. (4)

$$f(x, p, t) = \frac{1}{(2\pi)^2} \int_{-\infty}^{\infty} dp' \int_{-\infty}^{\infty} dk \, e^{ikx + ipp'} f_0(k, p')$$

$$\times \int_{c - i\infty}^{c + i\infty} d\omega e^{\omega t} f(k, p', \omega), \tag{7}$$

$$f(k, p', \omega) = \frac{\omega^{-1}}{1 + (T^{-1}\omega)^{-\nu}}, \tag{8}$$

where

$$T = [t\tau^{-1} - D^x(ik)^{2\gamma} - D^p(ip')^{2\xi}]. \tag{9}$$

Following [2–3, 13], we express Eq. (8) in terms of the Fox functions [14, 15] and then perform the inverse Laplace transformation of the function $f(k, p', \omega)$ also presented in the Fox functions. As a result, we arrive at the expression

$$f(x, p, t) = A \int_{-\infty}^{\infty} dk \int_{-\infty}^{\infty} dp \, e^{ikx_1 + ipp_1}$$

$$\times \sum_{n=0}^{\infty} \frac{(-1)^n}{\Gamma(1 + \nu n)} [t^\nu \tau^{-\nu} - (ik)^{2\gamma} - (ip)^{2\xi}]^n f_0(k, p), \tag{10}$$

where

$$A = (D^x t^\nu)^{-\frac{1}{2\gamma}}(D^p t^\nu)^{-\frac{1}{2\xi}},$$

$$x_1 = x(D^x t^\nu)^{-\frac{1}{2\gamma}}, \quad p_1 = p(D^p t^\nu)^{-\frac{1}{2\xi}}. \tag{11}$$

ASYMPTOTIC ESTIMATE OF THE SOLUTION AT LONG TIMES

In the case of $\nu < 1$, we failed to integrate over k and p the Fourier integral transformation expressed in terms of the Fox functions in Eq. (10). Therefore, only rather crude estimations will be given below for the behavior of exact solution to Eq. (10) at long times. It is worth noting that in the case of $\gamma = 1$, $\xi = 1$, $\nu = 1$, and $f_0(k, p') = 1$, the well known asymptotic expression

$$f \sim \frac{1}{(Dt)^{\frac{1}{2}}(Dt)^{\frac{1}{2}}} \exp\left(-\frac{x^2}{2^2 Dt} - \frac{t}{\tau} - \frac{p^2}{Dt}\right) \tag{12}$$

follows from Eq. (10).

We now estimate the rate of a decrease in exact solution to Eq. (10) at long times t. This estimate can be obtained from Eq. (10) by substituting the function $\Gamma(1 + \nu n)$ for $\Gamma(1 + n)$. Such a substitution leads to an increase in each term of the sum entering into Eq. (10) and, hence, allows us to find an asymptotic estimate of the solution to Eq. (10) for small x_1 and p_1 as $\nu \longrightarrow 1$, i.e., the maximum rate of a decrease in the function f. In this approximation, the summation in Eq. (10) yields the integral

$$f(x, p, t) = A \int_{-\infty}^{\infty} dk$$

$$\times \int_{-\infty}^{\infty} dp \exp[-(t\tau^{-1} - (ik)^{2\gamma\nu^{-1}} - (ip)^{2\xi\nu^{-1}})^\nu$$

$$+ ik_1 x + ip_1 p] f_0(k, p). \tag{13}$$

In order to estimate expression (13) for small x_1 and p_1 (i.e., for long times t) and for arbitrary $0 \leq \nu \leq 1$, we compute the fractional power ν of the trinomial in the exponential function of (12), expand this function (except for the first terms) in powers of ν, and write out the remaining integrals as series in powers of x_1 and p_1. For large t, the first term of this expansion is largest and takes the form

$$
f \sim \frac{f_0}{(D^x t^\nu)^{1/2\gamma}(D^p t^\nu)^{1/2\xi}}
$$
$$
\times \exp\left(-\frac{x^{2\gamma}}{2^{2\gamma}D^x t^\nu} - \frac{t^\nu}{\tau^\nu} - \frac{p^{2\xi}}{2^{2\xi}D^p t^\nu}\right). \tag{14}
$$

For $\gamma \leq 1, \nu \leq 1, \xi \leq 1$, and long times, the exact solution $f(x, p, t)$ decreases not more rapidly than the function determined by expression (14).

CONCLUSIONS

Kinetic processes depending on time more slowly than ordinary diffusion processes must be described with the help of Levi-type, rather than Gaussian, distributions. To do this, we write out the Klimontovich kinetic equation in a fractal space. The equation is suitable for describing kinetic processes in media similar to gels, aerosols, electron–ion plasma, etc., i.e., in the cases when Levi-type distributions are necessary for a more complete description of the behavior of the medium. We have found an exact solution to this equation in the form of series in the Fox functions and have analyzed the asymptotic behavior of the solution at long times, as well as a passage to the case of a non-fractal space. The results obtained can be used for describing physical processes (among them, processes in disordered or partially ordered media, etc.) whose kinetic description requires introducing fractional derivatives.

ACKNOWLEDGMENTS

REFERENCES

1. V. V. Yanovsky, A. V. Chechkin, D. Schertzer, and A. V. Tur, Physica A (Amsterdam) **282**, 13 (2000).
2. W. G. Gloecke and T. F. Nonnenmacher, J. Stat. Phys. **71** (3/4), 741 (1993).
3. W. R. Schneider and W. Wyss, J. Math. Phys. **30**, 134 (1989).
4. R. Metzler and J. Klafter, Phys. Rep. **339**, 1 (2000).
5. V. L. Kobelev, E. P. Romanov, L. Ya. Kobelev, and Ya. L. Kobelev, Izv. Ross. Akad. Nauk, No. 12, 2401 (1998).
6. R. R. Nigmatullin, Teor. Mat. Fiz. **90**, 354 (1992).
7. V. L. Kobelev, E. P. Romanov, L. Ya. Kobelev, and Ya. L. Kobelev, Dokl. Akad. Nauk **361**, 755 (1998) [Dokl. Phys. **43**, 537 (1998)].
8. Yu. L. Klimontovich, *Turbulent Motion and the Structure of Chaos* (Nauka, Moscow, 1990).
9. Yu. L. Klimontovich, *Statistical Physics of Open Systems* (Yanus, Moscow, 1995; Kluwer, Dordrecht, 1995), Vol. 1; *Statistical Physics of Open Systems* (Yanus, Moscow, 1999), Vol. 2; *Statistical Physics of Open Systems* (Yanus, Moscow, 2001), Vol. 3.
10. Yu. L. Klimontovich, Teor. Mat. Fiz. **92**, 312 (1992).
11. Yu. L. Klimontovich, Phys. Lett. A **197**, 434 (1992).
12. S. G. Samko, A. A. Kilbas, and O. I. Marichev, *Fractional Integrals and Derivatives, Theory and Applications* (Nauka i Tekhnika, Minsk, 1987; Gordon & Breach, Amsterdam, 1993).
13. M. Dzhrbashyan, *Integral Transformations and Representation of Functions in the Complex Region* (Nauka, Moscow, 1976).
14. C. Fox, Trans. Am. Math. Soc. **98**, 395 (1961).
15. A. M. Mathai and R. K. Saxena, *The H-Function with Applications in Statistics and Other Disciplines* (Wiley Eastern Ld., New Delhi, 1978).

Translated by V. Chechin

Angular Distribution of Photoelectron Spectra of Solids with Allowance for Second-Order Nondipole Effects and Elastic Scattering

**Corresponding Member of the RAS V. I. Nefedov*, I. S. Nefedova*, V. G. Yarzhemsky*,
M. B. Trzhaskovskaya**, and P. Streubel***, and R. Szargan*****

Received April 3, 2002

The nondipole component of the interaction of photons with atoms considerably affects the angular distribution of photoelectrons [1–3]. The angular distribution of electrons from the photoionization of solids was studied for unpolarized [4] and polarized [5] radiation with the inclusion of elastic scattering and the first-order nondipole component of the interaction of electromagnetic radiation with a substance. The first-order nondipole effects were found to substantially change the angular distribution of photoelectrons. Therefore, these effects must be taken into account when the element composition of a substance is analyzed by electron spectroscopy. Analyzing the angular dependence of the photoelectron spectra of Ne atoms, Derevianko *et al.* [6] concluded that higher orders of the interaction of electromagnetic radiation with a substance contribute considerably to the photoelectron angular distribution.

In this paper, we study the effect of higher order nondipole corrections on the angular distribution of the photoelectron spectra of solids.

TRANSPORT THEORY

The angular distribution of photoelectrons from ionization by linearly polarized electromagnetic radiation is expressed as

$$\frac{d\sigma}{d\Omega} = \frac{\sigma F}{4\pi}, \tag{1}$$

where

$$F = 1 + (\beta + \Delta\beta)P_2(\cos\theta) + (\delta + \gamma\cos^2\theta)\sin\theta\cos\phi$$
$$+ \eta P_2(\cos\theta)\cos 2\phi + \mu\cos 2\phi + \xi(1 + \cos 2\phi)P_4(\cos\theta)$$

* *Kurnakov Institute of General and Inorganic Chemistry,*
  Russian Academy of Sciences,
  Leninskiĭ pr. 31, Moscow, 117907 Russia
** *Petersburg Nuclear Physics Institute,*
  Russian Academy of Sciences,
  Gatchina, St. Petersburg, 188350 Russia
*** *Universität Leipzig,*
  Linnerschtrasse 2, Leipzig, Germany

includes the dipole component of interaction, first-order nondipole component, and higher order nondipole components given by the formula [6]

$$f = \Delta\beta P_2(\cos\theta) + \eta P_2(\cos\theta)\cos 2\phi$$
$$+ \mu\cos 2\phi + \xi(1 + \cos 2\phi)P_4(\cos\theta). \tag{2}$$

Figure 1 shows the definition of the angles.

In the typical geometry of experiments, a photon flux is perpendicular to the surface of a sample. In this case, angles are related as [5]

$$\cos\theta = \sin\alpha\cos\phi_0, \tag{3}$$

$$\cos\alpha = -\sin\theta\cos\phi. \tag{4}$$

It follows from these relations that

$$\cos 2\phi = \frac{2\cos^2\alpha}{1 - \sin^2\alpha\cos^2\phi_0} - 1. \tag{5}$$
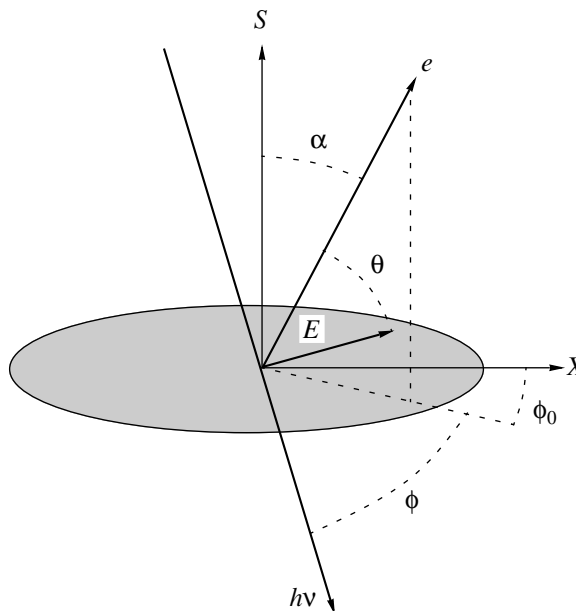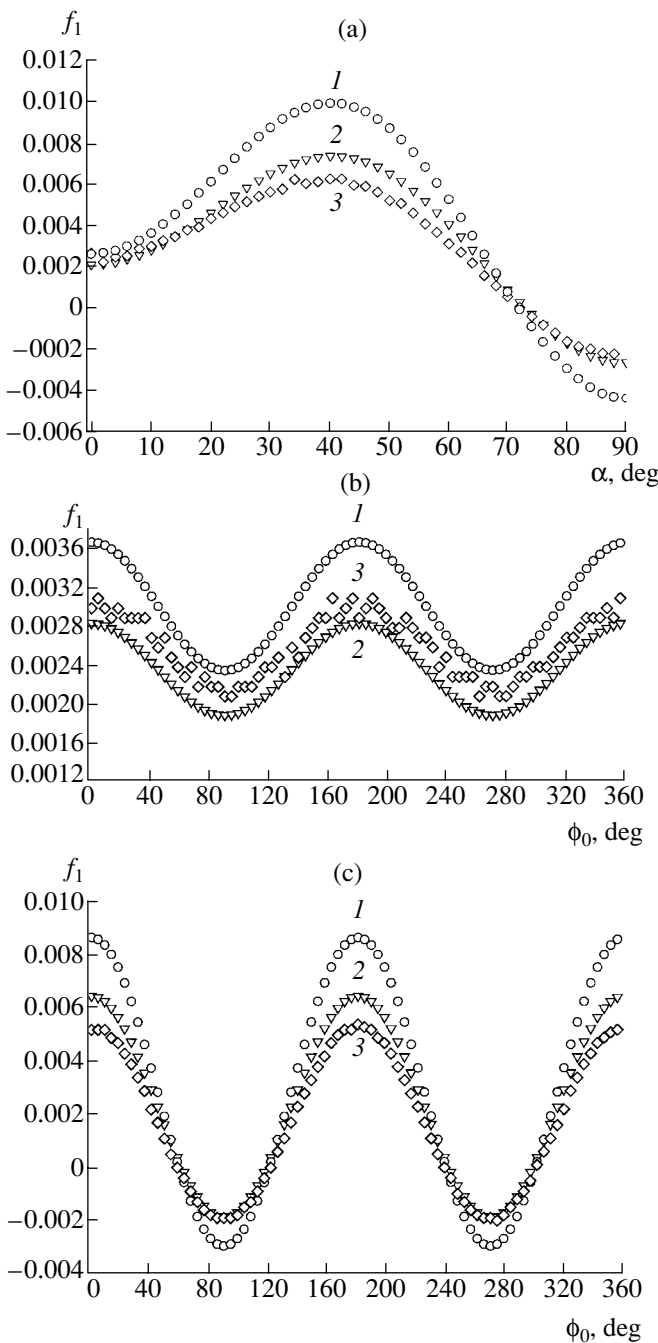
Applying transport theory [5, 7] and Eqs. (3)–(5), we

Fig. 1. Definition of the angles.

Fig. 2. Quantity f_1 as a function of the angle (a) α for $\phi_0 = 0°$, (b) ϕ_0 for $\alpha = 10°$, and (c) ϕ_0 for $\alpha = 50°$ as calculated for (*1*) a free atom; (*2*) an atom in a solid transport theory; and (*3*) an atom in a solid Monte Carlo result.

obtain the following angular distribution of final photoelectrons, whose initial distribution was given by Eq. (2):

$$f_1 = a\{\xi[a^{1/2}H(\cos\alpha, \omega)$$
$$-1 + (1 + \cos 2\phi)P_4(\cos\theta)] + \Delta\beta P_2(\cos\theta)$$
$$+ \eta P_2(\cos\theta)\cos 2\phi + \mu\cos 2\phi\} + A, \qquad (6)$$

where $a = 1 - \omega$, $H(\cos\alpha, \omega)$ is the Chandrasekhar function, and

$$A = 0.25H(\cos\alpha, \omega)\omega a$$

$$\times \left\{(4.5\eta + 1.5\Delta\beta + 10\xi)\int_0^1 \frac{x^3 H(x, \omega)dx}{\cos\alpha + x}\right.$$

$$-(1.5\eta + 0.5\Delta\beta)\int_0^1 \frac{xH(x, \omega)dx}{\cos\alpha + x} \qquad (7)$$

$$\left.-8.75\xi\int_0^1 \frac{x^5 H(x, \omega)dx}{\cos\alpha + x}\right\}.$$

Quantities A and $f_1 - A$ were calculated for the following parameters: all combinations of values $0°$, $15°$, $30°$, …, $90°$ of angles α and ϕ_0; $\omega = 0.15$ and 0.3; $\Delta\beta$, μ, η, and ξ values [8] corresponding to $1s$, $2s$, and $2p$ levels of Ne and $4s$, $4p$, and $4d$ levels of Xe; and a photoelectron kinetic energy of 1 keV. It was found that A is usually less than 10% of $f_1 - A$ and can be ignored in the first approximation. If f_1 changes sign with varying ϕ_0, A can be commensurate with f_1. In this case, A must be taken into account. We emphasize that the term including the integral

$$\int_0^1 \frac{xH(x, \omega)dx}{\cos\alpha + x} \qquad (8)$$

is always small and can be ignored.

For the above-listed parameters, f_1 is usually equal to about 0.01, which is several percent of the total intensity and about 10% of the first-order dipole transitions. The second-order correction is an oscillating function of angle ϕ_0.

MONTE CARLO CALCULATIONS

Following [4, 5, 9], Monte Carlo calculations were carried out for the $3d$ Ag line and for the above experimental case. The ranges of angles α and ϕ_0 are divided into 90 and 80 sections, respectively. In each section, 1000 paths each for 16 different sample depths are taken. Therefore, there are 1.152×10^8 independent paths. The photoelectron kinetic energy is equal to 1.5 keV. The single scattering albedo ω is equal to 0.22 [10]. The elastic and inelastic mean free paths are equal to 9.33 and 19.2 Å, respectively.

In this study, the parameters $\Delta\beta$, η, μ, and ξ characterizing the quadrupole and octupole interactions $E1E3$, $E1E2$, and $E1M2$ of order $O(k^2\alpha^2)$ were calculated for the $3d$ Ag line and a kinetic energy of 1.5 keV in the relativistic approximation (as in [3]). The Dirac–Fock–Slater atomic potential with coefficient $C = 1$ for the exchange term was used. The bound-state wave functions were calculated by the method of the self-

consistent field for a neutral atom. The continuous-spectrum wave functions were calculated in the approximation of quenched orbital angular momentum with the Dirac–Fock–Slater potential of an ion with a vacancy arising after photoionization. The parameters were calculated as 0.0047, –0.00112, 0.00594, and −0.00482, respectively.

Figure 2 shows the Monte Carlo and transport-theory results. The results for the $3d$ line of a free Ag atom are also shown. In agreement with expectations, the intensity for a solid Ag sample is lower than the intensity for free Ag atoms for most angles, because photoelectrons undergo elastic scattering in a solid. The Monte Carlo and transport-theory results agree well with each other. The corrections in question depend strongly on the azimuth angle ϕ_0 and must be taken into account when the diffraction of photoelectrons at certain α angles is analyzed.

ACKNOWLEDGMENTS

REFERENCES

1. M. Ya. Amus'ya, A. S. Baltenkov, A. A. Grinberg, and S. G. Shapiro, Zh. Éksp. Teor. Fiz. **68**, 28 (1975) [Sov. Phys. JETP **41**, 14 (1975)].
2. J. W. Cooper, Phys. Rev. A **47**, 1841 (1993).
3. M. B. Trzhaskovskaya, V. I. Nefedov, and V. G. Yarzhemsky, At. Data Nucl. Data Tables **77**, 97 (2000).
4. V. I. Nefedov and I. S. Nefedova, J. Electron Spectrosc. Relat. Phenom. **107**, 131 (2000).
5. V. I. Nefedov and I. S. Nefedova, J. Electron Spectrosc. Relat. Phenom. **113**, 3 (2000).
6. A. Derevianko, O. Hemmers, S. Oblad, *et al.*, Phys. Rev. Lett. **84**, 2116 (2000).
7. A. Jablonski and I. S. Telinin, J. Electron Spectrosc. Relat. Phenom. **74**, 202 (1995).
8. A. Derevianko, W. R. Johnson, and K. T. Cheng, At. Data Nucl. Data Tables **73**, 153 (1999).
9. V. I. Nefedov and I. S. Fedorova, J. Electron Spectrosc. Relat. Phenom. **85**, 211 (1997).
10. V. I. Nefedov and I. S. Nefedova, J. Electron Spectrosc. Relat. Phenom. **95**, 281 (1998).

Translated by R. Tyapaev

===== **PHYSICS** =====

Initiation of Propane–Air-Mixture Combustion by Pulse-Periodic CO$_2$-Laser Radiation

P. K. Tretyakov*, S. S. Vorontsov*, A. F. Garanin*, G. N. Grachev**,
A. L. Smirnov**, and A. V. Tupikin*
Presented by Academician A.K. Rebrov February 27, 2002

The efficient absorption by a reactive medium of laser-radiation energy can result in the initiation of pre-ignition reactions and in the inflammation of a combustible mixture. As is well known, the formation in a reacting medium of nonequilibrium oscillatory excited molecular states is possible under the action of both pulsed and permanent sources of laser radiation. The use of such sources with a sufficiently high output power stimulated the development of infrared photochemistry [1]. The resonance absorption of laser radiation by hydrocarbons (e.g., by methane and propane) was studied in [2, 3]. In [4], an increase in the combustion rate for a laminar flame of a propane–air mixture was observed under the action of the intense radiation emitted by a continuous CO$_2$ laser. The authors of [4] relate the mechanism of this action with the photodissociation of propane molecules and formation in a reacting mixture of active atoms and radicals (the so-called kinetic mechanism). These authors admit a possibility of heating the mixture as a result of the absorption of laser radiation (the thermal mechanism). A similar conclusion is made in [5], where the detonation in a tube filled with a propane–air mixture was initiated by focused CO$_2$-laser radiation. In [6], results of theoretical and experimental studies of thermal ignition for homogeneous mixtures of ethylene with an oxidizer, which is induced by a pulse CO$_2$ laser, are analyzed. Good agreement is obtained between calculated predictions based on the absorption model and the experimental data on the temperature variation. In [7], mechanisms resulting in the self-ignition of mixtures H$_2$ + O$_2$ (air) are analyzed with the assumption that, under external actions (e.g., electric discharge or laser radiation), the preliminary excitation of vibrational degrees of freedom occurs for reacting molecules.

In the experiments of [8], optical pulse discharge (OPD) was applied to stabilize the turbulent combustion of hydrogen–air mixtures. These experiments extended the limits of stable combustion with respect to both the gas-flow rate and the mixture composition compared to the flame stabilization by the recirculation zone formed on the jet axis. The experiments were continued with the propane–air mixture. The phenomenon of the stable ignition and combustion stabilization in a turbulent flow of propane–air mixtures under the action of focused pulsed CO$_2$-laser radiation in the absence of the laser-induced breakdown of the medium was discovered.

The layout of the experiment is presented in Fig. 1. The mixing of propane with air occurred prior to their injection into the combustion chamber (*1*). The flow was straightened with the help of meshes (*2*) installed in the chamber, and the efflux proceeded into the environment through a narrowing nozzle (*3*). In order to ensure reliable laser-induced breakdown and a decrease in the threshold-radiation power, argon was introduced into the beam-focusing zone on the jet axis through a
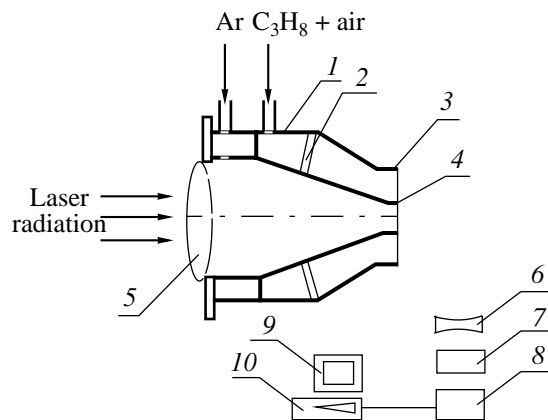

Fig. 1. Layout of the experiment. (*1*) Combustion chamber; (*2*) mesh; (*3*) nozzle 20 mm in diameter; (*4*) nozzle 3 mm in diameter; (*5*) KCl lens; (*6*) light filter; (*7*) camera lens; (*8*) technical-vision camera; (*9*) video tape recorder; (*10*) monitor.

---

* *Institute of Theoretical and Applied Mechanics,*
  Siberian Division, Russian Academy of Sciences,
  Institutskaya ul. 4/1, Novosibirsk, 630090 Russia
** *Institute of Laser Physics, Siberian Division,*
  Russian Academy of Sciences,
  Institutskaya ul. 4/3, Novosibirsk, 630090 Russia

small-diameter (3 mm) nozzle (*4*). The argon rate was constant and equal to $U_{Ar} = 17$ m/s. In the experiments without the laser-induced breakdown, argon was not injected. The radiation generated by a LOK-3MSI pulse-periodic CO_2 laser was focused by a lens (*5*) at a distance of 7–8 mm from the jet output cross section. The combustion process was investigated using spectral-zonal registration of the CH-radical radiation in the green–blue spectral region. The flame radiation within the visible wavelength range of 400–500 nm was separated by an optical filter (*6*) and fixed by a technical-vision camera (*7*). The exposure was chosen in accordance with the luminosity of the object and varied within the limits of 10^{-3}–10^{-5} s. A series of pictures related to the same regime was averaged and treated by standard graphical means of the Windows software package. In the process of performing the experiments, we varied parameters of the mixture flow (the rate U_0 and the coefficient α of the air excess). Radiation characteristics such as the energy-pulse frequency f, the average radiation power N_{av}, the total pulse duration τ_p, and that of the pulse-peak τ_{peak}, as well as the intensity in the focus (I) also changed. The flow parameters and radiation characteristics are listed in Tables 1 and 2.

Figure 2 illustrates features of the flame for the two methods of combustion initiation in the case of an approximately permanent mixture flow rate. It is necessary to note the difference in the onset domain of flame development depending on the ignition method. While initiating the OPD (in the picture, the region of the bright plasma glow is closed by a screen in order to reduce the effect of this region on the flame-radiation registration), ignition develops near the rear discharge boundary (Fig. 2a). When initiating by the radiation without forming the laser-induced breakdown (in the absence of the argon inflow), the onset domain of the flame formation has a characteristic segment extended in the direction opposite to the jet efflux (Fig. 2b). This is caused by a small rarefaction at the jet axis, which arises behind the small-diameter part of the nozzle (see Fig. 1, position *4*). There is yet another characteristic distinction associated with a horizontal jet inflow into the flooded space and the effect of lifting forces. This is especially pronounced in the absence of the OPD. The flame is asymmetric with respect to the axis (Fig. 2b). In the experiments with the OPD, the effect is weakened by the existence of the argon jet and the lower combustion intensity (the combustion zone is more extended). The comparison of certain flame pictures taken with a short exposure (10^{-4} s) shows that the combustion is of an unsteady nature. This testifies to the fact of the realization of the turbulent flame-propagation mechanism. The interval of the Reynolds numbers (see Table 1) exceeds the upper boundary of the laminar flow. In order to realize the quasi-steady flame mode, it is necessary for the characteristic combustion time to be longer than the time gap between the energy pulses. The time of the gas residence in the laminar-flame front
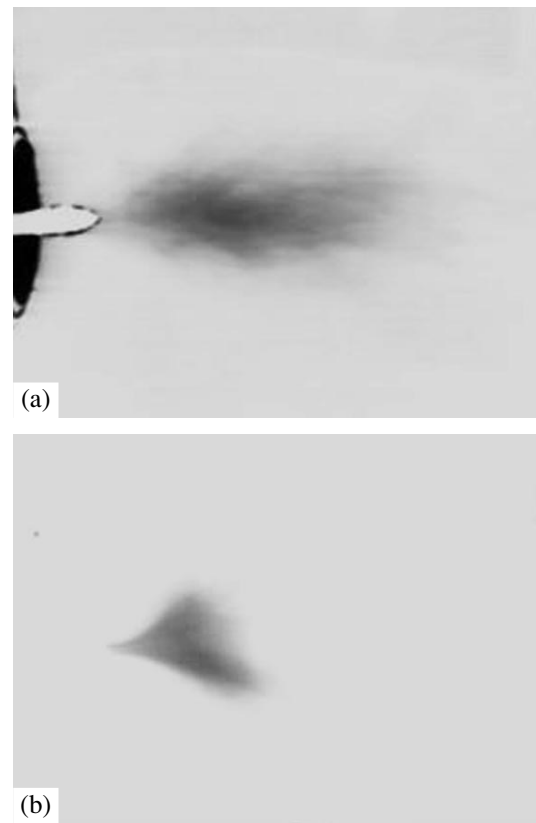

(a)

(b)

Fig. 2. Flame photographic image. $U_0 = 2.5$ m/s. OPD: (a) $\alpha = 1.07$; radiation: (b) $\alpha = 1.28$.

is considered as a characteristic combustion time $\tau_f = \dfrac{a}{U_n^2}$ [9], where a is the mixture thermal diffusivity and U_n is the normal velocity of the flame propagation. For the propane–air mixture (being maintained at room temperature), $\tau_f \approx 1.5 \times 10^{-3}$ s. In the experiments, the maximal time between the pulses was lower than this

Table 1. Gas-flow parameters

U_0, m/s	1.9–3.8
α	0.76–2.8
$Re \times 10^3$	2.7–5.5

Note: The Reynolds number was determined by the nozzle diameter.

Table 2. Laser-radiation parameters

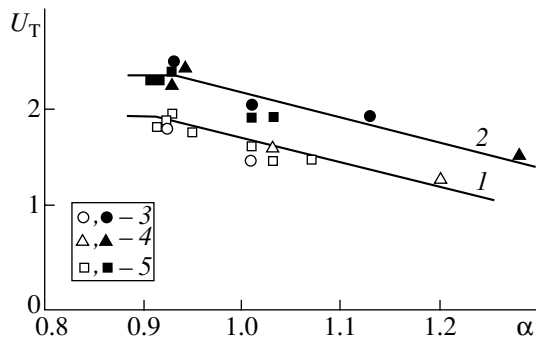| f, kHz	N_{av}, kW	N_{peak}, kW	τ_{peak}, μs	τ_p, μs	I, kW/cm^2
17	1.3	180	0.3	1.6	560
30	1.8	100	0.3	4.0	310
45	1.8	85	0.3	2.0	270

Fig. 3. Effect of the combustion initiation on the turbulent velocity of the flame propagation (U_0 = 2.5–2.86 m/s). (*1*) OPD; (*2*) pulse-periodic radiation; f = (*3*) 17; (*4*) 30; (*5*) 45 kHz.

value by more than an order of magnitude (namely, by a factor of 25). We may consider that in the experiments, the quasi-steady regime of flame stabilization is attained. The turbulent combustion rate was determined according to the tilt angle of the flame-front leading edge with respect to the flow direction: $U_T = U_0 \sin \varphi/2$, where φ is the total angle of a cone formed by the front. The existence of lifting forces introduces a certain error into this method. However, for the qualitative comparison of the combustion efficiency, this argument is not decisive. The effect of the method of combustion initiation is shown in Fig. 3. The general character of the variation of U_T as a function of α is consistent with physical concepts (U_T decreases with α). As follows from Fig. 3, the turbulent-combustion rate for initiation of the ignition process by focused pulse-periodic radiation in the absence of laser-induced breakdown is higher than in the case of OPD ignition by approximately 25%.

Thus, the pulse-periodic radiation of a CO_2 laser with a high repetition frequency in the absence of the laser-induced breakdown of a medium makes it possible to initiate and to maintain the stable combustion of the propane–air mixture. In this case, the combustion-propagation rate increases compared to the case of the combustion stabilization by the OPD. This indicates the occurrence of preignition reactions in the radiation-focusing domain.

ACKNOWLEDGMENTS

REFERENCES

1. Yu. N. Molin, V. N. Panfilov, and A. K. Petrov, *Infrared Photochemistry* (Nauka, Novosibirsk, 1985).

2. R. Emrikh and R. I. Soloukhin, Fiz. Goreniya Vzryva **8** (1), 92 (1972).

3. J. Brossard, N. A. Fomin, and R. I. Soloukhin, Acta Astronaut. **6**, 861 (1979).

4. G. I. Kozlov, V. A. Kuznetsov, and A. D. Sokurenko, Pis'ma Zh. Tekh. Fiz. **16** (9), 55 (1990) [Sov. Tech. Phys. Lett. **16**, 345 (1990)].

5. G. I. Kozlov, V. A. Kuznetsov, and A. D. Sokurenko, Pis'ma Zh. Tekh. Fiz. **17** (11), 25 (1991) [Sov. Tech. Phys. Lett. **17**, 398 (1991)].

6. M. A. Tanoff, M. D. Smooke, R. E. Teets, and J. A. Sell, Combust. Flame **103** (4), 253 (1995).

7. A. M. Starik and N. S. Titova, Khim. Fiz. **19** (9), 61 (2000).

8. V. I. Yakovlev, P. K. Tretyakov, S. S. Vorontsov, and A. V. Tupikin, in *Proceedings of Symposium on Combustion and Explosion.* Part 1. *Chemical Physics of Combustion and Explosion Processes, Chernogolovka, 2000*, pp. 165–167.

9. E. S. Shchetinkov, *Physics of Gas Combustion* (Nauka, Moscow, 1965).

Translated by G. Merzon

═══════════════ **PHYSICS** ═══════════════

Hydrogen Ball Lightning

Yu. R. Alanakyan

Presented by Academician V.D. Rusanov February 12, 2002

When solving the problem of ball lightning, we need to answer a number of questions. The basic question relates to the form of the energy consumed for maintaining electric and other phenomena that accompany ball lightning. Furthermore, it is necessary to explain the autonomous character of the movement of ball lightning and to clarify the reason that it jumps off when colliding with dielectric media, i.e., possesses elastic properties, and why it is attracted to conductors. We also need to explain why ball lightning explodes on the mechanical disintegration of its structure. According to data collected and systematized by Stakhanov [1], the average lifetime τ of ball lightning, its average radius r, and energy U are approximately 10 s, 15 cm, and 10^4 J, respectively.

The ball-lightning model under consideration is based on the effect of the self-purifying of plasma from heavy particles. This effect was first observed by P. Kapitza [2], who obtained a plasma pinch in a mixture of light and heavy gases at atmospheric pressure. It turned out that heavy-atom ions were virtually absent in the plasma pinch. Theoretical analysis of the Kapitza effect was performed by the author in [3]. At the plasma–gas interface, a transition layer arises in which the ambipolar electric field is very intense. In this layer, molecules penetrating plasma from the ambient gas are ionized. Thus, only those ions which can overcome a potential barrier arrive at the volume occupied with plasma. This is accessible only for light hydrogen ions. At the same time, the penetration of heavy particles into the plasma volume is practically impossible. The ball lightning nucleates in the linear-lightning channel in which high-temperature plasma is formed. This plasma exists in the atmosphere for only about one thousandth of a second. However, it is capable of accumulating hydrogen ions in its volume during this time. Beyond the hot plasma, a layer of cold recombining plasma arises. Here, in the case of a sufficient amount of organic substances, favorable conditions for molecular polymerization appear.

Russian Research Centre Kurchatov Institute,
pl. Kurchatova 1, Moscow, 123182 Russia

Thus, the ball lightning is an object that contains hydrogen molecules and has an excess positive charge in its interior domain. Hydrogen gradually escapes through the porous shell and burns, whereas the presence of an electric field promotes the appearance of spark discharges. If the hydrogen flow from the interior domains is anisotropic, then a reactive force arises, which causes a displacement of the ball lightning. The object can be elastic, but a rupture of its shell results in an explosion since, in the conditions under consideration, the hydrogen oxidation has an explosive nature.

The presence in a ball lightning of a substance in a condensed state is confirmed by the following theoretical and experimental studies. After analyzing various elementary processes in gas media, Smirnov [4] concluded that the energy accumulated in a ball lightning is of a chemical nature. He constructed a corresponding fractal model. Bychkov [5] assumed the ball lightning to be similar to an electrically charged polymer net. Furthermore, this author emphasized that in a number of experiments [6–9], luminous balls were obtained in the case of a high-frequency discharge only in the presence of organic molecules in the atmosphere. For example, in [9], Slyusarev obtained a luminous red-white ball when studying the effect of an electric field on wood. In [10, 11], an assumption was made that a ball lightning is a supercooled dense plasma or a structural cluster consisting of excited atoms.

We now consider the process of accumulating hydrogen ion plasma formed in a linear-lightning discharge. As is well known [4], the linear-lightning channel has the following parameters: the plasma temperature is $T = 3 \times 10^4$ K, the lifetime is $t = 10^{-3}$ s, and the channel radius is approximately $\rho = 10$ cm. In this case, plasma is completely ionized, and the energy of the discharge is mainly spent for heating and ionizing particles penetrating the plasma from ambient air layers. A molecule arriving at the plasma dissociates into atoms that are then ionized by the electron impact. In this case, neutral particles before they have been ionized manage to fly a certain distance into plasma. Thus, at the plasma boundary, a transition zone arises in which both neutral and ionized particles are present. In this zone, the plasma is inhomogeneous, and an ambipolar electric field appears due to the charge separation. Electrons having maximal energy are emitted from the plasma into the environment

and, being cooled, form negative ions that are trapped by molecules. Charged particles are turned out to be separated in space, and an excess positive charge can be preserved in the volume after the plasma has recombined. The depth of the transition zone is determined by the distance passed by neutral particles in the plasma, which penetrate it from the ambient gas. The path length of a neutral atom before it is ionized by the electron impact can be found from the formula

$$l = \frac{v}{v_e}\frac{1}{n\sigma_i}e^{\frac{I}{T}},\qquad(1)$$

where v and v_e are the thermal velocities of a neutral atom and of an electron, respectively, n is the plasma concentration, I is the atomic ionization potential, and $\sigma_i = \pi e^2/I^2$ is the Thomson ionization cross section. It follows from formula (1) that a particle whose velocity and ionization potential are higher penetrates deeper into plasma. In the absence of light inert atoms, hydrogen atoms have the maximum flight length. Newly formed atoms either penetrate the plasma volume overcoming the potential barrier produced by the ambipolar electric field or are thrown by this field from the plasma. Evidently, it is simpler to overcome the potential barrier for particles that penetrated deeply into the plasma, i.e., for hydrogen atoms. That is why hydrogen being contained in the ambient gas is collected in the plasma volume.

It is worth noting that we assumed the motion of a neutral particle (its flight regime) to be collisionless until the moment when the ionization occurs. However, the allowance for friction between neutral particles and the counterrunning ion flow insignificantly affects the efficiency of the plasma self-purification.[1]

We indicate that during the discharge time (10^{-3} s) in a lightning channel which is in dynamic equilibrium with the ambient air, tens of ion generations change each other. In this case, hydrogen can fill in the plasma volume provided that there is a sufficient amount of molecules containing hydrogen atoms. They may be water molecules, organic molecules, or macromolecules carried by the air flux into the domain in which the lightning discharge occurs.

After the discharge maintaining the existence of plasma has ceased, the plasma is cooled and recombines in a time of 10^{-4}–10^{-5} s. Hydrogen molecules begin to diffuse into the ambient gas. If spreading of a hydrogen cluster occurs freely, then the diffusion time is $\tau_D \approx \rho^2/D$ (where D is the diffusivity of hydrogen molecules in air) and lasts on the order of several seconds. It is probable that the nature of a bead lightning is associated with the diffusion spreading and hydrogen burning in the atmosphere.

A long-lived object (ball lightning) arises when a medium hampering the hydrogen diffusion is formed about the hydrogen cluster. This may be, e.g., a porous polymeric medium. It is worth noting that under laboratory conditions, in the case of a sufficient concentration of organic molecules, the polymerization can occur in fractions of a second. In this case, the polymerization rate may considerably increase in the presence of ozone and negative oxygen ions in the atmosphere (see, e.g., [14]).

Finally, we estimate the energy capacity of a hydrogen ball. There is not more than 0.25 mole of hydrogen in the volume of an average ball lightning. In the process of producing water, while fusing with an equal amount of oxygen, about 7×10^5 J of thermal energy is released.

REFERENCES

1. I. P. Stakhanov, *Physical Nature of Ball Lightning* (Atomizdat, Moscow, 1979).
2. P. L. Kapitza, Zh. Éksp. Teor. Fiz. **57**, 1801 (1969) [Sov. Phys. JETP **30**, 973 (1970)].
3. Yu. R. Alanakyan, Pis'ma Zh. Éksp. Teor. Fiz. **31**, 518 (1980) [JETP Lett. **31** (9), 487 (1980)].
4. B. M. Smirnov, *The Problem of Ball Lightning* (Nauka, Moscow, 1988).
5. V. L. Bychkov, Preprint MFTI (Moscow Phys.-Tech. Inst., Moscow, 1992).
6. K. L. Korum and Dzh. Korum, Usp. Fiz. Nauk **160** (4), 47 (1990).
7. Dzh. Barri, *Ball Lightning and Bead Lightning* (Plenum, New York, 1980; Mir, Moscow, 1983).
8. H. Ofuruton and Y. H. Ohtsuku, Lett. Nuovo Cimento **13**, 761 (1990).
9. N. M. Slyusarev, in *Ball Lightning*, Ed. by B. M. Smirnov (Inst. of High Temp., Russ. Acad. of Sci., Moscow, 1990), pp. 18–29.
10. L. M. Biberman and G. É. Norman, Teplofiz. Vys. Temp. **7** (5), 822 (1969).
11. É. A. Manykin, M. I. Ozhovan, and P. P. Poluektov, Zh. Tekh. Fiz. **52** (7), 1474 (1982) [Sov. Phys. Tech. Phys. **27**, 905 (1982)].
12. Yu. R. Alanakyan, Pis'ma Zh. Éksp. Teor. Fiz. **26**, 133 (1977) [JETP Lett. **26**, 125 (1977)].
13. Yu. R. Alanakyan, Zh. Éksp. Teor. Fiz. **76**, 2046 (1979) [Sov. Phys. JETP **49**, 1036 (1979)].
14. Yu. A. Ivanov, N. M. Rytova, I. V. Soldatova, *et al.*, in *Plasma Chemistry-90*, Ed. by L. S. Polak (Inst. Petroleum Chemistry Syntheses, Russ. Acad. of Sci., Moscow, 1990), pp. 81–120.

Translated by G. Merzon

---

[1] The structure of the transition zone in a homogeneous gas under conditions inherent in the flight regime and diffusion regime was thoroughly analyzed in [12, 13].

On a Mechanism of Ball-Lightning Formation

Academician S. S. Grigoryan

The attention and efforts of researchers of a wide range of specialties have been attracted by the ball-lightning phenomenon for decades. Many hypotheses have been put forward for its explanation and possible laboratory reproduction; however, the problem remains unsolved. A leap forward was made by the late Prof. I.P. Stakhanov. In the journal *Nauka i Zhizn',* he called for everyone who had really observed ball-lightning to send him descriptions of the observations. He received a few thousand formal responses and carried out physical analysis and statistical processing of the collected materials. This allowed him to state a number of concepts characterizing the basic properties and parameters of ball-lightning, along with prerequisites for its formation, motion, and interaction with its "habitat," physical bodies, constructions, etc. These materials constituted the content of his remarkable book *On the Physical Nature of Ball-Lightning* [1]. Stakhanov also stated a theoretical concept on the nature of ball-lightning, which is known as the cluster hypothesis. According to this hypothesis, ball-lightning is conceived as a localized bunch of ions which are surrounded by shells composed of polar molecules (of water and other compounds produced in air); i.e., they are ion clusters that can exist without recombination over a long period of time (many seconds, tens of seconds, and several minutes).

According to eyewitness observations, ball-lightning is produced predominantly on streak lightning strokes near the ground and high in the atmosphere (aircraft-borne observations), as well as during "jump out" of radio and electric devices when there is no thunderstorm in the immediate vicinity.

Stakhanov's cluster hypothesis agrees well with the extensive observations presented in [1], i.e., with the existence of an effective surface tension for ball-lightning material; its ability to pass nondestructively through narrow holes and slots and to gather in "daughter" ball-lightnings on forced mechanical breakdown; and with estimates of its temperature, nonequilibrium glow, substance density, etc. However, the author failed to construct a real physical mechanism for the forma-

Institute of Mechanics, Moscow State University,
Michurinskiĭ pr. 1, Moscow, 117192 Russia

tion of a bunch of cluster ions. The reason is that the part of the energy released on a streak lightning discharge and the mass that are available for the production of an ion cluster cloud were incorrectly estimated on the basis of empirical data on ball-lightning parameters. In his book (p. 208), Stakhanov wrote that "almost all the discharge energy [of a streak lightning, S.G.], which, as we have seen, measures in the hundreds of kilojoules per meter of length, leaves the channel mainly in the form of radiation, its major part being stuck in the corona." Of course, this statement is wrong. It is common knowledge [2] that, on a streak lightning stroke, the duration of the air breakdown process producing a conductive channel, through which the electric discharge proceeds, and the duration of this discharge itself are much shorter than the duration of the radiation of the shock and acoustic waves from the channel. The breakdown and discharge continue for a few to a few tens of microseconds; i.e., an acoustic wave travels in air from a few fractions of a millimeter to a few centimeters in these times. Thus, the energy release in the breakdown channel is far too short and induces an intense shock wave (which is perceived as a loud sound, i.e., as thunder) propagating in environmental air. Shock-wave passage through air containing water vapor and a multitude of water drops (fog, rain, thunderstorm clouds themselves) results in the complete fragmentation of drops of water, their evaporation, dissociation, and ionization (together with air molecules) near the discharge channel axis. The intensity of these processes decreases sharply away from the channel. With some separation, even drop fragmentation ceases. (Of course, all distances corresponding to the successive termination of the cited processes can be calculated by solving the corresponding mixed gas-dynamic and gas-kinetic problem.) When the shock-wave front recedes, the gas pressure, density, and temperature will decrease, and the reverse processes, i.e., recombination, restoration of molecules, etc., will proceed in the medium produced by the shock wave. It is clear that there exists a range of distances from the channel axis at which the values of the initial parameters of the humid air generated by the shock wave and their subsequent decrease with time are such that there will be many ions on which cooled water-vapor molecules adhere, producing the ion hydrate clusters needed for

Stakhanov's scheme. Ion recombination is thus sharply retarded.

Upon completion of the fast stage of the hydrodynamic process, when the shock wave has gone to large distances, a long (cylindrical) heated-gas region whose outer part contains cluster plasma remains near the channel. This region as a whole begins to float up under the action of buoyancy. However, the emerging motion is nonuniform: since the discharge channel is not straight and heated gas floating in the channel and around it is convectively unstable, the floating-up configuration is strongly deformed and decays into separate fragments. The presence of cluster plasma in these fragments, which possesses, as was shown by Stakhanov [1], an effective surface tension, may result in the formation of compact plasma bunches, i.e., ball-lightning. In order for the formation of these bunches to be possible (before the classical plasma loses its capacity for compaction due to convective mixing in the floating-up process), the presence of a sharp initial nonuniformity in the heated region including initial local regions with high concentration of cluster plasma is essential. Such nonuniformities may arise at the branching sites of the streak lightning channel, in sites of enhanced initial moisture content of the air broken down by the lightning, and in sites where the lightning strikes electric conductors. Here, the sizable "point" absorption of the discharge electric current produces a local increase in the energy of "explosion," which is not cylindrical, as it is around the main channel of a lightning discharge, but concentrated. As a result, the initial cluster plasma mass and, consequently, the probability of the formation of a bunch from it (i.e., ball-lightning formation) increase sharply. Indeed, as was described in [1], ball-lightning often arose precisely in places where streak lightning struck conductors: metal bearings of transmission lines, metal spires on buildings, wet soil (plowed field), lake water, etc. The examples of such events described in [1] are as follows: (event no. 1 according to [1]) a streak lightning stroke to the spire of Bol'shoĭ Kremlin Palace produced two ball-lightnings; (no. 7) a ball-lightning arose in a streak lightning branching site; (nos. 20, 58) a streak lightning stroke to a steel bearing of a transmission line and to a tower produced a ball-lightning; (no. 28) a streak lightning stroke to a bank of a river produced a ball-lightning; (nos. 59, 64, 65, 70) a streak lightning stroke to a tree produced a ball-lightning; (nos. 63, 64, 69) a streak lightning stroke to the ground produced a ball-lightning; (no. 68) streak lightning struck lake water, and a ball-lightning "jumped out" of the water; (no. 66) a streak lightning stroke to wires near a pole produced a ball-lightning; (no. 62) a streak lightning stroke to a transformer substation produced a ball-lightning, etc.

Now, we perform some quantitative estimates for checking the plausibility of the proposed mechanism for producing both cluster plasma and bunches of it, i.e., producing ball-lightning. Since energy is released in the streak lightning channel in a short time, the subsequent gas-dynamic processes can be described with reasonable accuracy by using the exact solution found by academician L.I. Sedov to the problem of a strong explosion in gas with cylindrical symmetry [3]. By this solution, the distribution of gas-dynamic parameters around the symmetry axis of the problem in the cylindrical coordinates is of the form

$$v = \frac{2}{\gamma + 1}\dot{r}_f V(\xi), \quad \rho = \frac{\gamma + 1}{\gamma - 1}\rho_0 R(\xi),$$

$$p = \frac{2}{\gamma + 1}\rho_0 \dot{r}_f^2 P(\xi), \tag{1}$$

$$T = \frac{p}{R_0 \rho}, \quad \xi = \frac{r}{r_f(t)}.$$

Here, v, ρ, p, and T are the (radial) velocity, density, and absolute temperature of gas, respectively; r is the radial coordinate (the solution is independent of the axial z and azimuth θ coordinates; i.e., it is one-dimensional); t is the time; ρ_0 is the initial gas density, γ is the adiabatic index for the gas; R_0 is the gas constant; the dot above r_f denotes differentiation with respect to t; $V(\xi)$, $R(\xi)$, and $P(\xi)$ ($V(1) = R(1) = P(1) = 1$) are known explicit functions of ξ found by Sedov; and $r = r_f(t)$ is the following law of motion for a shock-wave front:

$$r_f(t) = \sqrt[4]{\frac{E_0}{\alpha(\gamma)\rho_0}t^2}. \tag{2}$$

Here, E_0 is the energy instantaneously released per unit length of the cylindrical explosion axis and $\alpha(\gamma)$ is a dimensionless number of the order of unity [3].

According to the estimates based on the observational data analysis, on a streak lightning discharge, the average energy released per one meter is 500 kJ; i.e., the values $E_0 = 500$ kJ/m $= 5 \times 10^{10}$ g cm/s² and $\rho_0 = \frac{1}{800}$ g/cm³ can be substituted into the solution given by Eqs. (1) and (2). For dry air, $\gamma = 1.4$; for air containing water vapor, γ has a value from 1.2 to 1.3. However, for such values of γ, dependence $\alpha(\gamma)$ can be neglected in Eq. (2). Thus, Eq. (2) takes the form

$$r_f(t) = 2.5 \times 10^3 \sqrt{t}. \tag{3}$$

Here, r_f is expressed in centimeters, and t, in seconds. At the shock-wave front ($r = r_f$, $\xi = 1$), we have (for $\gamma = 1.4$; the employment of $\gamma \sim 1.2$–1.4 does not change the order of magnitude):

$$v_f = \frac{2}{\gamma + 1}\dot{r}_f = 0.8\dot{r}_f = 10^3 t^{-1/2},$$

$$p_f = 0.8\rho_0\dot{r}_f^2 = 1.6 \times 10^{-3}p_0 t^{-1},$$

$$\rho_f = \frac{\gamma + 1}{\gamma - 1}\rho_0 = 6\rho_0, \quad T_f = \frac{p_f\rho_0}{p_0\rho_f}T_0 \qquad (4)$$

$$= \frac{\gamma - 1}{\gamma + 1}\frac{p_f}{p_0}T_0 = 0.27T_0 t^{-1},$$

where p_0 and T_0 are the initial pressure and temperature, respectively. For 5×10^{-6} s $\le t \le 10^{-3}$ s, we obtain the results presented in the table.

For distances from the axis that are less than the distance corresponding to $t = 5$ μs, the solution is not described by Eqs. (1) and (2); in this region, it is substantial that energy is released in the discharge channel gradually. The last two rows in the table are also unsuitable for the process description: the effect of the initial atmospheric pressure p_0 is essential at this stage. The main error is introduced by the relationship $\frac{\rho_f}{\rho_0} = \frac{\gamma + 1}{\gamma - 1}$, which, in particular, distorts T_f. Nevertheless, the calculation gives correct estimates up to the distances $r_f \sim 0.3$ m, and in this range, the temperature conditions make possible the above-mentioned processes, which result in the production of the required cluster plasma volume. This statement is also justified by the fact that, according to the self-similar solution given by Eqs. (1) and (2), the temperature downstream from the shock-wave front sharply increases as the symmetry axis ("explosion" axis) is approached and tends to infinity on this axis. The temperature also increases with time for fixed r, until the effect of the initial pressure p_0 changes the solution completely and terminates this increase in temperature. The figure qualitatively shows the shock-wave front and isotherms for the self-similar solution (at the bottom) and for the exact solution (above). The real solution differs from Eqs. (1) and (2) also in the vicinity of the axis $r = 0$, where, according to Eqs. (1) and (2), temperature gradients are very large, and, hence, heat conduction is essential, and all gas-kinetic processes, including those responsible for the formation of the cluster plasma, are different.

Nevertheless, the above estimates and reasoning show that there are favorable conditions for cluster plasma production in the example under consideration in a cylinder with radius 0.3 m. Stakhanov [1] estimated the air volume required to produce such plasma with mass corresponding to a medium ball-lightning 20 cm in diameter. For an initial mass of saturated water vapor equal to 15.42 g per 1 m³, this volume is equal to 0.5 m³. According to the above estimates, this volume is obtained for max $r_f(t) = 0.25$ m for a section of streak
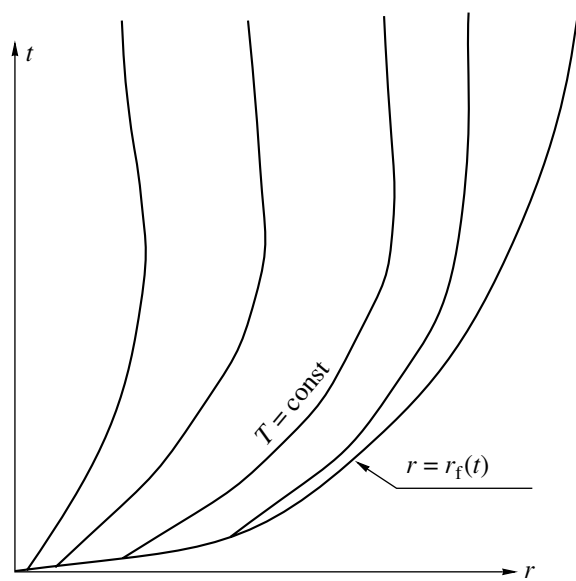

Figure.

lightning of length $l \approx 2.5$ m ($l \approx 2$ m for max $r_f(t) = 0.3$ m). This is in good agreement with the above mechanism of the formation of cluster plasma bunches, when a heated air region, which is left after the shock wave has moved away, floats up and disintegrates into separate fragments. Since the real water concentration in the initial air volume may be much higher (from one to two orders of magnitude in the presence of a dense fog of drops and at a lightning stroke to water-bearing obstacles: soil while it rains, a water reservoir, a tree; see the above examples), a strong shock wave induced by a streak lightning discharge can undoubtedly create the conditions for the production of the required cluster-plasma mass and the formation of ball-lightning from it.

A ball-lightning production mechanism independent of streak-lightning discharge (from radio and electrotechnical devices) is briefly outlined in [1]. This is a powerful corona discharge through an air gap, which is induced by energy accumulated in lines and devices with sizable electric capacitance when they become charged in the electrostatic field of a nearby thunder-

Table

t, μs	r_f, cm	v_f, km/s	p_f, kg/cm²	T_f, K
5	5.6	4.2	320	16 200
10	8.0	3.0	160	8100
50	17.7	1.3	32	1620
100	25.3	0.95	16	810
500	56	0.42	3.2	162
1000	80	0.3	1.6	81

storm. In these cases, the cluster plasma is produced by the "hydration" of ions which are created by the corona discharge, not necessarily by water molecules, but also by molecules of other compounds produced by a strong corona discharge as well.

From the above discussion, it follows that ball-lightning can in principle be produced artificially. This can be arranged by producing a moisture-laden atmosphere with a variable concentration of vapor and water drops within a volume insulated by firm walls (it is desirable to have transparent sections in them). In this medium, a powerful linear explosion with controlled energy should be fired, for example, by passing pulse electric current through a thin linear conductor (the well-known scheme of an exploding wire). If Stakhanov's cluster hypothesis is correct, ball-lightning will be generated under appropriate parameters in this experiment.

REFERENCES

1. I. P. Stakhanov, *About the Physical Nature of a Ball-Lightning* (Nauchnyĭ Mir, Moscow, 1996).
2. I. S. Stekol'nikov, Lightning, in *Physical Encyclopedic Dictionary* (Sovetskaya Éntsiklopediya, Moscow, 1963), Vol. 3, pp. 307–309.
3. L. I. Sedov, *Similarity and Dimensional Methods in Mechanics* (Nauka, Moscow, 1981; Academic, New York, 1959).

Translated by V. Tsarev

Analysis of the Space–Time Characteristics of the Resulting Radiation from Linear Antenna Arrays for Ultrashort Pulses in the Case of Sequential Activation and Arbitrary Input Signals

Corresponding Member of the RAS L. D. Bakhrakh* and M. Ya. Izrailovich**

Received April 15, 2002

The operating efficiency of ultrashort-pulse antenna arrays can be estimated by analyzing the space–time intensity structure of emitted signals. In addition, it is necessary to take into account the interaction between the radiation of each of the antennas turned on sequentially in time.

To date, the methods of such an analysis have been developed as applied to a certain fixed shape of a working signal arriving at the input of each antenna and, as a consequence, a signal emitted by the antenna. These signals have identical time diagrams with a certain time delay.

In this study, we consider a method for analysis of the resulting radiation from a linear array for arbitrary signals applied to the inputs of antennas turned on sequentially, and, in general, being different from each other. Such a generality is appropriate from the standpoint of the expanded possibilities associated with a purposeful action on both the focusing of a resulting signal and the improvement of the operating efficiency of the arrays. At the same time, this generality enables us to use ultrashort-pulse generators with different characteristics.

1. The space–time emission characteristic of a single antenna (in the plane approximation) can be written out in the form

$$y(t, \varphi) = f(\varphi)z(t), \qquad (1)$$

where $y(t, \varphi)$ is the intensity of the emitted signal at the time moment t along the direction with the angular coordinate φ; $f(\varphi)$ is the directivity pattern of the emitted signal, which is assumed to be a continuous and continuously differentiable function symmetric about

the value $\varphi = \dfrac{\pi}{2}$; and $z(t)$ is the time diagram of the emitted signal:

$$z(t) = \int_0^t h(t - \tau)x(\tau)d\tau, \quad t \in (0; T_1],$$

$$z(t) = \int_0^{T_1} h(t - \tau)x(\tau)d\tau, \quad t \in (T_1; \infty). \qquad (2)$$

Here, $h(t - \tau)$ is the pulse transient function of the antenna considered as a linear steady system; $x(t)$ is the time diagram of a signal produced by an ultrashort-pulse generator and applied to the antenna's input; and $x(t) = 0$ (at $t > T_1$), where T_1 is the duration of the input signal.

In view of relationship (2), expression (1) for the intensity of an emitted signal takes the form

$$y(t, \varphi) = f(\varphi)\int_0^t h(t - \tau)x(\tau)d\tau, \quad t \in (0; T_1],$$

$$y(t, \varphi) = f(\varphi)\int_0^{T_1} h(t - \tau)x(\tau)d\tau, \quad t \in (0; \infty). \qquad (3)$$

2. A linear array represents n antennas arranged along a straight line and spaced equidistantly at a distance l from each other (Fig. 1). The antennas are sequentially activated with a time delay T $(T > T_1)$ from left to right.

In the general case, at the moment when the ith antenna $(1 < i \le n)$ is turned on, the effect of the radiation of all preceding antennas is present.

Figure 2 shows the calculation scheme that makes it possible to determine the cumulative effect of the antenna's emissions. At a point with the abscissa p and the ordinate s, the effect of the total emission is determined by the summation of the radiation intensities from i antennas (i.e., from both $i - 1$ preceding antennas and

_____

* *Moscow Research Institute of Instrument Building,*
 Kutuzovskiĭ pr. 34, Moscow, 121170 Russia
** *Blagonravov Institute of Engineering Science,*
 Russian Academy of Sciences,
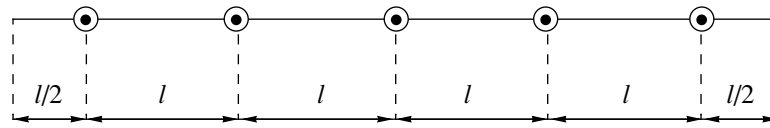 *ul. Bardina 4, Moscow, 117334 Russia*

Fig. 1. Linear antenna array.

the ith antenna emitting within a given time interval). Therefore, in accordance with expression (3), the overall emission effect of a single antenna can be written as

$$y_\Sigma(t, p, s) = \sum_{j=0}^{i-2} f(\varphi_{j+1}) \int_{jT}^{jT+T_1} h(t-\tau)x_{j+1}(\tau)d\tau$$

$$+ f(\varphi_i) \int_{(i-1)T}^{t} h(t-\tau)x_i(\tau)d\tau,$$

$$t \in ((i-1)T; (i-1)T+T_1], \qquad (4)$$

$$y_\Sigma(t, p, s) = \sum_{j=0}^{i-1} f(\varphi_{j+1}) \int_{jT}^{jT+T_1} h(t-\tau)x_{j+1}(\tau)d\tau,$$

$$t \in ((i-1)T+T_1; iT],$$

$$i = 2, 3, \ldots, n,$$

where $x_j(t)$ is the input signal for the jth antenna; the angles φ_j for the jth antenna are the functions of the coordinates p and s at the point under consideration:

$$\varphi_j = \arctan\frac{s}{\left(j-\dfrac{1}{2}\right)l - p}.$$

When the input signals with the same time diagram $x(t)$ are applied to the input of each of the antennas [i.e., $x(t)$ is a periodic function with a period T], it is appropriate to transform the integration limits to the interval $(0, T_1)$ of the function definition interval. As a result, expression (4) takes the form

$$y_\Sigma(t, p, s) = \int_0^{T_1}\sum_{j=0}^{i-2} f(\varphi_{j+1})h(t-\tau-jT)x(\tau)d\tau$$

$$+ \int_0^{t-(i-1)T} f(\varphi_i)h(t-\tau+T-iT)x(\tau)d\tau,$$

$$t \in ((i-1)T; (i-1)T+T_1],$$

$$y_\Sigma(t, p, s) = \int_0^{T_1}\sum_{j=0}^{i-1} f(\varphi_{j+1})h(t-\tau-jT)x(\tau)d\tau, \qquad (5)$$

$$t \in ((i-1)T+T_1; iT],$$

$$i = 2, 3, \ldots, n.$$

For repetitive input signals, expression (5) has an advantage over the general expression (4), since makes it possible to express the intensity y_Σ directly within the definition range of $x(t)$.

The maximum intensity of the emitted signal at a distance s from the antenna array at a time t is determined by the maximization of the expression $y_\Sigma(t, p, s)$ [either (4) or (5)] over the abscissa p:

$$\tilde{y}_\Sigma(t, s) = \max_p y_\Sigma(t, p, s). \qquad (6)$$

The function $\tilde{y}_\Sigma(t, s)$ exhaustively describes the space–time radiation structure of the antenna array for ultrashort pulses. This function determines the array emission intensity at an arbitrary time t and at an arbitrary distance s. The maximizing value of $p = p^*$ in Eq. (6) determines the value of the abscissa at the corresponding point, where the emission-intensity maximum exists.

3. As was assumed above, at the moment when the ith antenna is turned on, it is necessary to take into account the residual radiation of all preceding $i - 1$ antennas. However, by using methods of correcting signals emitted by the ultrashort-pulse antennas (in particular, the methods developed in [1–3]), it is possible, in principle, to provide conditions of the complete absence of a signal for a relatively short period of time. In this case, the signal

$$x(t) = x_0(t) + u(t)$$

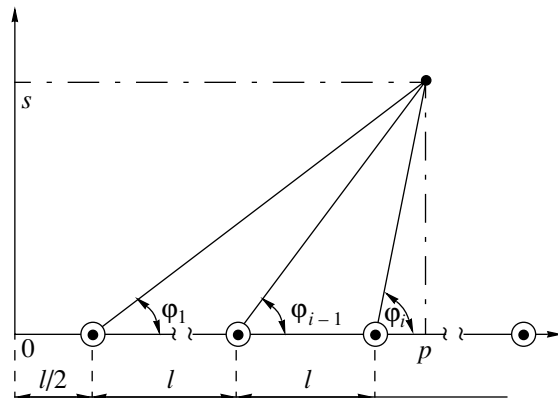is sequentially applied to each antenna input. Here, $x_0(t)$

Fig. 2. Scheme for calculating the intensity of the resulting signal.

is the signal produced by the generator and $u(t)$ is the correcting (controlling) signal calculated in such a way that, at a given moment T_2, the signal emitted by the antenna completely decays; i.e., $y(T_2) = 0$. Furthermore, we assume that $T_2 = kT$, where k is a positive integer ($k < n$). In this case, at $t \in (0; kT)$, expressions (4) and (5) for $y_\Sigma(t, p, s)$ remain the same, whereas at $t > kT$, they transform to the following forms. Expression (4) transforms to

$$y_\Sigma(t, p, s) = \sum_{j=i-1-k}^{i-2} f(\varphi_{j+1}) \int_{jT}^{jT+T_1} h(t-\tau)x_{j+1}(\tau)d\tau$$

$$+ f(\varphi_i) \int_{(i-1)T}^{t} h(t-\tau)x_i(\tau)d\tau,$$

$$t \in [(i-1)T; (i-1)T + T_1], \qquad (7)$$

$$y_\Sigma(t, p, s) = \sum_{j=i-1-k}^{i-2} f(\varphi_{j+1}) \int_{jT}^{jT+T_1} h(t-\tau)x_{j+1}(\tau)d\tau,$$

$$t \in [(i-1)T + T_1; iT],$$

$$i = k+1, \ldots, n;$$

and expression (5) transforms to

$$y_\Sigma(t, p, s) = \int_0^{T_1} \sum_{j=i-1-k}^{i-2} f(\varphi_{j+1})h(t-\tau-jT)x(\tau)d\tau$$

$$+ f(\varphi_i) \int_0^{t-(i-1)T} h(t-\tau-iT+T)x(\tau)d\tau,$$

$$t \in [(i-1)T; (i-1)T + T_1], \qquad (8)$$

$$y_\Sigma(t, p, s) = \int_0^{T_1} \sum_{j=i-1-k}^{i-1} f(\varphi_j)h(t-\tau-jT)x(\tau)d\tau,$$

$$t \in ((i-1)T + T_1; iT],$$

$$i = k+1, k+2, \ldots, n.$$

In this case, the basic characteristic (6) of the emission intensity $\tilde{y}_\Sigma(t, s)$ must be calculated on the basis of either the expression $y_\Sigma(t, p, s)$ (7) or (for identical input signals) expression (8).

The advantage of these operating regimes of sequentially activated antennas is the possibility of more accurate focusing and control of the resulting emission, since, in the general case, the emission is spread due to the residual radiation of all preceding antennas.

REFERENCES

1. L. D. Bakhrakh and M. Ya. Izrailovich, Antenny **2** (48), 45 (2001).

2. L. D. Bakhrakh and M. Ya. Izrailovich, Dokl. Akad. Nauk **379**, 325 (2001) [Dokl. Phys. **46**, 491 (2001)].

3. L. D. Bakhrakh and M. Ya. Izrailovich, Dokl. Akad. Nauk **380**, 338 (2001) [Dokl. Phys. **46**, 647 (2001)].

Translated by Yu. Vishnyakov

TECHNICAL PHYSICS

Surface Tension at the Interface of Materials as a Function of Impurity Content

R. V. Gol'dshtein* and M. E. Sarychev**

Presented by Academician A.Yu. Ishlinskiĭ April 1, 2002

In studies [1,2], it was shown that the concentration of crystal-structure defects such as vacancies and dislocations can substantially affect the surface tension coefficient γ_{12} at the interface between two crystalline materials. In turn, this coefficient appreciably determines the resistance of the joint to the growth of cracks at the interface. In this study, we consider the important applied problem of the effect of impurity content in the materials forming the interface on the coefficient γ_{12}.

Let each of the adjoining materials 1 and 2 contain its own impurity. These impurities are also designated by the numbers 1 and 2, respectively. As in [1, 2], we apply the thermodynamic method based on the Gibbs equation [3] relating a change $d\gamma_{12}$ in the surface tension γ_{12} to changes in the chemical potentials of the components of materials 1 and 2 (in this case, these are the impurities and matrices of the corresponding material). For constant temperature and pressure in the system under consideration, this equation has the form

$$d\gamma_{12} = -\Gamma_1^{(0)}d\mu_1^{(0)} - \Gamma_1 d\mu_1 - \Gamma_2^{(0)}d\mu_2^{(0)} - \Gamma_2 d\mu_2, \quad (1)$$

where $d\mu_i^{(0)}$ and $d\mu_i$ are the changes in chemical potentials $\mu_i^{(0)}$ and μ_i of the matrix and impurity of the ith material $i = 1, 2$, respectively; $\Gamma_i^{(0)}$ and Γ_i are the number of matrix and impurity atoms, respectively, for the ith material in the interface (per unit area).

Since interstitial-impurity atoms are arranged in interstitial sites of the matrix, we can assume that the concentration of matrix atoms (i.e., their chemical potential) is constant when the concentration of impurity atoms (i.e., their chemical potential) varies. In this case, $d\mu_1^{(0)} = d\mu_2^{(0)} = 0$ for the interstitial impurity and

---

 * Institute for Problems in Mechanics,
   Russian Academy of Sciences,
   pr. Vernadskogo 101, Moscow, 117526 Russia
** Institute for Physics and Technology,
   Russian Academy of Sciences, Moscow, Russia

Eq. (1) takes the form

$$d\gamma_{12} = -\Gamma_1 d\mu_1 - \Gamma_2 d\mu_2. \quad (2)$$

At the same time, the concentration C_i of the substitutional-impurity atoms varies due to the varying matrix–atom concentration $C_i^{(0)}$.

Using the Gibbs–Duhem equation for volumes of each of the adjoining materials (also for constant pressure and temperature) [3]

$$C_i^{(0)}d\mu_i^{(0)} + C_i d\mu_i = 0$$

and neglecting the low vacancy concentration for the substitutional impurity, i.e., taking $C_i^{(0)} + C_i = 1$, we reduce Eq. (1) to the form

$$d\gamma_{12} = -\left(\Gamma_1 - \Gamma_1^{(0)}\frac{C_1}{1 - C_1}\right)d\mu_1$$

$$-\left(\Gamma_2 - \Gamma_2^{(0)}\frac{C_2}{1 - C_2}\right)d\mu_2, \quad (3)$$

which takes the form of Eq. (2) for low concentrations $C_i \ll 1$ of the substitutional impurity, when the effect of both types of impurities can be considered using only Eq. (2). However, since the case of high concentrations C_i is also of great interest, we further analyze both Eqs. (2) and (3). In order to solve them, it is necessary to find the dependences of quantities $\mu_{1,2}$, $\Gamma_{1,2}^{(0)}$, and $\Gamma_{1,2}$ on impurity concentrations C_1 and C_2 in the bulk of materials 1 and 2.

Following [4], we find μ_i, $i = 1, 2$, on the basis of the ith-material free energy F_i involving the configuration entropy of impurity atoms. We assume that the impurity atoms do not interact with each other and that two arbitrary atoms cannot occupy the same atomic site (or interstitial site) simultaneously:

$$F_i = F_{i0} + n_i E_i - kT\ln\frac{N_i!}{(N_i - n_i)!n_i!}, \quad (4)$$

where F_{i0} is the free energy of the ith material without impurity; E_i is the reversible work necessary for the

implantation of the ith-impurity atom into the ith material; and N_i and n_i are the number of atomic sites (for the substitutional impurity) or interstitial sites (for the interstitial impurity) and the number of impurity atoms in the ith material, respectively. Then, using the Stirling formula and differentiating Eq. (4) with respect to n_i, we obtain the chemical potential $\mu_i = \dfrac{\partial F_i}{\partial n_i}$ in the form

$$\mu_i = E_i + kT \ln \frac{n_i}{N_i - n_i} = E_i + kT \ln \frac{C_i}{1 - C_i}, \qquad (5)$$

where $C_i = \dfrac{n_i}{N_i}$ is the impurity concentration in the bulk of the ith material.

It should be noted that Eq. (5) is applicable both for interstitial and substitutional impurities, because the configuration entropy in (4) is written identically in both cases [4]; a distinction is determined only by the value of E_i. In addition, it was shown in [4] that the approximation of noninteracting impurity atoms used in Eq. (4) is also reasonably good for extremely high concentrations $C_i < 1$, because there are no obstacles for a random local distribution of impurity atoms in this case as well. There is only short-range repulsion, due to which two atoms cannot occupy the same atomic site (interstitial site). Thus, we further use Eq. (3) for arbitrary $C_i < 1$. Finally, we here neglect external and internal pressure in the system for the sake of simplicity. Otherwise, the Gibbs thermodynamic potential $\Phi_i = F_i + p_i v_i$ (p_i is the pressure in the ith material, and v_i is its volume) should be used instead of free energy F_i [4].

For finding the quantities Γ_1 and Γ_2 in Eqs. (2) and (3), we consider an interface as a surface absorbing structural defects (in the case under consideration, these are impurities) [3, 4]. In addition, it is assumed that the adsorption and desorption of impurities by the interface proceed independently for each of them, and ith-impurity atoms can be desorbed only backwards into the same material. The latter property can be ensured by, e.g., a high energy barrier for their desorption into another material (see also [1], where a similar model was used for vacancies).

Thus, Γ_i can be written according to Eq. (1) as follows:

$$\Gamma_i = \frac{n_{Ii}}{v_{Ii}} b = C_{Ii} \frac{b}{\Omega_i}, \quad i = 1, 2, \qquad (6)$$

where n_{Ii} and $C_{Ii} \equiv \dfrac{n_{Ii}}{N_I}$ are the number of ith-impurity atoms and their concentration at the interface, respectively; N_I is the number of sites (in the case of the substitutional impurity) or interstitial sites (for the interstitial impurity) in the interface; b is the interface thickness; and Ω_i is the volume per site (interstitial site) in the ith material. According to the accepted model of the

interface, the kinetics of the concentration C_{Ii} are described by the following equations:

$$\frac{dC_{Ii}}{dt} = k_{ai}(1 - C_{Ii})C_i - k_{di}C_{Ii}(1 - C_i), \qquad (7)$$

where k_{ai} and k_{di} are the adsorption and desorption constants, respectively, for the process of exchange by impurity atoms between the interface and ith material. In the steady-state regime $\left(\dfrac{dC_{Ii}}{dt} = 0\right)$, Eq. (7) gives

$$C_{Ii} = \frac{h_i C_i}{1 + (h_i - 1)C_i}, \qquad (8)$$

where $h_i = \dfrac{k_{ai}}{k_{di}}$.

By their definition [see (1)], the quantities $\Gamma_i^{(0)}$ in Eq. (3) for the substitutional impurity are related to the concentrations $C_{Ii}^{(0)}$ of matrix atoms similar to Eq. (6). If, as for the bulk concentrations, vacancies are ignored, then $C_{Ii}^{(0)} + C_{Ii} = 1$, and $\Gamma_i^{(0)}$ are given by the expressions

$$\Gamma_i^{(0)} = C_{Ii}^{(0)} \frac{b}{\Omega_i} = (1 - C_{Ii}) \frac{b}{\Omega_i}. \qquad (9)$$

Now, substituting Eqs. (5), (6), (8), and (9) into Eqs. (2) and (3), we obtain equations enabling us to find $\gamma_{12} = \gamma_{12}(C_1, C_2)$. However, it is useful to first analyze γ_{12} for the particular case of an inner interface in one material (i.e., $C_1 = C_2 = C$). For example, this can be the grain boundary (GB) in a polycrystalline material.

1. The surface tension of the grain boundary [$\gamma_{12} \equiv \gamma_{GB}(C)$] is described by the following one-component equation instead of two-component Gibbs equations (2) and (3) (see also [3]):

$$d\gamma_{GB} = -\Gamma d\mu, \qquad (10a)$$

$$d\gamma_{GB} = -\left(\Gamma - \Gamma^{(0)} \frac{C}{1 - C}\right) d\mu, \qquad (10b)$$

where the quantities introduced in Eq. (1) now correspond to one material and one type of impurity. Thus, Eqs. (4)–(8) above are all valid, but it is necessary to omit the subscript i in them.

Then, substituting Eqs. (5), (6), (8), and (9) without the subscript i into Eqs. (10a), (10b), we obtain the following equation for γ_{GB}:

$$\frac{d\gamma_{GB}}{dC} = -\frac{bkT}{\Omega} A(h) \frac{1}{1 + (h - 1)} \frac{1 - 2C}{1 - C}, \qquad (11)$$

where $A(h) = h$ for the interstitial impurity and $A(h) = h - 1$ for the substitutional impurity. Equating the right-hand side of Eq. (11) to zero, we find that $\gamma_{GB}(C)$ for the

interstitial impurity has a minimum at $C = C_m = \frac{1}{2}$ both for $h > 1$ (grain boundary is a good absorber of impurity atoms) and for $h < 1$ (grain boundary is a poor absorber). At the same time, the surface tension γ_{GB} for the substitutional impurity at $C = \frac{1}{2}$ has a minimum for $h > 1$ and a maximum for $h < 1$.

The integration of Eq. (11) gives

$$\gamma_{GB}(C) = \gamma_{GB}^{(0)} - \frac{bkT}{\Omega} g(h)$$

$$\times \left\{ \frac{h+1}{h-1} \ln[1 + (h-1)C] + \ln(1-C) \right\}, \quad (12)$$

where $g(h) = \frac{A(h)}{h}$ and $\gamma_{GB}^{(0)} = \gamma_{GB}(0)$ is the surface tension of the grain boundary without an impurity; i.e., it is assumed in Eq. (12) that the impurity concentration in a material is determined by external sources and that, therefore, its minimum value is zero.

In the cases where function (12) has a minimum at $C = \frac{1}{2}$, it rises for $C > \frac{1}{2}$ and can be substantially higher than $\gamma_{GB}^{(0)}$ if $C \longrightarrow 1$. In this case, substituting $C = C_m = \frac{1}{2}$ into Eq. (12), we find that the surface tension of the grain boundary $\gamma_{GB}^{(m)} = \gamma_{GB}(C_m)$ is given by the expression

$$\gamma_{GB}^{(m)} = \gamma_{GB}^{(0)} - \frac{bkT}{\Omega} g(h) \left\{ \frac{h+1}{h-1} \ln\frac{h+1}{2} - \ln 2 \right\}; \quad (13)$$

i.e., $\gamma_{GB}^{(m)}$ decreases with increasing h and can become negative if the following condition is satisfied:

$$f(h) \equiv g(h) \left\{ \frac{h+1}{h-1} \ln\frac{h+1}{2} - \ln 2 \right\} > \frac{\gamma_{GB}^{(0)} \Omega}{bkT}. \quad (14)$$

In this case, $\gamma_{GB} < 0$ for $C_1^* < C < C_2^*$, where $C_1^* < \frac{1}{2}$ and $C_2^* > \frac{1}{2}$ are the roots of the equation that is obtained when the right-hand side of (12) is equal to zero. For a quite deep minimum in Eq. (13), $C_1^* \ll \frac{1}{2}$; i.e., γ_{GB} can become negative even at low impurity concentrations. The analysis of the function $f(h)$ in Eq. (14) shows that it steadily grows from zero at $h = 0$ and 1 for the interstitial impurity ($g(h) = 1$) and substitutional

impurity with $h > 1$ $\left(g(h) = \frac{h-1}{h} \right)$, respectively, to

$$f \sim \ln\frac{h}{2} \longrightarrow \infty$$ at $h \gg 1$ for both these types of impurity. Since the right-hand side of (14) is positive, condition (11) can always be satisfied for sufficiently high h values. In other words, for arbitrary parameters b, T, and Ω and any $\gamma_{GB}^{(0)}$, condition (14) can be satisfied, i.e., $\gamma_{GB}^{(m)} < 0$, if the grain boundary is a sufficiently good absorber of impurity (i.e., h is sufficiently high). Whether or not real polycrystalline materials have such properties is another matter.

We estimate the relation between the adsorption and desorption characteristics of the grain boundary for which condition (14) is satisfied in real cases. Let $\gamma_{GB}^{(0)} \simeq 0.3$ J/m² (a typical value for the grain boundary of many metals [5]), $\Omega \sim 10^{-29}$ m³, $b \sim 5$ Å, and $kT \cong 0.025$ eV (room temperature). In this case, we find from Eq. (14) that $h > 10^2$. Therefore, in view of the Arrhenius form of the temperature dependence of the adsorption and desorption constants $k_a \sim \exp\left(-\frac{E_a}{kT}\right)$ and $k_d \sim \exp\left(-\frac{E_d}{kT}\right)$ $\left(\text{i.e., } h \sim \exp\frac{E_a - E_d}{kT} \right)$, the activation energies E_a and E_d of the corresponding processes satisfy the relationship $E_d - E_a \geq 0.2$ eV, which does not seem completely unrealizable. For example, in the framework of this estimate, we have $\gamma_{GB}^{(m)} \simeq -0.2$ J/m² for $h = 10^3$.

For the substitutional impurity with $h < 1$, function (12) for $\gamma_{GB}(C)$ has a maximum $\gamma_{12}\left(\frac{1}{2}\right) > 0$ at $C = C_m = \frac{1}{2}$, which is determined by Eq. (13) with $g(h) = \frac{h-1}{h} < 0$; i.e., the quantity $\gamma_{12}(C)$ is negative for $1 > C > C^* > \frac{1}{2}$, where C^* is a root of the equation

$$(1 - C)^{h-1}[1 + (h-1)C]^{h+1} = 1.$$

2. We now return to the case of an interface formed by two various materials involving different impurities of the same type.

In this case, the two-component Gibbs equation (1) for $\gamma_{12}(C_1, C_2)$ with allowance for Eqs. (5), (6), and (8) can be integrated independently with respect to C_1 and

C_2 [this is possible because $\Gamma_1 = \Gamma_1(C_1)$, $\mu_1 = \mu_1(C_1)$ and $\Gamma_2 = \Gamma_2(C_2)$, $\mu_2 = \mu_2(C_2)$], and we obtain

$$\gamma_{12}(C_1, C_2) - \gamma_{12}^{(0)} = -\frac{bkT}{\Omega_1}g(h_1)$$

$$\times\left\{\frac{h_1+1}{h_1-1}\ln[1+(h_1-1)C_1]+\ln(1-C_1)\right\} \quad (15)$$

$$-\frac{bkT}{\Omega_{21}}g(h_2)\left\{\frac{h_2+1}{h_2-1}\ln[1+(h_2-1)C_2]+\ln(1-C_2)\right\},$$

where $g(h_i) = 1$ and $g(h_i) = \dfrac{h_i - 1}{h_i}$ for the interstitial and substitutional impurities, respectively. Thus, $\gamma_{12}(C_1, C_2)$ can be represented as the sum of two terms each of which have form (12). Therefore, $\gamma_{12}(C_1, C_2)$ has minima at $C_1 = \dfrac{1}{2}$ as a function of C_1 and at $C_2 = \dfrac{1}{2}$ as a function of C_2 for the interstitial impurities with arbitrary h_i and for the substitution impurities with $h_i > 1$. At the same time, it is of interest to determine whether or not $\gamma_{12}(C_1, C_2)$ has a minimum as a function of two variables. Analysis of $\gamma_{12}(C_1, C_2)$ and its second derivatives $\dfrac{\partial^2 \gamma_{12}}{\partial C_1^2}$, $\dfrac{\partial^2 \gamma_{12}}{\partial C_2^2}$, and $\dfrac{\partial^2 \gamma_{12}}{\partial C_1 \partial C_2}$ shows that the function $F = -\gamma_{12}$ has a maximum at $C_1 = C_2 = \dfrac{1}{2}$. Therefore, $\gamma_{12}(C_1, C_2)$ actually has a maximum at these values of C_1 and C_2. According to Eq. (15), for substitutional impurities with $h_i < 1$ $\gamma_{12}(C_1, C_2)$ it has a maximum at $C_1 = C_2 = \dfrac{1}{2}$.

Similarly to Eq. (13), $\gamma_{12}^{(m)} = \gamma_{12}\left(\dfrac{1}{2}, \dfrac{1}{2}\right)$ is given by the expression

$$\gamma_{12}^{(m)} = \gamma_{12}^{(0)} - \frac{bkT}{\Omega_1}g(h_1)\left[\frac{h_1+1}{h_1-1}\ln\frac{1+h_1}{2} - \ln 2\right]$$

$$-\frac{bkT}{\Omega_2}g(h_2)\left[\frac{h_2+1}{h_2-1}\ln\frac{1+h_2}{2} - \ln 2\right]. \quad (16)$$

As in the case of Eq. (13), analyzing dependence (16) on h_1 and h_2, one can find the domains of h_1 and h_2 within which $\gamma_{12}^{(m)} < 0$. This inequality is certainly satisfied for sufficiently large h_1 and h_2.

In particular, for $h_1, h_2 \gg 1$ (in this case, there is no distinction between the actions of the interstitial and substitutional impurities; i.e., $g(h_i) = 1$) and under the assumption that $\Omega_1 \sim \Omega_2 = \Omega$, we find from Eq. (15) that

$$\gamma_{12}^{(m)} = \gamma_{12}^{(0)} - \frac{bkT}{\Omega}\ln\frac{h_1 h_2}{16}.$$

Therefore, the condition that $\gamma_{12}^{(m)} < 0$ takes the form

$$h_1 h_2 > 16\exp\left(\frac{\gamma_{12}^{(0)}\Omega}{bkT}\right). \quad (17)$$

Considering the metal–metal interface (typical $\gamma_{12}^{(0)} \sim$ 1 J/m² [1]) and using the same values as above ($\Omega \simeq 10^{-29}$ m³, $b \simeq 5$ Å, and $kT \simeq 0.025$ eV) for the remaining values, we obtain the estimate $h_1 h_2 > 10^3$ from Eq. (17). For example, $\gamma_{12}^{(m)} \simeq -0.4$ J/m² for $h_1 h_2 \simeq 10^4$ in this case.

The possibility of satisfying the inequality $\gamma_{12} < 0$ means that the introduction of impurities makes the formation of a joint between given materials certainly more energetically advantageous than the existence of their free surfaces. Correspondingly, the spontaneous formation of microcavities along the joint interface becomes less advantageous, because free surfaces of materials appear in this case. The latter process corresponds to the fact that the interface becomes more stable against the spontaneous peeling of materials.

Thus, the effect of impurities on the surface tension of interfaces of materials is nonmonotonic and so substantial that surface tension can change sign at reasonably high concentrations. In this case, the character of the effect depends on the type of impurity (interstitial or substitutional) and on the adsorption properties of the interface. These results can be used for optimizing the adhesion characteristics of interfaces, which are determined by the requirements of particular practical applications.

REFERENCES

1. R. V. Gol'dshteǐn and M. E. Sarychev, Dokl. Akad. Nauk **380**, 476 (2001) [Dokl. Phys. **46**, 708 (2001)].

2. R. V. Gol'dshteǐn and M. E. Sarychev, Dokl. Akad. Nauk **381**, 770 (2001) [Dokl. Phys. **46**, 853 (2001)].

3. B. S. Bokshteǐn, Ch. V. Kopetskiǐ, and P. S. Shvindlerman, *Thermodynamics and Kinetics of Grains Boundaries in Metals* (Metallurgiya, Moscow, 1986).

4. J. P. Hirth and J. Lothe, *Theory of Dislocations* (McGraw-Hill, New York, 1967; Atomizdat, Moscow, 1972).

5. A. P. Babichev, I. A. Babushkina, A. M. Bratkovskiǐ, *et al.*, *The Physical Quantities. Handbook* (Énergoizdat, Moscow, 1991).

Translated by V. Bukhanov

High-Elastic Properties of Networks
Based on a Block Copolymer

V. É. Zgaevskiĭ

Presented by Academician A.E. Shilov March 5, 2002

Received March 5, 2002

Presently, needs of industry and technology for polymeric materials with various physical and mechanical characteristics are satisfied to a greater extent not by the synthesis of new polymers but by the combination and modification of already known chemical compounds. New catalysts and nonstandard polymerization approaches are widely used for producing materials based on block copolymers, graft copolymers, and polymerization composites [1]. These modification methods are most efficient compared to approaches based on the conventional mechanical mixing of various polymers. The materials obtained by such methods are macroscopically homogeneous, although at the molecular level, they are also inhomogeneous (microheterogeneous). The relations often used in practice associate mechanical properties of microheterogeneous materials with structural parameters. These relations are taken from the mechanics of filled composites where the volume fractions and mechanical characteristics of components as individual macroscopic formations are the basic parameters [1]. These methods do not allow for features of the microstructure of various microheterogeneous polymeric materials and the specific character of interactions of microstructure elements. This results in the same dependences of physicomechanical properties of such materials on the above parameters. At the same time, actual microheterogeneous materials significantly differ in both parameters of the microstructure and the characteristics of interactions of its elements. Accounting for this fact allows us not only to obtain the dependence of physicomechanical properties on the molecular and microstructural parameters but to experimentally discover new effects and regularities [2].

In this paper, we apply an approach based on the scaling concept within a model representation on the microstructure to describe high-elastic properties of networks based on block copolymers. Previously, this approach was used in [2, 3] while considering high-

Institute of Chemical Physics in Chernogolovka,
Russian Academy of Sciences,
Chernogolovka, Moscow oblast, 142432 Russia

elastic and relaxation properties of a complex of colloid particles and macromolecules.

The model of a network based on a block copolymer with a polymeric chain consisting of two blocks between the neighboring nodes is shown in the figure. One block is characterized by the magnitude of the segment a_1, by the number of segments N_1, and by the projection of the distance between the ends of the segment AB onto the r_i-axis in the laboratory coordinate system. Similarly, another block is characterized by the parameters a_2, N_2, and l_i (see figure). For simplicity, we assume that all macromolecules consist of similar blocks, but vectors $\mathbf{r}$ and $\mathbf{l}$ of various macromolecules are oriented chaotically in the network, the network being macroscopically isotropic. In the case of homogeneous deformation of the network, the distance between the ends of each macromolecule of the block copolymer (distance AC in the figure) varies similarly to the entire sample (affine deformation), but the strains of various macromolecule blocks differ from each other and from the macroscopic strain of the entire sample.

We consider a structural element of the model that is a macromolecule of the block copolymer linking two neighboring network nodes A and C (see figure). We denote the projections of the segment AC onto the plane of the laboratory coordinate system as d_i. All the projections for the initially undeformed state are denoted with a superscript zero (r_i^0, l_i^0, d_i^0). From the geometric relations, the following equality holds:

$$d_i^0 = r^0 + l_i^0. \tag{1}$$

Similarly, in the strained state, we have the relation

$$d_i = r_i + l_i. \tag{2}$$

Let a constant strain gradient be defined along the network sample as $X_{i,k} = \dfrac{\partial x_i}{\partial x_k^0}$, where x_k^0 and x_i are the coordinates of an arbitrary point of the sample prior to and after the deformation, respectively. Similarly, we denote the strain gradients of a model element at the segments AB and BC as $\xi_{i,k}$ and $\eta_{i,k}$, respectively.
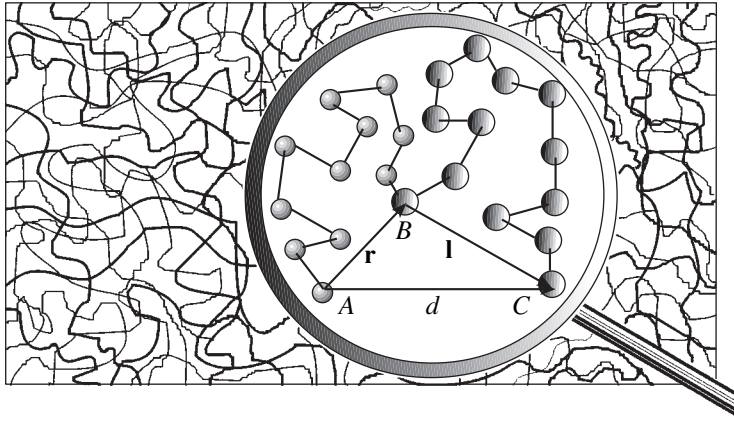
Model of the network based on the block copolymer.

From relationships (1) and (2) it follows immediately that

$$X_{i,k}d_k^0 = \xi_{i,k}r_k^0 + \eta_{i,k}l_k^0, \qquad (3)$$

where hereinafter summing over indices repeated twice is implied.

Squares of the distances AB and BC between the points can be written out in the form [4]

$$r^2 = r^{0^2} + (\xi_{l,i}\xi_{l,k} - \delta_{ik})r_i^0 r_k^0, \qquad (4)$$

$$l^2 = l^{0^2} + (\eta_{l,i}\eta_{l,k} - \delta_{ik})l_i^0 l_k^0, \qquad (5)$$

where δ_{ik} is the Kronecker delta. The free energies of the segments of polymeric chains (see figure) held by their ends at the points A, B and B, C are, respectively [5],

$$F_1 = \frac{3Tr^2}{2N_1a_1^2}, \qquad (6)$$

$$F_2 = \frac{3Tl^2}{2N_2a_2^2}, \qquad (7)$$

where T is an absolute temperature in energy units.

We write the free energy of the block-copolymer macromolecule as the sum of expressions (6) and (7):

$$F = F_1 + F_2 = \frac{3Tr^2}{2N_1a_1^2} + \frac{3Tl^2}{2N_2a_2^2}. \qquad (8)$$

Substituting relationships (4) and (5) into (8) and eliminating the gradient $\xi_{i,k}$ with the help of (3), we arrive at the expression

$$F = F^0 + \frac{3T}{2N_1a_1^2}$$

$$\times [X_{l,k}X_{l,i}d_k^0 d_i^0 - 2\eta_{l,k}l_k^0 X_{l,s}d_s^0 + \eta_{l,k}\eta_{l,i}l_k^0 l_i^0]$$

$$+ \frac{3T}{2N_2a_2^2}(\eta_{l,i}\eta_{l,k} - \delta_{ik})l_i^0 l_k^0, \qquad (9)$$

where the notation $F^0 = \dfrac{3T}{2N_1a_1^2}r^{0^2} + \dfrac{3T}{2N_2a_2^2}l^{0^2}$ is introduced.

The minimum of free energy (9) is determined by the relation $\dfrac{\partial F}{\partial \eta_{\mu,\nu}} = 0$ for a constant gradient $X_{l,k}$ set along the sample, whence it follows the equation for the determination of $\eta_{\mu,\nu}$:

$$-X_{i,s}d_s^0 + \eta_{i,\mu}l_\mu^0 + \frac{N_1a_1^2}{N_2a_2^2}\eta_{i,\nu}l_\nu^0 = 0.$$

Solving this equation yields

$$\eta_{n,i}l_i^0 = X_{n,s}d_s^0\left(1 + \frac{N_1a_1^2}{N_2a_2^2}\right)^{-1}. \qquad (10)$$

Substituting relation (10) into (9), we obtain after certain transformations

$$F = F^0 + \frac{3T}{2(N_1a_1^2 + N_2a_2^2)}X_{l,i}X_{l,k}d_i^0 d_k^0. \qquad (11)$$

Furthermore, we write out the free-energy density of the sample. In accordance with our assumption, macromolecules differ only by orientation of the vectors **r** and **l**. Therefore, we substitute equality (1) into (11) and average over the equiprobable and independent orientations of the vectors **r** and **l** using the relations [6]

$$\langle r_i^0 r_k^0 \rangle = \frac{1}{3}r^{0^2}\delta_{ik}, \quad (l_i^0 l_k^0) = \frac{1}{3}l^{0^2}\delta_{ik}, \quad (r_i^0 l_k^0) = 0. \quad (12)$$

As a result, we arrive at

$$\langle d_i^0 d_k^0 \rangle = \frac{1}{3}(r^{0^2} + l^{0^2})\delta_{ik} \qquad (13)$$

and, finally, using (13), we obtain

$$\langle F \rangle = F^0 + \frac{T(r^{0^2} + l^{0^2})}{2(N_1 a_1^2 + N_2 a_2^2)} I_1, \tag{14}$$

where $I_1 = X_{l,k} X_{l,k}$ is the first strain invariant [7]. To find the free-energy density Φ of a strained sample for network block-copolymer macromolecules, we should multiply relationship (14) by the number of macromolecules in a unit volume M of the network:

$$\Phi = \Phi_0 + \frac{MT(r^{0^2} + l^{0^2})}{2(N_1 a_1^2 + N_2 a_2^2)} I_1. \tag{15}$$

From relation (15), we can find by the conventional manner the shear modulus G^* of the indicated network:

$$G^* = \frac{MT(r^{0^2} + l^{0^2})}{N_1 a_1^2 + N_2 a_2^2}. \tag{16}$$

We now offer several modifications of expression (16) that are useful for practice. The moduli of the networks consisting of homogeneous macromolecules similar to the first and second blocks of a block-copolymer macromolecule are often known. If network macromolecules consist of only segments of the first block, the shear modulus of such a network can be expressed by the formula [in expression (16), we should put $N_2 = l^0 = 0$, and, in this case, M should be replaced by M_1]:

$$G_1 = \frac{M_1 T r^{0^2}}{2 N_1 a_1^2}. \tag{17}$$

By analogy, we obtain the expression for the shear modulus of the network consisting of homogeneous macromolecules of the second block.

$$G_2 = \frac{M_2 T l^{0^2}}{2 N_2 a_2^2}. \tag{18}$$

Combining expressions (16), (17), and (18), we arrive at the relation

$$G^* = G_1 \frac{M}{M_1} \frac{N_1 a_1^2}{N_1 a_1^2 + N_2 a_2^2} + G_2 \frac{M}{M_2} \frac{N_2 a_2^2}{N_1 a_1^2 + N_2 a_2^2}. \tag{19}$$

Here, M_1 and M_2 are the numbers of macromolecules in a unit volume of the sample consisting of homogeneous macromolecules of the first and second types, respectively.

Directly from (16), we obtain the following relation:

$$G^* = \frac{\rho R T d^{0^2}}{2 k M_c N a^2}, \tag{20}$$

where ρ is the density of a network based on a block copolymer; R is the universal gas constant; k is the Boltzmann constant (note that T is temperature expressed in energy units); d^0 is the distance between the neighboring nodes; M_c is the molecular weight of the chain between neighboring nodes of the network; N is the total number of segments of the first and second types of a block-copolymer macromolecule; and a is the effective size of the segment of the block copolymer, which can be calculated according to the formula

$$a = \left(\frac{N_1}{N_1 + N_2} a_1^2 + \frac{N_2}{N_1 + N_2} a_2^2 \right)^{\frac{1}{2}}.$$

We should pay attention to the features of the relations obtained, into which the volume fractions of the individual macromolecule blocks do not enter explicitly.

REFERENCES

1. A. D. Pomogaĭlo, A. S. Rozenberg, and I. E. Uflyand, *Metal Nanoparticles in Polymers* (Khimiya, Moscow, 2000).
2. V. É. Zgaevskiĭ, Dokl. Akad. Nauk **341**, 758 (1995) [Phys. Dokl. **40**, 179 (1995)].
3. V. É. Zgaevskiĭ, Dokl. Akad. Nauk **363**, 42 (1998) [Dokl. Phys. **43**, 685 (1998)].
4. L. D. Landau and E. M. Lifshitz, *Theory of Elasticity* (Nauka, Moscow, 1987; Pergamon, Oxford, 1986).
5. A. Yu. Grosberg and A. R. Khokhlov, *Statistical Physics of Macromolecules* (Nauka, Moscow, 1989).
6. V. N. Pokrovskiĭ, *Statistical Mechanics of Diluted Suspensions* (Nauka, Moscow, 1978).
7. V. É. Zgaevskiĭ, Kolloidn. Zh. **57**, 679 (1995).

Translated by T. Galkina

New Class of Atomic-Fractal Functions for Antenna Synthesis

V. F. Kravchenko

On the basis of ideas and results obtained in [1–6], we developed and justified a new class of fractal functions with allowance for the specific properties of atomic functions (AFs) $y_r(x)$ and $\pi_m(x)$ [2–5]. The new synthesized atomic–fractal functions (AFFs) are constructed in combinations with classic nondifferentiable functions of Weierstrass (1872), Bezikovich (1922), and van der Waerden (1930) for application to the problem of fractal-antenna synthesis.

BASIC PROPERTIES OF ATOMIC FUNCTIONS $y_r(x)$ AND $\pi_m(x)$

In order to determine the properties of the function $y_r(x)$, we consider the stages of its construction. According to [2, 5], we fix the sequence of $\overline{m}$ positive integers m_s: $m_1, m_2, m_3, \ldots$ and define the functions $\Psi_s(x)$ as

$$
\Psi_{\substack{s \\ s \geq r, \\ r = 1, 2, 3, \ldots}}(x)
$$

$$
= \begin{cases}
0, & x < -1 + \dfrac{1}{2m_r} \\[2ex]
\dfrac{k}{m_r}, & x \in \left[-1 + \dfrac{2k-1}{2m_s}, -1 + \dfrac{2k+1}{2m_s}\right] \\[2ex]
k = 1, 2, m_s - 1 \\[2ex]
1, & x \in \left[-\dfrac{1}{2m_s}, 0\right] \\[2ex]
\Psi_s(-x), & x > 0.
\end{cases}
$$

Let X_s be the independent random variables. The probability densities $\varphi_s(x)$ of random variables X_s

Institute of Radio Engineering and Electronics,
Russian Academy of Sciences,
ul. Mokhovaya 11, Moscow, 103907 Russia

$(s \geq r)$ are specified by the relationships

$$
\varphi_s(x) = \Psi_s\left(\frac{m_{r,s}x}{2m_s}\right)\frac{m_{r,s}}{2m_s} \tag{1}
$$

and, therefore, have the properties (i) $\operatorname{supp}\varphi_s(x) = [-a_s, a_s]$, where $a_s = \dfrac{2m_s - 1}{m_{r,s}}$; (ii) $\varphi_s(-x) = \varphi_s(x)$; (iii) $\varphi_s(x) > 0 \ \forall x \in (-a_s, a_s)$; and (iv) $\varphi_s(x)$ steadily increases in $[-a_s, 0]$.

According to the definition of convolution, the convolution of two densities is the density of the random variable $X_j + X_i$ with the same properties (ii)–(iv) and with the carrier equal to the sum of the carriers of the components $\operatorname{supp}\varphi_j \cdot \varphi_i = [-(a_j + a_i), (a_j + a_i)]$. Let $y_r(x)$ be the infinite-to-one convolution of densities $\varphi_s(x)$. Since the Fourier transform of the infinite-to-one convolution of densities $\varphi_s(x)$ is an infinite product of characteristic functions $\Phi_s(t)$, the Fourier transform of the function y_r has the form

$$
F_r(t) = \prod_{k=r}^{\infty} \Phi_k(t) = \prod_{k=r}^{\infty} \frac{\sin^2 \dfrac{m_k t}{m_{r,k}}}{\dfrac{m_k^2 t}{m_{r,k}^2}\sin\dfrac{t}{m_{r,k}}}, \tag{2}
$$

which is summable at the real axis and decreases faster than $|t|^{-n}$ for arbitrary $n > 0$ in the limit $|t| \longrightarrow \infty$. Therefore, $y_r \in C^{\infty}[-1, 1]$. Using the inversion theorem for the Fourier integral [5], we obtain the following integral representation of the functions:

$$
y_r(x, \overline{m}) = \frac{1}{2\pi}\int_{-\infty}^{\infty} e^{-ixt}F_r(t)\,dt, \quad r = 1, 2, 3, \ldots, \tag{3}
$$

where $F_r(t)$ is given by Eq. (2). In this case, the function $y_r(x)$ has the following properties: (i) $\operatorname{supp}y_r(x) = [-1, 1]$; (ii) $y_r(-x) = y_r(x)$; (iii) $y_r(x) \in C^{\infty}[-1, 1]$;

(iv) $\int\limits_{-\infty}^{\infty} y_r(x)dx = 1$; (v) they satisfy the infinite set of functional differential equations

$$y_r'(x) = 2\sum_{k=1}^{2m_r}(-1)^{\frac{k-1}{m_r}}y_{r+1}(x_{k,r}), \quad r = 1, 2, 3, \ldots, \quad (4)$$

where $x_{k,r} = 2m_r x + 2m_r - 2k + 1$, $x \in R^1$, $k = 1, 2, \ldots, 2m_r$; (vi) $y_r(x)$ steadily increases in $[-1, 0]$ and steadily decreases in $[0, 1]$; (vii) $N_n(y_r) = N_{n,r}^{\overline{m}}$, $n = 0, 1, 2, \ldots$, where

$$N_{n,r}^{\overline{m}} = \left\{ x \in [-1, 1]: x = x_{n,s,r} = \frac{2s}{m_{r,r+n-1}} \right\},$$

$$\left\{ s: -\frac{1}{2}m_{r,r+n-1}, \ldots, \frac{1}{2}m_{r,r+n-1} \right\}, \quad n \geq 1,$$

$$N_{0,r}^{\overline{m}} = \{ x \in [-1, 1]: x_0 = x_{0,s,r} = \pm 1 \},$$

$$\{ s: -1, 0, +1 \}, \quad n = 0;$$

(viii) $\Delta_{h_{n,r}}^2 y_r^{(n)}(x) = 0 \; \forall x \in D_{n,r}^{\overline{m}}$, $n \geq 0$, where $D_{n,r}^{\overline{m}}$ is the set of points of the interval $[-1, 1]$; (ix) $y_r(0) = 1$; (x) $\left\| y_r^{(n)}(x) \right\|_{C[-1,1]} = B_{n,r}$, $n \geq 0$, where $B_{n,r} = 2^{\frac{n(n+1)}{2}} \prod_{i=r}^{r+n-1} m_i^{r+n-1-i}$; (xi) the integer shifts of functions $y_r(x)$ give the decomposition of unity $\sum_{k=-\infty}^{\infty} y_r(x+k) \equiv 1$; and (xii) the functions $y_r(x)$ are nonanalytic at any point of the carrier.

ATOMIC FUNCTIONS $\pi_m(x)$

Let us consider the functional differential equation

$$\pi_m'(x) = a$$

$$\times \left[\pi_m(x_1(m)) + \sum_{k=2}^{2m-1}(-1)^k \pi_m(x_k(m)) - \pi_m(x_{2m}(m)) \right], \quad (5)$$

$$m = 3, 4, 5, \ldots,$$

where $x_k(m) = 2mx + 2m - 2k + 1$, $x \in R^1$, $k = 1, 2, \ldots, 2m$. We apply the Fourier transform to both sides of Eq. (5):

$$\int\limits_{-\infty}^{\infty} e^{ixt}\pi_m'(x)dx = a\left[\int\limits_{-\infty}^{\infty} e^{ixt}\pi_m(x_1(m))dx \right.$$

$$+ \sum_{k=2}^{2m-1}(-1)^k \int\limits_{-\infty}^{\infty} e^{ixt}\pi_m(x_k(m))dx$$

$$\left. - \int\limits_{-\infty}^{\infty} e^{ixt}\pi_m(x_{2m}(m))dx \right].$$

Using its fundamental properties, we obtain

$$-it\int\limits_{-\infty}^{\infty} e^{ixt}\pi_m(x)dx = \frac{a}{2m}\left[\int\limits_{-\infty}^{\infty} e^{it\frac{u+1-2m}{2m}}\pi_m(u)du \right.$$

$$+ \sum_{k=2}^{2m-1}(-1)^k \int\limits_{-\infty}^{\infty} e^{it\frac{u+2k-1-2m}{2m}}\pi_m(u)du$$

$$\left. - \int\limits_{-\infty}^{\infty} e^{it\frac{u-1+2m}{2m}}\pi_m(u)du \right].$$

Denoting the integral $\int\limits_{-\infty}^{\infty} e^{ixt}\pi_m(x)dx$ by $F_m(t)$, we represent the last equality as

$$-itF_m(t) = \frac{a}{2m}$$

$$\times \left[e^{-it\frac{2m-1}{2m}} + \sum_{k=2}^{2m-1}(-1)^k e^{it\frac{2k-1-2m}{2m}} - e^{it\frac{2m-1}{2m}} \right]F_m\left(\frac{t}{2m}\right).$$

According to the Euler formula,

$$F_m(t) = \frac{a}{tm}$$
$$\times \left[\sin\frac{2m-1}{2m}t + \sum_{k=2}^{2m-1}(-1)^k \sin\frac{2m-2k+1}{2m}t \right]F_m\left(\frac{t}{2m}\right). \quad (6)$$

Passing to integrals in Eq. (5) for $t \longrightarrow 0$ and taking into account that the integral of the function $\pi_m(x)$ is equal to 1, we obtain $a = \frac{2m^2}{3m-2}$. Substituting this value into Eq. (6), we derive

$$F_m(t) = \frac{1}{\frac{(3m-2)t}{(2m)^2}}\left[\sin\frac{(2m-1)t}{(2m)^2} \right.$$

$$\left. + \sum_{k=2}^{m}(-1)^k \sin\frac{(2m-2k+1)t}{(2m)^2} \right]F_m\left(\frac{t}{(2m)^2}\right).$$

Acting as above, we obtain

$$F_m(t) = \prod_{k=1}^{m} \frac{\sin\dfrac{(2m-1)t}{(2m)^k} + \sum_{v=2}^{m} (-1)^v \sin\dfrac{(2m-2v+1)t}{(2m)^k}}{\dfrac{(3m-2)t}{(2m)^k}}. \qquad (7)$$

The function $\pi_m(x)$ is an infinitely differentiable function with the carrier $[-1, 1]$, because it is the infinite-to-one convolution of the functions

$$\varphi_s(x) = \begin{cases} \dfrac{m}{3m-2}, & x \in \left[-1 + \dfrac{2k-1}{2m}, -1 + \dfrac{2k+1}{2m}\right], & \text{if } k \text{ is odd} \\[4mm] \dfrac{2m}{3m-2}, & x \in \left[-1 + \dfrac{2k-1}{2m}, -1 + \dfrac{2k+1}{2m}\right], & \text{if } k \text{ is even,} \end{cases}$$

$$k = 1, 2, \ldots, 2m, \quad \varphi_s(x) = 2n\varphi_{s-1}(2mx), \quad s = 2, 3, 4, \ldots$$

Applying the theorem of the Fourier-integral inversion [3, 5] to the characteristic function $F_m(t)$, we obtain the integral representation of the function $F_m(t)$

$$\pi_m(x) = \frac{1}{2\pi} \int_{-\infty}^{\infty} e^{ixt} F_m(t)dt, \qquad (8)$$

where $F_m(t)$ is given by Eq. (7). The function $\pi_m(x)$ has the following properties: (i) $\mathrm{supp}\,\pi_m(x) = [-1, 1]$; (ii) $\pi_m(-x) = \pi_m(x)$; (iii) $\pi_m(x) \in C^\infty[-1, 1]$;

(iv) $\displaystyle\int_{-\infty}^{\infty} \pi_m(x)dx = 1$;

(v) $\quad \pi_m(0) = \begin{cases} \dfrac{m}{3m-2}, & \text{if } m \text{ is odd} \\[4mm] \dfrac{2m}{3m-2}, & \text{if } m \text{ is even;} \end{cases}$

(vi) $N_v(\pi_m) = N_v, v \geq 0$, where the set N_v^m has the form

$$N_v^m = \left\{x \in [-1, 1]: x = x_{n,s} = \frac{2s}{(2m)^n}\right\},$$

$$\left\{s: -\frac{1}{2}(2m)^n, \ldots, \frac{1}{2}(2m)^n\right\}, \quad n \geq 1,$$ $\qquad (9)$

$$N_0^m = \{x \in [-1, 1]: x = x_{0,s} = s = \pm 1\},$$

$$\{s: -1, 0, 1\}, \quad n = 0;$$

(vii) $\Delta_{h_v^2}^2 \pi_m^{(v)}(x) = 0 \;\forall x \in D_v^m, v \geq 0$, where D_v^m is the set of points of the interval $[-1, 1]$; (viii) $\Delta_{h_v^1}^1 \pi_m^{(v)}(x) = 0 \;\forall x \in T_v^m, v \geq 0$; (ix) $\left\|\pi_m^{(v)}(x)\right\|_{C[-1, 1]} = K_{v,m}, v \geq 0$;

and (x) the functions $\pi_m(x)$ are nonanalytic at any point of the carrier.

FRACTAL PROPERTIES OF THE ATOMIC FUNCTIONS $y_r(x)$ AND $\pi_m(x)$

Let us construct a new class of fractal functions using certain AF properties presented in the table. Following [2, 7], we apply the fundamental mathematical operations of the multiplication of the generalized function $y_r(x)$, $\pi_m(x)$ by another function (e.g., the fractal functions of Weierstrass, Cantor, Bezikovich, and van der Waerden). On the basis of statements 1 and 2 from [2], we construct the new class of functions based on the products of the AFFs $y_r(x)$, $\pi_m(x)$ by the classical fractal functions.
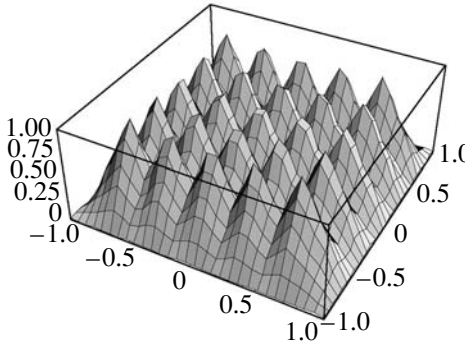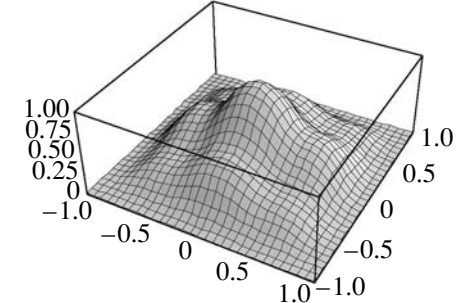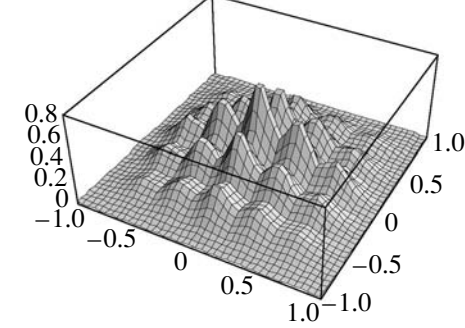
SYNTHESIS OF THE ATOMIC-FRACTAL DIRECTIONAL PATTERNS

In contrast to conventional methods [3] when the smooth antenna directional patterns (DPs) are synthesized, fractal-synthesis theory [6] is based on the idea of realizing the radiation characteristics with repeating structure at arbitrary scales. Such an approach makes it possible to create new modes of operation in the fractal antenna synthesis problems. The family of fractal functions known as the generalized Weierstrass functions [2, 4, 6] plays the determining role in the synthesis of the fractal characteristics of radiation. These functions are continuous, nowhere differentiable, and fractal functions at all scales. This class of functions can be represented in the form

$$f(x) = \sum_{n=1}^{\infty} \eta^{(D-2)n} g(\eta^n x), \qquad (10)$$

where $1 < D < 2$, g is a bounded periodic function, and $\eta > 1$. As follows from [2, 6], the factor for a nonuni-

Family of the new class of the Kravchenko atomic–fractal functions

Kravchenko fractal function	Analytical expression	Plot
$f_1(x, y) = \pi_m(x, y)$	$$\pi_m(x) = \frac{1}{2\pi}\int_{-\infty}^{\infty}\exp(jux)\prod_{k=1}^{m}\frac{\sin\left(\frac{(2m-1)u}{(2m)^k}\right)+\sum_{v=2}^{m}(-1)^v\sin\left(\frac{(2m-2v+1)u}{(2m)^k}\right)}{\frac{(3m-2)u}{(2m)^k}}du,$$ $$\pi_m(y) = \frac{1}{2\pi}\int_{-\infty}^{\infty}\exp(juy)\prod_{k=1}^{m}\frac{\sin\left(\frac{(2m-1)u}{(2m)^k}\right)+\sum_{v=2}^{m}(-1)^v\sin\left(\frac{(2m-2v+1)u}{(2m)^k}\right)}{(3m-2)u/(2m)^k}du,$$ $$f_1(x, y) = \pi_m(x)\pi_m(y), \quad m = 1, 2, \dots, \infty$$	$f_1(x, y) = \pi_6(x, y)$
$f_2(x, y) = y_r(x, y)$	$$y_r(x) = \frac{1}{2\pi}\int_{-\infty}^{\infty}\exp(jux)\prod_{i=1}^{\infty}\frac{\mathrm{shc}(r\cdot 2^{-1}+iu\cdot 2^{-n})}{\mathrm{shc}\left(\frac{r}{2}\right)}du,$$ $$y_r(y) = \frac{1}{2\pi}\int_{-\infty}^{\infty}\exp(juy)\prod_{i=1}^{\infty}\frac{\mathrm{shc}(r\cdot 2^{-1}+iu\cdot 2^{-n})}{\mathrm{shc}\left(\frac{r}{2}\right)}du,$$ $$f_2(x, y) = y_r(x)y_r(y), \quad r = 1, 2, \dots, \infty$$	$f_2(x, y) = y_6(x, y)$
$f_3(x, y) = y_r(x, y) \cdot \pi_m(x,y)$	$$f_3(x, y) = y_r(x) \cdot y_r(y) \cdot \pi_m(x) \cdot \pi_m(y),$$ $$r = 1, 2, \dots, \infty, \quad m = 1, 2, \dots, \infty$$	$f_3(x, y) = y_8(x, y) \cdot \pi_6(x, y)$

form, symmetrically distributed array of $2N$ radiating elements has the form

$$f(\theta) = 2 \sum_{n=1}^{N} I_n \cos(kd_n \cos\theta + \alpha_n). \qquad (11)$$

Here, $k = \dfrac{2\pi}{\lambda}$; I_n and α_n are the amplitude and phase of the feed current, respectively; and d_n is the spacing between the neighboring radiating elements. The array factor with an infinite number of radiating elements is assumed to be expressed in terms of the generalized Weierstrass function (10) with the cosine function g and random phase α_n:

$$f(u) = 2 \sum_{n=1}^{\infty} \eta^{(D-2)n} \cos(a\eta^n u + \alpha_n), \qquad (12)$$

where a is a constant. Comparing Eqs. (11) and (12), we find that the current amplitude and arrangement of the elements satisfy the conditions

$$I_n = \eta^{(D-2)n}, \quad kd_n = a\eta^n, \qquad (13)$$

where $u = \cos\theta$. The fractal DP defined by Eq. (12) is self-similar in the infinite range of scales. In practice, the physically realized arrays involve a finite number of elements:

$$f_N(u) = 2 \sum_{n=1}^{N} \eta^{(D-2)n} \cos(a\eta^n u + \alpha_n). \qquad (14)$$

In this case, partial sum (14) is the range-bounded Weierstrass function, while the resulting DP becomes a fractal in the finite range of scales with the lower boundary $\dfrac{2\pi}{a\eta^N}$. The scale range is controlled by the number N of radiating array elements. The DP becomes more fine with increasing N. The maximum value of function (14) for the observation angle θ_0 is equal to

$$f_N(u_0) = 2 \sum_{n=1}^{N} \eta^{(D-2)n} \qquad (15)$$

and is determined by the choice of the feed-current phase $\alpha_n = -a\eta^n u_0$ for $u_0 = \cos\theta_0$. Series (15) is a geometric progression; therefore,

$$f_N(u_0) = 2\eta^{D-2} \frac{1 - \eta^{(D-2)N}}{1 - \eta^{(D-2)}}, \qquad (16)$$

and the normalized factor of the Weierstrass array can be obtained by dividing Eq. (14) by Eq. (16) and is equal to

$$g_N(u) = \frac{1 - \eta^{D-2}}{1 - \eta^{(D-2)N}} \sum_{n=1}^{N} i_n \cos(a\eta^n u + \alpha_n), \qquad (17)$$

where the normalized feed-current amplitude is

$$i_n = \eta^{(D-2)(n-1)}. \qquad (18)$$

Comparing Eqs. (13) and (18), we find that the DP fractal dimension can be controlled by the current distribution over the array. The spacing between its arbitrary two neighboring radiating elements can be estimated by the relationship

$$d_{n+1} - d_n = \frac{a(\eta-1)\eta^n}{2\pi}\lambda, \quad n = 1, 2, \ldots, N-1. \qquad (19)$$

Following [2, 6], we consider a long linear radiating system L with a continuous variation of the current $I(z)$. For a linear infinite source, the radiation characteristic $F(u)$ and current-distribution characteristic $I(z)$ are related by a pair of Fourier transforms

$$F(u) \int_{-\infty}^{\infty} I(s)\exp(i \cdot 2\pi us)ds,$$

$$I(s) = \int_{-\infty}^{\infty} F(u)\exp(-i \cdot 2\pi Su)du, \qquad (20)$$

where $s = \dfrac{z}{\lambda}$. Any fractal function is constructed using recursive algorithms with the suitable generating function. We assume that the DP of a linear infinite source can be represented in terms of the range-bounded generalized Weierstrass function in the form

$$F(u) = \sum_{n=0}^{N-1} \eta^{(D-2)n} g(\eta^n u) \qquad (21)$$

with the generating function $g(u)$. We take $g(u)$ to be periodic and even: $g(u+2) = g(u)$, $g(-u) = g(u)$. Derived for the first time, the family of generating functions has the following form: (i) $g_1(u) = \pi_m(u)$ and $g_2(u) = y_r(u)$ are the Kravchenko AFFs; (ii) $g_3(u) = y_5(u)W(u)$ is the Kravchenko–Weierstrass function [the product of the AF $y_5(u)$ by the Weierstrass function $W(u)$]; (iii) $g_4(u) = \pi_6(u) \cdot C(u)$ is the Kravchenko–Cantor function [the product of the AF $y_5(u)$ by the Cantor function C]; (iv) $g_5(u) = \pi_{12}(u) \cdot B(u)$ is the Kravchenko–Bezikovich function [the product of the AF $y_5(u)$ by the Bezikovich function B]; and (v) $g_6(u) = y_5(u) \cdot V(u)$ is the Kravchenko-van der Waerden function [the product of the AF $y_5(u)$ by the van der Waerden function V]. Any synthesized functions (i)–(v) can be expanded into a series of the form

$$g(u) = \frac{a_0}{2} + \sum_{m=1}^{\infty} a_m \cos(m\pi u), \qquad (22)$$

where the Fourier coefficients are

$$a_m = 2\int_0^1 g(u)\cos(m\pi u)du.$$

For example, the coefficients a_m of the AFFs $\pi_m(x)$ and $y_r(x)$ can be obtained directly from Eqs. (2) and (7). In this case, substituting Eq. (22) into Eq. (21), we obtain the DP in the form

$$F(u) = \frac{a_0}{2}\frac{\eta^{(D-2)N}-1}{\eta^{(D-2)}-1}$$
$$+ \sum_{m=1}^{\infty}\sum_{n=0}^{N-1}a_m\eta^{(D-2)n}\cos(m\pi\eta^n u). \qquad (23)$$

Substituting $u + 1$ for u in (23), we obtain

$$F(u) = \frac{a_0}{2}\frac{\eta^{(D-2)N}-1}{\eta^{(D-2)}-1}$$
$$+ \sum_{m=1}^{\infty}a_m\left\{\sum_{n=0}^{N-1}\eta^{(D-2)n}\cos(m\pi\eta^n(u+1))\right\}, \qquad (24)$$

$$a_m = 2\int_0^1 g(u-1)\cos(m\pi u)du, \qquad (25)$$

where $\eta > 1$ and $1 < D < 2$. Expression (24) is the Fourier expansion of the fractal DP $F(u)$ in the AFF basis in combinations with the range-bounded cosine Weierstrass function. The feed-current distribution for a linear source required for obtaining the given DP can be obtained from (21) and written in the form

$$I(s) = \int_{-1}^{1}F(u)\exp(-i\cdot 2\pi su)du, \qquad (26)$$

where $F(u)$ for the AFF can be found from Eq. (24). In this case, the desired current distribution for the infinite linear source is expressed as

$$I(s) = a_0\frac{\eta^{(D-2)N}-1}{\eta^{(D-2)}-1}\text{sinc}(2\pi s)$$
$$+ \sum_{m=1}^{\infty}\sum_{n=0}^{N-1}a_m\eta^{(D-2)n}\{\exp(im\pi\eta^n) \qquad (27)$$
$$\times \text{sinc}(2\pi s - m\pi\eta^n)$$
$$+ \exp(-im\pi\eta^n)\text{sinc}(2\pi s + m\pi\eta^n)\}$$

for a finite source

$$\tilde{I}(s) = I(s), \quad |s|\le\frac{L}{2\lambda}, \quad \tilde{I}(s) = 0, \quad |s|>\frac{L}{2\lambda}. \qquad (28)$$

The corresponding expression for the DPs synthesized with AFFs for a linear radiating system L is determined by Eqs. (20), (28), and [2, 4, 6]:

$$\tilde{F}_{\text{AFF}}(u) = \frac{a_0}{2\pi}\frac{\eta^{(D-2)N}-1}{\eta^{(D-2)}-1}$$

$$\times\left\{\text{Si}\left[\pi\frac{L}{\lambda}(1+u)\right] + \text{Si}\left[\pi\frac{L}{\lambda}(1-u)\right]\right\}$$

$$+ \frac{1}{2\pi}\sum_{m=1}^{\infty}\sum_{n=0}^{N-1}a_m\eta^{(D-2)n}\{\cos[m\pi\eta^n(u+1)]S_{mn}(u)$$

$$+ \sin[m\pi\eta^n(u+1)]C_{mn}(u)\}. \qquad (29)$$

NUMERICAL EXPERIMENT

In order to illustrate the procedure of synthesizing a linear source of radiation, we consider a number of examples with the generalized generating function. Using the properties of the AFF of generating functions (i)–(v), we present in Fig. 1 the examples of normalized directional patterns $F(u)$ for linear sources with the given values of D, η, p, and N. The directivity of the atomic–fractal array involving the Kravchenko–Weierstrass functions $g_3(u)$, Kravchenko–van der Waerden functions $g_6(u)$, and Kravchenko–Bezikovich functions $g_5(u)$ are defined by Eqs. (20) and (21):

$$G_{\text{AFF}}(u_0) = \frac{2f_N^2(u_0)}{\int_{-1}^{1}f_N^2(u)du}, \qquad (30)$$

where $f_{N\,\text{AFF}}(u)$ is determined from Eq. (24), where a_m are the coefficients of the expansions of AFFs in terms of the Weierstrass range-bounded cosine functions (Fig. 1). It is seen that as D increases, the DP main lobe is narrowed, and the corresponding value of $G_{\text{AFF}}(u_0)$ increases. Figure 1b shows the directivity for the Kravchenko-van der Waerden generating function for various values of the self-similarity coefficient p (van der Waerden function) [2]. The coefficient p specifies the maximum range of its scaling. For example, we have a triangular function for $p = 0$, whereas the maximum scale of the van der Waerden function is equal to $4^3 = 64$ for $p = 3$. In this case, the function is broadened, which reduces the directivity. It is of interest that the directivity index increases with the fractality degree N to 21 dB (Kravchenko–Weierstrass function).

Figure 1c testifies to the interesting physical properties of the new Kravchenko–Bezikovich function: energy is uniformly redistributed from the DP main lobe over sidelobes as D increases; correspondingly, the directivity index varies from 10 to –21 dB.
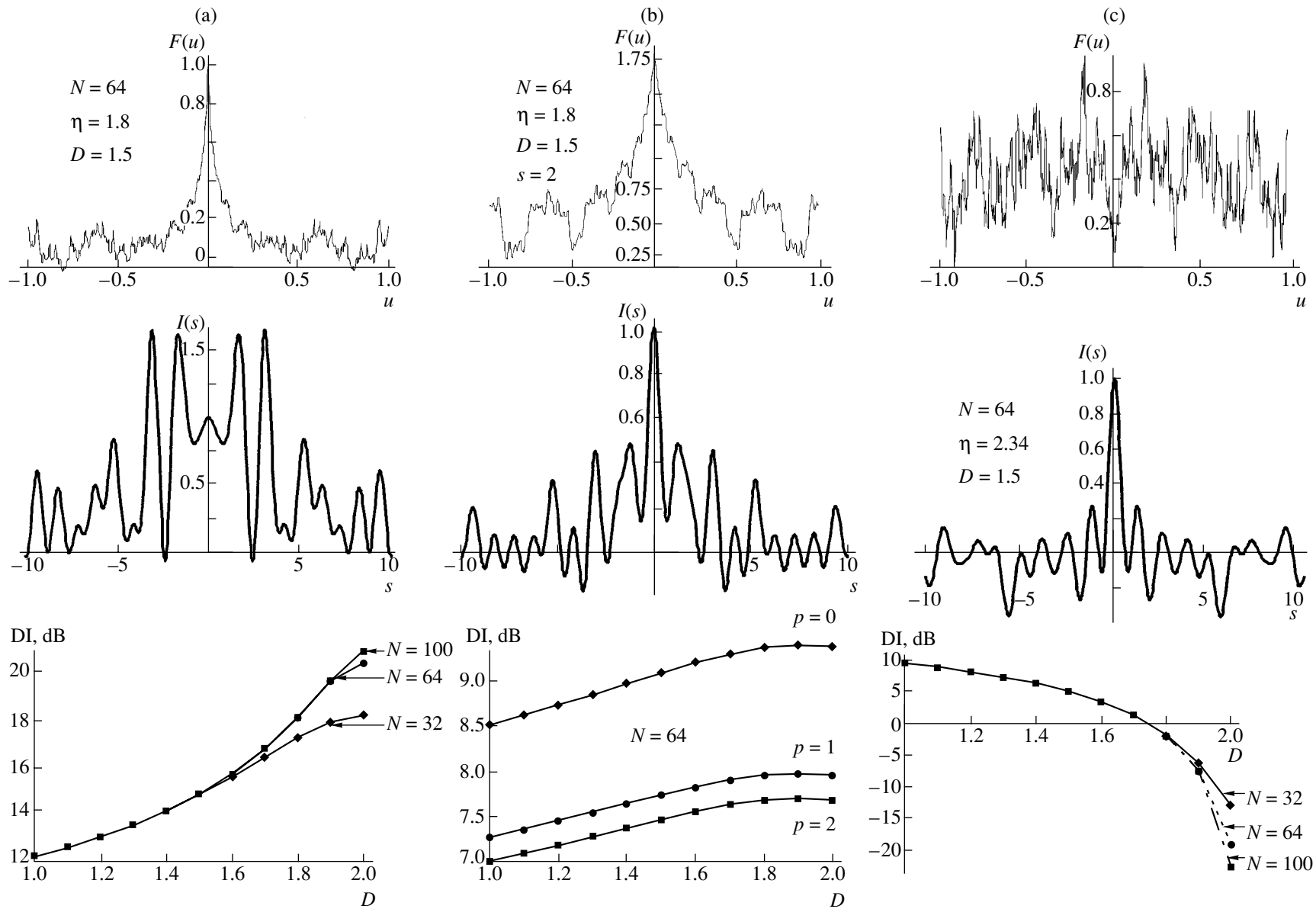
Fig. 1. Directional pattern, current distribution, and directivity index (DI) as a function of fractal dimension D for $\eta > 1$ and self-similarity coefficients $p = 0, 1, 2, \ldots$ for the (a) Kravchenko–Weierstrass, (b) Kravchenko–van der Waerden, and (c) Kravchenko–Bezikovich generating functions.

The investigation showed the efficiency of the new procedure for synthesizing self-similar fractal radiating elements. For the same physical parameters, they correspond to the known data [6] and, in certain cases, even exceed them. Thus, the same as for the cases with conventional fractal radiating elements, the proposed and justified method of constructing self-similar AFFs can yield a relatively high level of sidelobes. However, this method is robust to errors in the arrangement of elements and to their failures. This fact makes it possible practically to unify advantages of equi-amplitude and random antenna arrays.

The results of this study were reported at the URSI International Symposium on Electromagnetic Theory (Victoria, Canada, May 13–17, 2001) [8] and Fourth International Kharkov Symposium on Physics and Engineering of Millimeter and Submillimeter Waves (Kharkov, Ukraine, June 4–9, 2001) [9, 10].

ACKNOWLEDGMENTS

REFERENCES

1. V. F. Kravchenko, Dokl. Akad. Nauk **382** (2), 190 (2002) [Dokl. Phys. **47**, 51 (2002)].
2. V. F. Kravchenko, A. A. Potapov, and V. M. Masyuk, Usp. Sovrem. Radioélektron., No. 6, 4 (2001).
3. E. G. Zelkin and V. F. Kravchenko, Radiotekh. Élektron. **46** (8), 903 (2001).
4. M. A. Basarab, V. F. Kravchenko, and V. M. Masyuk, Usp. Sovrem. Radioélektron., No. 8, 5 (2001).
5. V. L. Rvachev and V. A. Rvachev, *Nonclassical Methods of Approximation Theory in Boundary Value Problems* (Naukova Dumka, Kiev, 1979).
6. D. H. Werner, P. L. Werner, and R. L. Haupt, IEEE Antennas Propag. Mag. **41** (5), 37 (1999).
7. S. L. Sobolev, *Selected Problems of the Theory of Functional Spaces and Generalized Functions* (Nauka, Moscow, 1989).
8. V. F. Kravchenko and A. A. Potapov, in *Proceedings of URSI International Symposium on Electromagnetic Theory, Victoria, 2001*, pp. 660–662.
9. V. F. Kravchenko and A. A. Potapov, in *Proceedings of the IV International Symposium on Physics and Engineering of Millimeter and Submillimeter Waves, Kharkov, 2001*, p. 102.
10. V. F. Kravchenko, in *Proceedings of the IEEE Antennas and Propagation Society International Symposium, San Antonio, 2002*, Vol. 2, p. 148.

Translated by V. Bukhanov

================== **ENERGETICS** ==================

Excitation of Acoustic Vibrations by Heating a Liquid in a Supercritical State

V. R. Pesochin

Presented by Academician V.E. Fortov April 21, 2002

As is known [1], high-frequency acoustic vibrations can arise in heated ducts with a supercritical liquid. These vibrations cause pulsations of the flow rate of the liquid, cyclic stresses in the device structure, and even the destruction of the latter. For example, experiments [2] showed that pressure oscillations with a frequency up to $10000 \, s^{-1}$ and amplitude up to 27 atm arise in supercritical liquid hydrocarbons in a turbulent flow regime as they are heated in a duct (with a liquid-propellant-engine cooling system) at a steady-state pressure of ~35 atm. These oscillations were responsible for the formation of cracks and flaws in the experimental duct. Therefore, the excitation of acoustic vibrations by heating a supercritical liquid flowing in a duct is a problem of current interest.

There is extensive experimental information concerning the origination of thermal acoustic vibrations of a supercritical heat-transfer liquid [3–6]. The phenomenon was explained in [1, 7] as follows. When heat is supplied from walls, the field of the turbulent flow of a supercritical liquid can be divided into the turbulent core and viscous sublayer near the walls. The viscous sublayer is characterized by a steep temperature profile, while the profile in the turbulent core is much smoother because of turbulent mixing. In addition, the viscous liquid sublayer is more compressible than the flow core. Therefore, the viscous sublayer provides the phase relations between variations of pressure and heat flux (feedback) that are necessary for the excitation of acoustic vibrations. This mechanism was used in [7] to numerically investigate the excitation of acoustic vibrations in a heated supercritical liquid.

In this paper, the excitation of longitudinal acoustic vibrations by heating a supercritical liquid flowing in a duct of length l and radius r_0 is investigated theoretically. It is assumed that heat supply to the flowing liquid is distributed along the duct length, whereas the

Institute for High Energy Densities,
Joint Institute for High Temperatures,
Russian Academy of Sciences,
ul. Izhorskaya 13/19, Moscow, 127412 Russia

heat-flux density q for the steady-state process is constant. Similar to [1, 7], quasi-static relations are used to describe heat exchange between the liquid vibrating with acoustic frequency and the duct walls. In addition, as is accepted in acoustics [8], the supercritical liquid is considered as inviscid.

Under these assumptions, equations of continuity, motion, and energy take the form

$$\frac{\partial \rho}{\partial t} + \frac{\partial}{\partial x}(\rho u) = 0, \tag{1}$$

$$\frac{\partial u}{\partial t} + u\frac{\partial u}{\partial x} = -\frac{1}{\rho}\frac{\partial p}{\partial x}, \tag{2}$$

$$\rho\left(\frac{\partial i}{\partial t} + u\frac{\partial i}{\partial x}\right) = \frac{1}{r}\frac{\partial}{\partial r}(qr) + \frac{\partial p}{\partial t}, \tag{3}$$

where i is the specific enthalpy of the liquid. The other notation is conventional. The liquid density is treated as a function of thermodynamic parameters; i.e.,

$$\rho = \rho(p, s). \tag{4}$$

The linearization of Eqs. (1)–(3) yields the following approximate equations:

$$\frac{\partial \rho'}{\partial t} + \rho\frac{\partial u'}{\partial x} + u'\frac{\partial \rho}{\partial x} = 0, \tag{5}$$

$$\frac{\partial u'}{\partial t} = -\frac{1}{\rho}\frac{\partial p'}{\partial x}, \tag{6}$$

$$\rho\left(\frac{\partial i'}{\partial t} + u'\frac{\partial i}{\partial x}\right) = \frac{1}{r}\frac{\partial}{\partial r}(q'r) + \frac{\partial p'}{\partial t}. \tag{7}$$

Hereafter, perturbation is marked by a prime.

Approximate equations (5)–(7) can be used for investigating the excitation of acoustic vibrations in a flowing supercritical liquid at $\text{Sh} \gg 1$, where $\text{Sh} = \dfrac{\omega l}{u}$ is the Strouhal number for acoustic vibrations and ω is the cyclic frequency. To linearize Eq. (4), one should have the density of a supercritical liquid ρ as a function

of the enthalpy i at constant pressure. Here, we use the empirical dependence

$$\rho = [\rho_0^{-1} + b(i - i_0)]^{-1}, \quad b = \text{const},$$

proposed in [9] for helium, where ρ_0 and i_0 are the density and enthalpy of the supercritical liquid at the duct entrance.

With insignificant error, this dependence can be used as well for other supercritical liquids. For example, for supercritical water vapor, it is accurate to not worse than ~20%. In view of the last expression, the linearization of (4) yields

$$\frac{\rho'}{\rho} = \frac{p'}{\rho c_s^2} - b\rho i', \qquad (8)$$

where c_s is the adiabatic speed of sound.

Substituting Eq. (8) into Eq. (5) and taking into account both Eq. (7) and the equality

$$\left(\frac{1}{\rho c_s^2} - b\right)\frac{\partial p'}{\partial t} = \frac{b}{r}\frac{\partial}{\partial r}(q'r) - \frac{\partial u'}{\partial x}, \qquad (9)$$

we obtain the equation

$$b\rho\frac{\partial i}{\partial x} = -\frac{1}{\rho}\frac{\partial \rho}{\partial x}.$$

Differentiating Eqs. (6) and (9) with respect to x and t, respectively, and eliminating u', we derive the equation

$$\left(\frac{1}{\rho c_s^2} - b\right)\frac{\partial^2 p}{\partial t^2} = \frac{1}{\rho}\frac{\partial^2 p}{\partial x^2} + \frac{b}{r}\frac{\partial}{\partial r}\left(r\frac{\partial q'}{\partial t}\right). \qquad (10)$$

To be solved, this equation requires an expression for q', which, in general, depends on heat transfer in both the liquid and the duct wall. As is known [7], the quantity q' is primarily determined by the variation of viscous-sublayer thickness under acoustic vibrations. Therefore, using the condition of mass conservation in the viscous sublayer, one can derive the relation

$$\frac{q'}{q} = \frac{\rho'}{\rho} = \frac{1}{\gamma}\frac{p'}{p}; \qquad (11)$$

where γ is the specific-heat ratio.

The last formula is derived with allowance for the fact that, at high-frequency vibrations in a duct, a state of the liquid can be described in the quasi-adiabatic approximation [8]. For a steady-state flow of the supercritical liquid, enthalpy is distributed linearly along the duct [10]:

$$i = i_0 + \frac{2q_1 x}{\rho u r_0},$$

where q_1 is the heat-flux density on the duct surface. Aver-

aged along the duct length, the last expression yields

$$\langle i \rangle = i_0 + \frac{q_1 l}{\rho_0 u_0 r_0}. \qquad (12)$$

For a turbulent flow, liquid velocity at each point of a duct cross-section is close to its average value over this section [10]. Then, the heat flux is a linear function of the radius, so that

$$\frac{q}{q_1} = \frac{r}{r_0}. \qquad (13)$$

In this case, with allowance for Eqs. (11)–(13), Eq. (10) can be written as

$$\frac{\partial^2}{\partial t^2}\left(\frac{p'}{p}\right) = \alpha^2\frac{\partial^2}{\partial x^2}\left(\frac{p'}{p}\right) + 2\delta\frac{\partial}{\partial t}\left(\frac{p'}{p}\right); \qquad (14)$$

where $\alpha^2 = \dfrac{\langle c_s^2 \rangle}{1 - \gamma b p}$ and $\delta = \dfrac{b}{1 - \gamma b p}\dfrac{q}{r_0}$.

Equation (14) should be complemented by boundary conditions corresponding to the properties of the device in whose duct the excitation of acoustic vibrations is investigated. In this paper, we consider a duct with acoustically open ends. Then, the boundary conditions have the form

$$p' = 0 \text{ at } x = 0,$$

$$p' = 0 \text{ at } x = l.$$

Solving Eq. (14) with these boundary conditions by the method of separation of variables, we obtain the expression

$$\frac{p'}{p} = e^{\delta t}\sum_{k=1}^{\infty} B_k \sin\frac{\pi k x}{l}\cos(\sqrt{\omega_k^2 - \delta^2}\, t + \varphi_k), \qquad (15)$$

where $k = 1, 2, 3\ldots$.

The quantities B_k and φ_k are determined from the initial conditions, while the natural frequency

$$\omega = \frac{\pi k \alpha}{l}$$

is found from the boundary conditions. Expression (15) shows that, at $\delta > 0$, the external heating of the supercritical liquid flowing in the duct excites acoustic vibrations with the increment

$$\mu = \frac{2\pi\delta}{\sqrt{\omega_k^2 - \delta^2}}.$$

According to Eq. (14), the excitation of acoustic vibrations ceases at the pressure $p \geq \dfrac{1}{\gamma b}$, which is usually much higher (by about five or six times) than the critical pressure. Therefore, in a supercritical liquid, the excita-

tion of acoustic vibrations is possible in the pressure range

$$p_c < p < \frac{1}{\gamma b};$$

where p_c is the critical pressure.

The termination of acoustic vibrations at $p \geq \dfrac{1}{\gamma b}$ is verified experimentally [2]. According to Eq. (15), the excitation of acoustic vibrations reduces the vibration frequency of the supercritical liquid as compared to the natural frequency. However, this decrease is insignificant. For example, $\delta = 4 \text{ s}^{-1}$ for $\omega_1 = 1.6 \times 10^3 \text{ s}^{-1}$ when water of the initial temperature $T_0 = 630 \text{ K}$ is heated in a duct, which has the dimensions $l = 1 \text{ m}$ and $r_0 = 10^{-2} \text{ m}$, under the pressure 235 atm at $b = 6 \times 10^{-9} \text{ m}^3/\text{J}$, $q_l = 2 \times 10^6 \text{ W/m}^2$, and $u_0 = 1 \text{ m/s}$.

It is of interest to compare these results with the Rayleigh criterion [8], which is known in thermal acoustics as a condition of the excitation of acoustic vibrations and is generally used for investigating the acoustic stability of a system. It provides the sufficient stability conditions and reveals sources of vibrational energy if they are not obvious, for example, during phase transitions in a vapor–gas mixture [11]. As in [8], we multiply Eqs. (6) and (9) by u' and p', respectively, and integrate the sum of the resulting expressions over volume. This procedure yields

$$\frac{\partial E'}{\partial t} = N_Q + N_S;$$

where

$$E' = \int_V \left[\frac{\rho (u')^2}{2} + \frac{(p')^2}{2\gamma p}(1 - \gamma b p) \right] dV,$$

$$N_S = -\int_S p'u' dS; \quad N_Q = 2\frac{bq_1}{\gamma p r_0} \int_V (p')^2 dV.$$

Here, the surface integral is equal to zero [8]. Therefore, the single source of vibrational energy is the pos-

itiveness of the quantity

$$N_Q = \beta \int_V \left(\frac{p'}{p}\right)^2 dV > 0, \quad \beta = 2\frac{pbq_1}{\gamma r_0}.$$

This inequality mathematically expresses the Rayleigh criterion. It shows that the heating of a supercritical liquid flowing in a duct can excite acoustic vibrations. However, in contrast to the results of this paper, the increment and frequency of these vibrations cannot be determined from the Rayleigh criterion.

Thus, the model proposed here describes the excitation of acoustic vibrations by external heating of a supercritical liquid flowing in a duct. In this model, the increment and frequency of the vibrations are simply expressed in terms of the initial parameters of the liquid and power of the heater.

REFERENCES

1. V. B. Khabenskiĭ and V. A. Gerliga, *Instability of Flow of Heat-Transfer Agent in Elements of Power Equipment* (Nauka, St. Petersburg, 1994).
2. R. Heins and G. Wolf, Raketnaya Tekhnika, No. 3, 18 (1962).
3. V. I. Vetrov, V. A. Gerliga, and V. G. Razumovskiĭ, Vopr. At. Nauki Tekh., Ser.: Fiz. Tekh. Yad. Reakt., Din. Yad. Énerg. Ustan., No. 2, 51 (1977).
4. V. A. Gerliga and V. I. Vetrov, Izv. Vyssh. Uchebn. Zaved., Aviats. Tekh., No. 1, 31 (1978).
5. N. L. Kafengauz, Inzh.-Fiz. Zh. **44** (1), 14 (1983).
6. K. Goldman, in *International Development in Heat Transfer* (Washington, DC, 1961), Part 3, p. 562.
7. M. A. Il'chenko, V. V. Kryutchenko, Yu. S. Mnatsakanyan, *et al.*, *Stability of Work Process in Engines of Aircrafts* (Mashinostroenie, Moscow, 1995).
8. K. I. Artamonov, *Thermohydroacoustic Stability* (Mashinostroenie, Moscow, 1982).
9. D. A. Labuntsov and P. A. Mirzoyan, Teploénergetika (Moscow), No. 3, 2 (1983).
10. S. S. Kutateladze, *Foundations of Heat Transfer Theory* (Nauka, Novosibirsk, 1970).
11. V. R. Pesochin, Teplofiz. Vys. Temp. **32**, 791 (1994).

Translated by Yu. Verevochkin

=== **MECHANICS** ===

Cutting and Fracture of Ideal Rigid-Plastic Solids

Yu. G. Egorova, S. A. Kaverzina, and A. I. Khromov

Presented by Academician V.P. Myasnikov September 10, 2001

The rigid-plastic analysis of the cutting problem stems from the model based on the assumption of the existence of a single shear plane (isolated slip line). In this formulation of the problem, two basic kinematically admissible solutions are known [1, 2]. In this paper, the completeness of the solutions found in [1, 2] is studied from the standpoint of constructing a statically admissible continuation of the stress field to rigid zones (i.e., to the blank body and cuttings). It is shown that known solutions have significant limitations. A new solution supposing the existence of a statically admissible continuation to rigid zones and minimizing the volume density of energy dissipation and strain in the shear plane is suggested. The problem of cutting accompanied by fracture is analyzed.

1. We consider the problem of cutting (Fig. 1). An absolutely hard cutter is assumed to be immobile: a blank moves from left to right with a constant velocity **V**. *ST* is the shear plane (isolated slip line). The material moves towards the cutter as a rigid whole, deforms in the shear plane *ST*, and, furthermore, moves as a solid body along the front surface *NT* of the cutter.

The solutions obtained in [1, 2] yield the following dependences for the determination of the shear-plane angle φ:

$$\varphi = \frac{1}{2}\left(\frac{\pi}{2} + \alpha - \lambda\right) \text{ is solution of [1],}$$

$$\varphi = \frac{\pi}{4} + \alpha - \lambda \text{ is solution of [2],}$$

where α is the front angle of the cutter and λ is the friction angle at the cutter front surface.

The completeness of the solutions of [1, 2] is studied from the standpoint of constructing a statically admissible continuation of the stress field to rigid zones. For the stress-field construction, an idea described in [3] is used: the continuation of the stress field beyond the plastic-rigid boundary is constructed on the assumption that the material, by convention, is in a plastic state and

Institute of Machine Science and Metallurgy,
Far-East Division, Russian Academy of Sciences,
Komsomolsk-na-Amure, ul. Metallurgov 1, 681005 Russia

that the stress field is determined by the system of equations

$$\frac{1}{4}(\sigma_x - \sigma_y)^2 + \tau_{xy}^2 = k^2, \quad \frac{\partial \sigma_x}{\partial x} + \frac{\partial \tau_{xy}}{\partial y} = 0,$$

$$\frac{\partial \sigma_y}{\partial y} + \frac{\partial \tau_{xy}}{\partial x} = 0.$$

Furthermore, the statically admissible continuation is constructed such that it is limited by a certain surface Σ which is free of stresses and lies completely inside the rigid zone. In [4], within the framework of this approach, local criteria of the existence of the stress field continuation in the vicinity of the rigid-plastic boundary at the point of its exit to the free surface are suggested. These criteria form grounds for studies of the completeness of the solutions.

The conditions of the existence of the continuation suggested in [4] are transformed here to the following forms.

(a) Continuation to the *MST* region (Fig. 1):

$$\cot\varphi \geq \tan(\varphi + \lambda - \alpha) \text{ (necessary condition)}, \quad (1)$$

$$\tan(\varphi + \lambda - \alpha) \leq 1 + \frac{\pi}{2} - 2\varphi \text{ (sufficient condition)}. \quad (2)$$

(b) Continuation to the *RST* region:

$$\varphi \geq \alpha - \frac{\lambda}{2} \text{ (necessary condition)}, \quad (3)$$
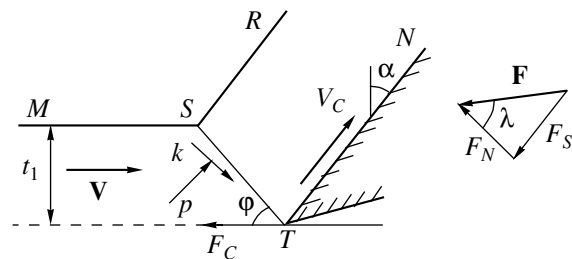

Fig. 1. Diagram of the cutting process without fracture.

$$\tan(\varphi + \lambda - \alpha) \le 1 - 2\cos\left(\frac{\pi}{4} - \alpha + \varphi\right) \qquad (4)$$

(sufficient condition).

(c) Continuation to the *NTS* region:

$$\varphi \le \frac{\pi}{4} + \alpha - \lambda \qquad (5)$$

(necessary and sufficient conditions).

Thus, for the completeness of the solution, it is necessary for the angle φ to simultaneously satisfy all inequalities (1)–(5).

Studies of the completeness of the solutions obtained in [1, 2] have shown that the solution of [1] has no stress-field continuation to rigid zones, while the solution of [2] has a continuation in the case of $\alpha \le \lambda$. Thus, the known solutions of [1, 2] have significant limitations from the standpoint of their completeness.

We suggest a new solution supposing the existence of a statically admissible continuation to rigid regions. The possibility of finding this solution is provided by the kinematic uncertainty of the cutting problem: the boundary conditions for velocities can be met at an arbitrary angle φ. Thus, there is an infinite set of kinematically possible solutions that can be complete at definite angles φ, α, and λ. To choose a preferential solution, we use the condition of the minimum of the volume density for the dissipation energy W. This energy is acquired by a particle of the material when intersecting the shear plane in the case of the continuation of the stress field to the rigid zones. In this case, the solution is complete. It is shown in [4, 6] that the quantity W relates to the angle φ by the dependence

$$W = \frac{[V_\tau]}{G - V_n}k, \quad [V_\tau] = \sin\varphi\tan(\alpha - \varphi) - \cos\varphi,$$

$$V_n = \sin\varphi.$$

Here, $[V_\tau]$, V_n are the discontinuity of the tangent component and the normal component of the particle velocity while intersecting the shear plane, respectively; G is the normal velocity of the shear-plane propagation (when cutting without fracture; $G = 0$); and k is the yield stress of the material.

The dependences $\overline{W} = \overline{W}(\varphi)$ for various angles α are shown in Fig. 2 ($\overline{W} = \dfrac{W}{k}$ and μ is the friction coefficient). The lines *1–1*, *2–2*, *3–3*, *4–4*, and *5–5* bound the regions of the validity of inequalities (1)–(5), respectively. The blackened region represents the range of values of φ in which all the inequalities (1)–(5) simultaneously hold (i.e., this is the region of existence of the complete solution).

In order to choose the preferential solution, we assume that the quantity W in the region of the existence of the complete solution has a minimum value.

The minimum value of W in this region is attained when the boundary of the constructed continuation to the *MST* region coincides with the free boundary of the material. Then, the angle φ is determined from the equation

$$\tan(\varphi + \lambda - \alpha) = 1 + \frac{\pi}{2} - 2\varphi. \qquad (6)$$

The line *2–2* corresponds to Eq. (6) (Fig. 2).

The strains in the shear plane can be found on the basis of the theory of Hadamard–Thomas discontinuity functions [5]. In particular, according to [6], the first
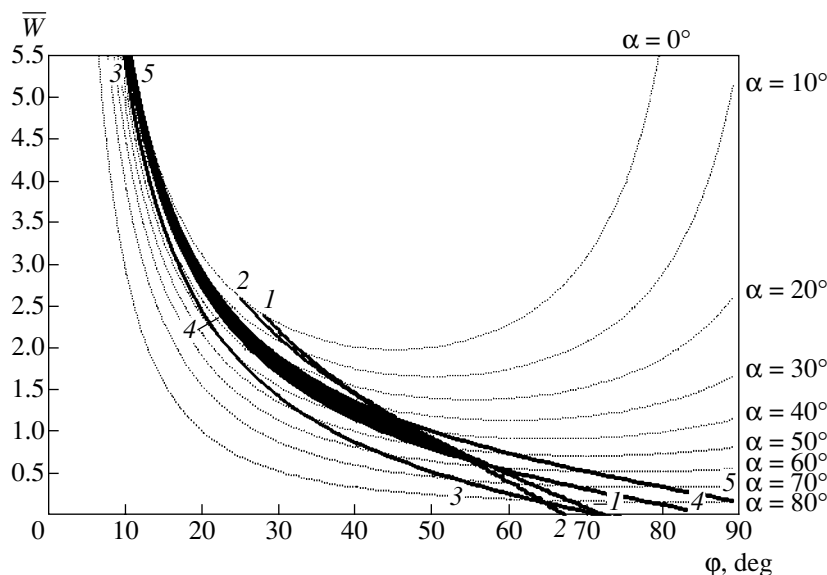

Fig. 2. The region of the existence of the complete solution to the problem of cutting without fracture ($\mu = 0.7$).
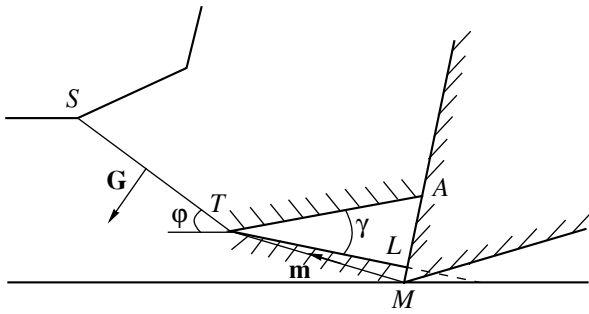
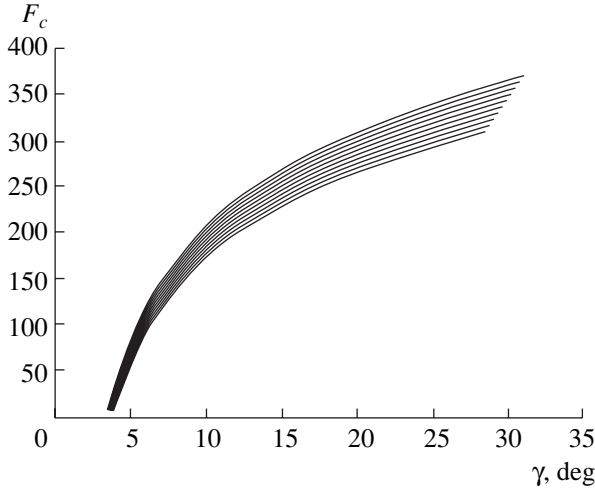**Fig. 3.** The initial moment of the crack development.

Fig. 4. Cutting force F_c as a function of the crack-opening angle γ for various angles α (upper and lower curves correspond to $\alpha = 1°$ and $10°$, respectively; $\overline{W} = 8$, $\mu = 0.35$).

principal value of the Almansi tensor beyond the shear plane is determined in terms of W by the dependence

$$E_1 = \frac{\overline{W}^2}{4(\sqrt{1 + 4/\overline{W}^4} - 1)}. \tag{7}$$

The value of E_1, as that of W, attains a minimum provided that condition (6) is true.

The cutting force is determined in terms of φ as

$$F_c = \frac{kt_1 \cos(\lambda - \alpha)}{\sin\varphi \cos(\varphi + \lambda - \alpha)},$$

where t_1 is the thickness of the layer being cut off. The values of the cutting force according to the new solution and the solution of [1] virtually coincide.

Thus, the new solution to the problem of cutting without fracturing is complete and minimizes the volume density of the energy dissipation and strain in the shear plane.

2. We now consider the solution to the problem of cutting with fracture. A general approach to the study of the problems of crack propagation in rigid-plastic solids, as well as fracture criteria for the strain and energy, are given in [6]. We assume that the fracture of a material begins if the strains E_1 [or, according to (7), the magnitude of the volume density of the energy dissipation in the shear line] attain the limiting value

$$W \geq W_*,$$

where W_* is the limiting value of W, at which the fracture begins. The direction **m** of the crack development is, generally speaking, not defined.

In the process of the nucleation and development of a crack, the shear plane comes off the cutting edge and begins its motion with a normal velocity **G**. We consider the initial moment of the crack development when crack boundaries are still rectangular (Fig. 3).

The crack develops in the direction **m**. Its vertex T is the point of intersection of the current position of the shear line and the direction of the crack development. The position of the upper boundary of the crack is defined by the point A, which moves with the velocity of cutting.

The appearance of the crack results in the formation of a new free surface in the blank material. This surface forms the lower crack boundary, which intersects the cutter at the point L and results in the formation of the secondary cuttings, whose effect is not analyzed here. The angle γ corresponds to the crack opening angle.

Possible directions of the crack development are also studied. To this end, the dependence of the plastic-strain work (unambiguously associated with the cutting force F_c) on the crack opening angle γ is analyzed. The derivative $\dfrac{dF_c}{d\gamma}$ is defined by the expression

$$\frac{dF_c}{d\gamma} = \frac{\dfrac{dF_c}{dz}}{\dfrac{d\gamma}{dz}} = -\frac{k\cos(\lambda - \alpha)\left(1 + \dfrac{a^2}{b^2}\right)\left(1 + \dfrac{z^2}{c^2}\right)}{\cos(\varphi + \lambda - \alpha)\sin\varphi \cdot f}, \tag{8}$$

$$a = \frac{\sin\varphi \cdot t\cos\alpha}{\cos(\varphi - \alpha)} - z,$$

$$b = z\cot\varphi + \frac{Gt}{\sin\varphi} + \frac{\sin\varphi \cdot t\sin\alpha}{\cos(\varphi - \alpha)},$$

$$c = z\cot\varphi + \frac{Gt}{\sin\varphi} + t,$$

$$f = -\frac{(c^2 + z^2)(b + a\cot\varphi) - (b^2 + a^2)(c - z\cot\varphi)}{b^2 c^2}.$$

Study of the sign in expression (8) has shown that, within the entire region of definition, $\dfrac{dF_c}{d\gamma} > 0$; i.e., the cutting force increases with the crack opening angle (Fig. 4).

The largest angle of crack opening is attained at the smallest angle between the direction **m** and the horizontal line. In this case, the cutting force F_c reaches the largest value.

ACKNOWLEDGMENTS

REFERENCES

1. H. Ernst and M. E. Merchant, Trans. ASME **29**, 299 (1941).

2. E. H. Lee and B. W. Shaffer, J. Appl. Mech. Trans. ASME **73**, 405 (1951).

3. J. F. W. Bishop, J. Mech. Phys. Solids **2** (1), 43 (1953).

4. A. I. Khromov, *Strain and Fracture of Rigid-Plastic Bodies* (Dal'nauka, Vladivostok, 1995).

5. T. Thomas, *Plastic Flow and Fracture in Solids* (Academic, New York, 1961; Mir, Moscow, 1964).

6. A. I. Khromov, Dokl. Akad. Nauk **362**, 202 (1998) [Dokl. Phys. **43**, 587 (1998)].

7. G. I. Bykovtsev and D. D. Ivlev, *Theory of Plasticity* (Dal'nauka, Vladivostok, 1998).

Translated by T. Galkina

=========== **MECHANICS** ===========

Peculiarities of the Bending-Stiffness Calculation for Nanocrystals

E. A. Ivanova*, A. M. Krivtsov*, and Academician **N. F. Morozov****

In view of the evolution of nanotechnology, it is of current interest to develop analytical models for describing the mechanical deformation of nanodimensional objects. The majority of available theoretical models are based on elasticity-theory equations. In this case, values of the modulus of elasticity obtained in macroscopic experiments are commonly used. At the same time, many investigators pointed to a discrepancy between values of the modulus of elasticity obtained in microscopic and macroscopic experiments (see, e.g., [1–3]). In [4], the Young's modulus and Poisson's ratio were theoretically investigated as functions of the number of atomic layers by the example of a two-dimensional single-crystal strip. It was shown that, with a decreasing number of atomic layers, the Poisson's ratio decreases and the Young's modulus increases and, for two-layer crystalline films, can differ from their macroscopic values by a factor of 1/2 and 2, respectively. The results [4] indicate that scale effects must be taken into account when notions of continuum mechanics are applied to nano-objects. In this study, we theoretically investigated the effect of the scale factor on the bending stiffness of a single-crystal strip. This problem is of high priority because, in particular, it is necessary to investigate the stress–strain state of nanotubes, which are extensively used in current engineering applications [5–8].

We consider a two-dimensional single crystal with $N \geq 2$ layers along the y axis and $J \gg N$ layers along the x axis. Each atom is assumed to interact only with the nearest neighbors (see figure). Forces Q_n are applied to the atoms on the lateral faces of the crystal. The subscript n means the layer number ($n = 1, 2, …, N$). From one layer to another, forces vary linearly, so that the summary load acting on the lateral crystal face provides only the moment of force

$$\sum_{n=1}^{N} Q_n = 0, \quad \sum_{n=1}^{N} R_n Q_n = M. \tag{1}$$

The strained state of the single crystal is completely specified by spacings a_{jn} between the neighboring atoms in each layer and by spacings b_{jn} between the nearest atoms in the neighboring layers. The subscripts j and n correspond to the numbers of layers along the x and y axes, respectively (see figure). It is evident that spacings h_{jn} between layers can be determined from the geometric relationship $h_{jn}^2 = b_{jn}^2 - \dfrac{a_{jn}^2}{4}$. In the unstrained state, the crystal lattice consists of equilateral triangles with sides $a = b = a_0$. This lattice is characterized by the relations

$$h_0 = \frac{\sqrt{3}}{2} a_0, \quad R_n = (n-1) h_0.$$

It is easy to show that the formula for Q_n satisfying
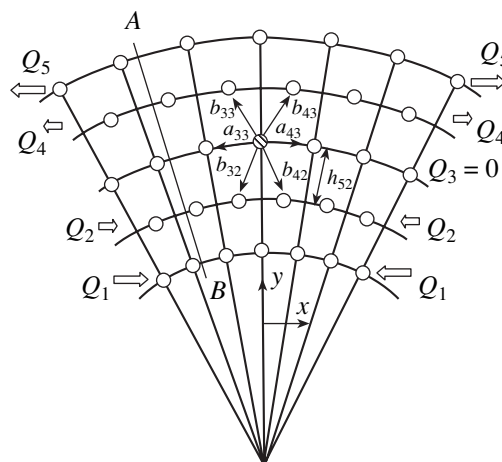
Bending of a nanocrystal strip.

* *St. Petersburg State Technical University,*
ul. Politekhnicheskaya 29, St. Petersburg,
195251 Russia
** *Faculty of Mathematics and Mechanics,*
St. Petersburg State University,
Bibliotechnaya pl. 2, Petrodvorets,
St. Petersburg, 198904 Russia

conditions (1) has the form

$$Q_n = \frac{4\sqrt{3}M(2n - N - 1)}{a_0(N-1)N(N+1)}. \tag{2}$$

Let $F(r)$ be the force of interaction between two atoms separated by distance r. Assuming the smallness of strains (displacements are magnified in the figure for clearness) induced by the forces of interaction between atoms in the crystal, we use the linear approximation

$$F(a_{jn}) = C\Delta a_{jn}, \quad F(b_{jn}) = C\Delta b_{jn},$$
$$C \stackrel{\text{def}}{=} F'(a_0) > 0, \tag{3}$$

where C is the interatomic-bond rigidity, $\Delta a_{jn} \stackrel{\text{def}}{=} a_{jn} - a_0$, and $\Delta b_{jn} \stackrel{\text{def}}{=} b_{jn} - a_0$. Such a simplified approach is justified by the fact that the modulus of elasticity in continuum mechanics is generally determined in linear theory. It should be noted that the approach proposed here can be realized even without the assumption that elastic bonds are linear; the difficulties arising in this case are of a purely technical nature. Writing the equations of equilibrium for atoms of the crystal lattice, we obtain the set of recurrence equations for the quantities Δa_{jn}, Δb_{jn}, and Q_n:

$$\Delta a_{j,n} + \frac{1}{2}(\Delta b_{j,n} + \Delta b_{j,n-1})$$
$$= \Delta a_{j-1,n} + \frac{1}{2}(\Delta b_{j-1,n} + \Delta b_{j-1,n-1}),$$

$$\Delta b_{j,n} + \Delta b_{j-1,n} = \Delta b_{j,n-1} + \Delta b_{j-1,n-1}, \tag{4}$$

$$\Delta a_{l,n} + \frac{1}{2}(\Delta b_{l,n} - \Delta b_{l-1,n} + \Delta b_{l,n-1} - \Delta b_{l-1,n-1}) = \frac{Q_n}{C},$$

$$\Delta a_{J-l,n} + \frac{1}{2}(\Delta b_{J-l,n} - \Delta b_{J-l+1,n} + \Delta b_{J-l,n-1}$$
$$- \Delta b_{J-l+1,n-1}) = \frac{Q_n}{C}, \quad l = 1, 2.$$

The solution to these equations has the form

$$\Delta b_{jn} = 0, \quad \Delta a_{jn} = \frac{Q_n}{C}. \tag{5}$$

We conceptually cut the crystal by a vertical straight line AB (see figure). According to Eqs. (2) and (5), the total normal force acting from one part of the crystal to the other is equal to zero. The total bending moment M is calculated by Eq. (1). As can be seen from Eqs. (2) and (5), a change in interatomic spacings Δa_{jn} linearly depends on the layer number n along the y axis and is independent of the layer number j along the x axis. This means that the atomic layers along the y axis remain rectilinear when the crystal is deformed, and the angles between any neighboring atomic layers in the strained state are identical. In this case, the angle α between the

neighboring atomic layers and the corresponding curvature β are determined as follows:

$$\alpha \stackrel{\text{def}}{=} \frac{\Delta a_{jN}/2 - \Delta a_{j1}/2}{h_0(N-1)}, \quad \beta \stackrel{\text{def}}{=} \frac{\alpha}{a_0/2}. \tag{6}$$

According to Eqs. (2), (5), and (6), the bending stiffness of the single-crystal strip has the form

$$D \stackrel{\text{def}}{=} \frac{M}{\beta} = \frac{Ca_0^3}{16}(N-1)N(N+1). \tag{7}$$

Attempts to express bending stiffness in terms of macroscopic parameters encounter difficulties associated with the possibility of different definitions of the thickness H of the nanocrystal. On the one hand, the single-crystal thickness can be defined as the spacing $H = (N - 1)h_0$ between atomic layers at opposite ends; on the other hand, the nanocrystal thickness can be defined as the product of the number of layers and the thickness of one atomic layer: $H = Nh_0$. Because it is difficult to give preference to one of the formulated definitions, we define nanocrystal thickness as [4]

$$H \stackrel{\text{def}}{=} N_* h_0, \quad N - 1 \le N_* \le N, \tag{8}$$

where N_* is a dimensionless parameter reflecting the ambiguity in the determination of H. As is shown in [4], the Young's modulus E_1 corresponding to extension along the x axis of a single-crystal strip, which is infinite in this direction, is calculated by the formula

$$E_1 = \frac{N}{N_*}E_\infty, \quad E_\infty = \frac{2C}{\sqrt{3}}. \tag{9}$$

Here, E_∞ is the Young's modulus of the infinite crystal [9, 10]. It should be noted that we consider a strip finite along the x axis. However, the number of atomic layers along this direction is assumed to be so large that Eq. (9) can be used. Using Eqs. (8) and (9), we express bending stiffness (7) of the single-crystal strip in terms of its macroscopic parameters:

$$D = \frac{E_1 H^3 (N^2 - 1)}{12 N_*^2}. \tag{10}$$

Experimental data indicate that the bending stiffness of a single-layer strip is 25 times lower than the value obtained by the formula of elasticity theory [11]. Indeed, a single-layer chain of atoms must have no bending stiffness from the classical viewpoint. Therefore, it should be considered that the most acceptable values of N_* in bending problems are those for which the bending stiffness D vanishes at $N = 1$ (a low experimentally observed bending stiffness is associated with the effects ignored in the model under consideration). We consider two N_*-values satisfying the above condition.

First, we assume that $N_* = N$. In this case, $E_1 = E_\infty$ and bending stiffness is defined by the formula

$$D = D_\infty\left(1 - \frac{1}{N^2}\right), \quad D_\infty = \frac{E_\infty H^3}{12}, \quad H = Nh_0. \quad (11)$$

Here, D_∞ is the bending stiffness of the strip known from macroscopic elasticity theory. According to Eq. (11), the bending stiffness of the nanocrystal varies within the interval $0 \leq D \leq D_\infty$. For small N, this stiffness substantially depends on the number of atomic layers. It increases with N and tends to its elasticity-theory value for $N \longrightarrow \infty$.

On the other hand, we assume that

$$N_* = N\left(1 - \frac{1}{N^2}\right)^{1/3}.$$

The parameter N_* introduced in such a way satisfies inequality (8): $N - 1 \leq N_* \leq N$. In this case, the bending stiffness and the thickness of the nanocrystal are expressed as

$$D = \frac{E_\infty H^3}{12} \equiv D_\infty, \quad H = Nh_0\left(1 - \frac{1}{N^2}\right)^{1/3}. \quad (12)$$

It is easy to see that the expression for bending stiffness exactly coincides with the elasticity-theory expression. The strip-thickness expression coincides, for large N, with Nh_0 corresponding to the previous case. For small N, Eq. (12) gives thickness values lower than Nh_0; for $N = 1$, it vanishes as it must according to the concept that a single-atom layer has zero bending stiffness.

An alternative way of determining bending stiffness is to solve the problem of the deformation of a single-crystal strip upon its bending into a ring. This problem can be considered as linear in strains; however, it is geometrically nonlinear in displacements. An advantage of this formulation is the fact that it requires no assumptions about the nature of the external load. The expressions for bending stiffness D obtained as a result of solving the similar problem coincide exactly with Eqs. (10)–(12).

The problem of determining the bending stiffness of nanotubes was considered in the quasi-continuum formulation in [5], where, for several particular N-values, a strip bending stiffness which coincided with the results calculated by Eq. (11) was determined. Strip thickness was defined in [5] as $H = h_0N$, which is responsible for the discrepancy between bending stiffness and its elasticity-theory value. However, as was shown above, the application of the alternative definition of plate thickness makes it possible to use the macroscopic formula for bending stiffness without any modifications.

ACKNOWLEDGMENTS

REFERENCES

1. D. L. Bykov and D. N. Konovalov, in *Proceedings of XXXVI International Seminar on Actual Problems of Strength, Vitebsk, 2000*, pp. 428–433.

2. Yu. P. Baĭdarovtsev, G. N. Savenkov, and V. A. Tarasenko, Vysokomol. Soedin., Ser. A **41**, 1302 (1999).

3. J. J. Kim, H. A. Marzouk, C. C. Eloi, and J. D. Robertson, J. Appl. Phys. **78** (1), 245 (1995).

4. A. M. Krivtsov and N. F. Morozov, Dokl. Akad. Nauk **381** (3), 825 (2001) [Dokl. Phys. **46**, 825 (2001)].

5. C. Q. Ru, Phys. Rev. B **62** (15), 9973 (2000).

6. C. Q. Ru, Phys. Rev. B **62** (15), 10405 (2000).

7. C. Q. Ru, J. Appl. Phys. **87**, 7227 (2000).

8. V. Ya. Prinz, A. V. Chehovskiy, and L. A. Nenasheva, in *Proceedings of VII International Symposium on Nanostructures: Physics and Technology, St. Petersburg, 1999*, pp. 481–484.

9. A. M. Krivtsov, Tr. S.-Peterb. Gos. Tekh. Univ. **443**, 9 (1992).

10. A. M. Krivtsov, Z. Angew. Math. Mech. **79** (2), 419 (1999).

11. B. I. Yakobson, C. J. Brabec, and J. Bernholc, Phys. Rev. Lett. **76**, 2511 (1996).

Translated by V. Bukhanov

============== **MECHANICS** ==============

Exact Nonlinear Theory of Tension and Torsion of Helical Springs

L. M. Zubov

Presented by Academician V.A. Babeshko March 12, 2002

The problem of helical-spring loading by a longitudinal force and a torque that are applied at a point of the spring axis and directed along this axis is considered on the basis of the exact three-dimensional equations of nonlinear elasticity theory. This three-dimensional problem of nonlinear elastostatics is reduced to a two-dimensional boundary value problem for the plane region of the spring-coil cross section. A solution to the two-dimensional problem allows the equilibrium equations in the bulk of the body and boundary conditions at the lateral spring surface to be satisfied. The nonlinear theory of the torsion and tension of prismatic elastic bodies was developed earlier in [1, 2]. Within the scope of linear three-dimensional elasticity theory, the problem of a spring was investigated in [3].

1. We consider an elastic body that initially has the shape of a helical spring of an arbitrary cross section. The body is formed by the helical motion of a plane figure σ along the x_3 axis, where the figure is situated in a plane involving the x_3 axis. An equation of the contour $\partial\sigma$ bounding the region σ is presented in the parametric form $\rho = \rho(t)$, $\xi = \xi(t)$, where ρ and ξ are distances measured from and along the x_3 axis, respectively. The helical surface formed by the helical motion of the curve $\partial\sigma$ along the x_3 axis is called the lateral spring surface. We describe the deformation of an elastic medium in the nonorthogonal curvilinear Lagrangian coordinates ρ, φ, and ξ related to the Cartesian coordinates of the initial configuration x_1, x_2, and x_3 by

$$x_1 = \rho\cos\varphi, \quad x_2 = \rho\sin\varphi, \quad x_3 = \xi + \mu\varphi. \quad (1)$$

Here, μ is a real number characterizing the inclination of spring coils to the plane $x_1 x_2$. At $\mu = 0$, this coordinate system turns into the system of circular cylindrical coordinates ρ, φ, and x_3. Considering the parameters t and φ as the Gaussian coordinates of the surface, we

write the equation of the lateral spring surface in the form

$$\mathbf{r}(t, \varphi) = \rho(t)(\mathbf{i}_1\cos\varphi + \mathbf{i}_2\sin\varphi) + \xi(t)\mathbf{i}_3 + \mu\varphi\mathbf{i}_3. \quad (2)$$

Here, $\mathbf{r} = x_m\mathbf{i}_m$ is the radius vector of a surface point and $\mathbf{i}_m$ ($m = 1, 2, 3$) are the constant basis vectors of the Cartesian coordinates. Equation (2) allows the unit vector normal to the lateral surface to be found as ($s = 1, 2, 3$)

$$\mathbf{n} = \frac{-\rho\xi'\mathbf{g}_1 - \mu\rho'\mathbf{g}_2 + \rho\rho'\mathbf{g}_3}{\sqrt{(\rho\xi')^2 + (\mu\rho')^2 + (\rho\rho')^2}} = n_s(t)\mathbf{g}_s, \quad (3)$$

$$\mathbf{g}_1 = \mathbf{i}_1\cos\varphi + \mathbf{i}_2\sin\varphi,$$
$$\mathbf{g}_2 = -\mathbf{i}_1\sin\varphi + \mathbf{i}_2\cos\varphi, \quad \mathbf{g}_3 = \mathbf{i}_3, \quad (4)$$

where a prime in Eq. (3) denotes a derivative with respect to the variable t. In the problem considered below, the stress–strain state is identical for all spring coils. Therefore, it is possible to take $0 \le \varphi \le 2\pi$.

2. In the absence of mass forces, a static state of a nonlinear elastic medium is described by the equilibrium equation for stresses [4]

$$\operatorname{div}\mathbf{D} = 0, \quad (5)$$

the equations of state

$$\mathbf{D} = \mathbf{P} \cdot \mathbf{C}, \quad \mathbf{P} = 2\frac{dW}{d\mathbf{G}}, \quad (6)$$

and the geometric relations

$$\mathbf{G} = \mathbf{C} \cdot \mathbf{C}^T, \quad \mathbf{C} = \operatorname{grad}\mathbf{R},$$
$$\mathbf{R} = X_k\mathbf{i}_k, \quad X_k = x_k + u_k. \quad (7)$$

Here, div and grad are the divergence and gradient in the Lagrangian coordinates; $\mathbf{C}$ is the strain gradient; X_k ($k = 1, 2, 3$) are the Cartesian coordinates of particles of a deformed body (Eulerian coordinates); u_k are the components of the displacement field; $\mathbf{G}$ is the Cauchy

Rostov State University,
ul. Zorge 5, Rostov-on-Don, 344104 Russia

strain measure; $\mathbf{D}$ is the asymmetric Piola stress tensor; $\mathbf{P}$ is the symmetric Kirchhoff stress tensor; and $W(\mathbf{G})$ is the specific potential strain energy.

For an elastic body with the shape described above, we consider the following two-parameter family of finite strains:

$$X_1 = \alpha(\rho, \xi)\cos\kappa\varphi - \beta(\rho, \xi)\sin\kappa\varphi,$$
$$X_2 = \alpha(\rho, \xi)\sin\kappa\varphi + \beta(\rho, \xi)\cos\kappa\varphi, \qquad (8)$$
$$X_3 = \gamma(\rho, \xi) + \nu\varphi,$$

where κ and ν are real constants. For the strain of form (8), the lateral surface of the considered helical spring remains helical. However, both the diameter and inclination of the coils vary, and the azimuthal cross section σ of a spring coil, i.e., its section by the half-plane $\varphi = $ const, undergoes deformation described by the two-variable functions α, β, and γ.

At $\kappa < 0$, the spring is turned inside out; i.e., the circular ring that represents the projection of the spring body on the plane $x_1 x_2$ is turned inside out so that the inner and outer circles of the ring exchange places.

According to Eqs. (1), (4), and (7), the tensor fields of both the strain gradient and the Cauchy strain measure, which correspond to the displacement field (8), have the form

$$\mathbf{C}(\rho, \xi, \varphi) = C_{sk}(\rho, \xi)\mathbf{g}_s \otimes \mathbf{d}_k,$$
$$\mathbf{d}_1 = \mathbf{i}_1\cos\kappa\varphi + \mathbf{i}_2\sin\kappa\varphi,$$
$$\mathbf{d}_2 = -\mathbf{i}_1\sin\kappa\varphi + \mathbf{i}_2\cos\kappa\varphi, \qquad (9)$$
$$\mathbf{d}_3 = \mathbf{i}_3;$$

$$C_{11} = \frac{\partial\alpha}{\partial\rho}, \quad C_{12} = \frac{\partial\beta}{\partial\rho}, \quad C_{13} = \frac{\partial\gamma}{\partial\rho},$$

$$C_{21} = -\frac{1}{\rho}\left(\kappa\beta + \mu\frac{\partial\alpha}{\partial\xi}\right),$$
$$\qquad\qquad (10)$$
$$C_{22} = \frac{1}{\rho}\left(\kappa\alpha - \mu\frac{\partial\beta}{\partial\xi}\right), \quad C_{23} = \frac{1}{\rho}\left(\nu - \mu\frac{\partial\gamma}{\partial\xi}\right),$$

$$C_{31} = \frac{\partial\alpha}{\partial\xi}, \quad C_{32} = \frac{\partial\beta}{\partial\xi}, \quad C_{33} = \frac{\partial\gamma}{\partial\xi};$$

$$\mathbf{G} = G_{sk}(\rho, \xi)\mathbf{g}_s \otimes \mathbf{g}_k, \quad G_{sk} = C_{sm}C_{km}. \qquad (11)$$

It is further assumed that, being considered as a function of the components G_{sk} of the Cauchy strain measure in the orthonormal basis $\mathbf{g}_m$, the elastic-material specific energy W does not explicitly depend on the coordinate φ but can depend on the coordinates ρ and ξ: $W = W(G_{sk}, \rho, \xi)$. Such materials will be called uni-

form in the coordinate φ. Along with certain anisotropic media, this class of materials includes isotropic elastic media with arbitrary nonuniformity in the coordinates ρ and ξ, which are taken in the plane of the azimuthal cross section σ.

According to Eqs. (10) and (11), the quantities G_{sk} are independent of the coordinate φ. Therefore, Eqs. (6) indicate that, for a material uniform in the coordinate φ, the components $P_{sk} = \mathbf{g}_s \cdot \mathbf{P} \cdot \mathbf{g}_k$ of the Kirchhoff stress tensor depend only on the two coordinates ρ and ξ. Therefore, for a strain of form (8), the Piola stress tensor is written as

$$\mathbf{D}(\rho, \xi, \varphi) = D_{sk}(\rho, \xi)\mathbf{g}_s \otimes \mathbf{d}_k. \qquad (12)$$

Substituting Eq. (12) into Eq. (5), we arrive at the following scalar form of equilibrium equations for the Piola stresses:

$$\frac{\partial D_{11}}{\partial\rho} + \frac{1}{\rho}\left(D_{11} - \kappa D_{22} - \mu\frac{\partial D_{21}}{\partial\xi}\right) + \frac{\partial D_{31}}{\partial\xi} = 0,$$

$$\frac{\partial D_{12}}{\partial\rho} + \frac{1}{\rho}\left(D_{12} + \kappa D_{21} - \mu\frac{\partial D_{22}}{\partial\xi}\right) + \frac{\partial D_{32}}{\partial\xi} = 0, \quad (13)$$

$$\frac{\partial D_{13}}{\partial\rho} + \frac{1}{\rho}\left(D_{13} - \mu\frac{\partial D_{23}}{\partial\xi}\right) + \frac{\partial D_{33}}{\partial\xi} = 0.$$

Taking into account the equations of state (6) and Eqs. (10) and (11), one can see that Eqs. (13) are a system of three scalar equations for the three two-variable functions $\alpha(\rho, \xi)$, $\beta(\rho, \xi)$, and $\gamma(\rho, \xi)$. According to Eqs. (3) and (12), the boundary conditions on the lateral spring surface, which is assumed to be unloaded, are

$$n_s D_{sk} = 0, \quad k = 1, 2, 3. \qquad (14)$$

Expression (3) shows that the components n_s of the normal vector are independent of the coordinate φ. Therefore, boundary conditions (14) do not contain the variable φ and, together with equilibrium equations (13), form the two-dimensional boundary value problem for the plane region σ. Thus, assumptions (8) concerning the character of the deformation of an elastic medium reduce the initial three-dimensional nonlinear problem of a helical spring to the two-dimensional boundary-value problem for the plane region σ presented by the azimuthal cross section of a spring coil.

Let $\alpha_0(\rho, \xi)$, $\beta_0(\rho, \xi)$, and $\gamma_0(\rho, \xi)$ be a solution to the boundary value problem (13), (14). Then, the functions

$$\alpha = \alpha_0\cos K - \beta_0\sin K, \quad \beta = \alpha_0\sin K + \beta_0\cos K,$$

$$\gamma = \gamma_0 + L, \quad K, L = \text{const}$$

also satisfy both Eqs. (13) and boundary conditions (14); i.e., the position of the elastic body after deformation is

determined up to both rotation about and translation along the x_3 axis. This solution nonuniqueness can be removed by imposing the additional conditions

$$\iint_{\sigma} [\gamma(\rho, \xi) - \xi] d\rho \, d\xi = 0,$$

$$\iint_{\sigma} [\cos\Phi - 1] d\rho \, d\xi = 0, \qquad (15)$$

$$\cos\Phi = \frac{\dfrac{\partial\alpha}{\partial\xi} + \dfrac{\partial\beta}{\partial\rho}}{\sqrt{\left(\dfrac{\partial\alpha}{\partial\xi} + \dfrac{\partial\beta}{\partial\rho}\right)^2 + \left(\dfrac{\partial\beta}{\partial\xi} - \dfrac{\partial\alpha}{\partial\rho}\right)^2}}$$

on the desired functions.

3. A solution to the two-dimensional boundary value problem (13)–(15) formulated in the plane region σ exactly satisfies both the equilibrium equations in the body bulk and the boundary conditions at its lateral surface. In addition, by fitting the constants κ and ν, the boundary conditions specified at the ends of a spring can be satisfied approximately, i.e., in the Saint-Venant integral sense. For this purpose, considering a spring deformed according to (8), we determine the resultant force **F** and resultant moment **M** both applied to an arbitrary azimuthal cross section $\varphi = \text{const}$ of a spring coil. Taking account of Eq. (12) and the fact that the lateral surface of the body is unloaded, we obtain

$$\mathbf{F}(\varphi) = \iint_{\sigma} \mathbf{g}_2 \cdot \mathbf{D} d\rho \, d\xi = F_k \mathbf{d}_k,$$

$$F_k = \iint_{\sigma} D_{2k} d\rho \, d\xi = \text{const}. \qquad (16)$$

The condition of equilibrium of an arbitrary spring-coil segment bounded by the half-planes $\varphi = \varphi_1$ and $\varphi = \varphi_2$ has the form $\mathbf{F}(\varphi_1) = \mathbf{F}(\varphi_2)$, which leads to the relations $F_1 = F_2 = 0$ and $\mathbf{F} = F_3 \mathbf{i}_3$. Therefore, the resultant force is parallel to the X_3 axis, so that the resultant force moment is independent of a position of the axial point used for its determination. Calculating the moment

with respect to the point $X_1 = X_2 = X_3 = 0$, we derive the expressions

$$\mathbf{M}(\varphi) = -\iint_{\sigma} \mathbf{g}_2 \cdot \mathbf{D} \times \mathbf{R} d\rho \, d\xi = M_k \mathbf{d}_k,$$

$$M_1 = \iint_{\sigma} (D_{23}\beta - D_{22}\gamma) d\rho \, d\xi,$$

$$M_2 = \iint_{\sigma} (D_{21}\gamma - D_{23}\alpha) d\rho \, d\xi, \qquad (17)$$

$$M_3 = \iint_{\sigma} (D_{22}\alpha - D_{21}\beta) d\rho \, d\xi.$$

According to Eqs. (12) and (17), the quantities M_k ($k = 1, 2, 3$) are constant. The balance of the moments of all forces applied to the spring-coil segment bounded by the sections $\varphi = \varphi_1$ and $\varphi = \varphi_2$ leads to the relations $M_1 = M_2 = 0$ and $\mathbf{M} = M_3\mathbf{i}_3$. Thus, to realize strain (8), the system of forces applied to spring ends must be statically equivalent to the force and moment that are applied to a point of the spring axis and directed along this axis. After solving the two-dimensional boundary value problem (13)–(15), the force and moment become known functions of the parameters ν and κ:

$$F_3 = F(\nu, \kappa), \quad M_3 = M(\nu, \kappa). \qquad (18)$$

The inversion of the functions F and M in (18) allows the parameters ν and κ to be determined for given values of both the longitudinal force F_3 and torque M_3.

4. Potential strain energy of the spring-coil segment bounded by the sections $\varphi = \varphi_1$ and $\varphi = \varphi_2$ is expressed by the formula

$$(\varphi_1 - \varphi_2)\Pi, \quad \Pi = \iint_{\sigma} \rho W d\rho \, d\xi.$$

In view of Eqs. (10) and (11), the functional Π calculated for a solution to the two-dimensional boundary value problem (13)–(15) has the form

$$\Pi(\nu, \kappa) = \iint_{\sigma} \rho W[\alpha(\rho, \xi, \nu, \kappa), \beta(\rho, \xi, \nu, \kappa), \gamma(\rho, \xi, \nu, \kappa); \nu, \kappa] d\rho \, d\xi,$$

which takes into account the fact that a solution to problem (13)–(15) depends on the parameters ν and κ. By

using equilibrium equations (13), boundary conditions (14), and Eqs. (16) and (17), one can prove the

following energy relations of the nonlinear theory of the tension and torsion of helical springs:

$$F(\nu, \kappa) = \frac{\partial \Pi(\nu, \kappa)}{\partial \nu}, \quad M(\nu, \kappa) = \frac{\partial \Pi(\nu, \kappa)}{\partial \kappa}. \quad (19)$$

ACKNOWLEDGMENTS

REFERENCES

1. L. M. Zubov, Dokl. Akad. Nauk SSSR **270** (4), 827 (1983) [Sov. Phys. Dokl. **28**, 512 (1983)].
2. L. M. Zubov and L. U. Bogachkova, J. Appl. Mech. **62** (2), 373 (1995).
3. Yu. A. Ustinov, Dokl. Akad. Nauk **345** (5), 621 (1995) [Phys. Dokl. **40**, 660 (1995)].
4. A. I. Lur'e, *Nonlinear Elasticity Theory* (Nauka, Moscow, 1980).

Translated by Yu. Verevochkin

===== **MECHANICS** =====

Energy-Based Approach to the Effect of Vascular-Wall Muscles on the Structure of the Blood-Circulation System: A Biomechanical Concept[1]

Academician I. F. Obraztsov, I. B. Bukharov, and M. A. Khanin

In this paper, an optimality criterion for the structural and functional organization of the blood-circulation system is proposed. In addition to the previously analyzed energy expenditure, an energy-based approach to functioning smooth vascular-wall muscles is also developed. In other words, the energy spent for the regulation of peripheral vascular resistance is taken into account. Much better agreement between the theoretical results and morphological data is attained. The model proposed determines the blood vascular volume depending on the vessel generation number, whereas all known optimization models use the same blood vascular volume for all generations.

Optimization models of the blood circulation system (CS) were proposed in papers by Cohn [1], Chernous'ko [2], Obraztsov and Khanin [3], and Khanin and Bukharov [4]. According to these models, the blood volume of a certain vessel generation turned out to be equal for all vessel generations except capillaries.

The goal of this paper is to explain the observed dependence of the blood volume in vessels of a certain generation on the number of this generation. The proposed model is purely phenomenological; i.e., the control mechanisms of the vascular tone are not considered.

In this study, the principle of minimum energy expenditure of the CS is formulated in the form

$$W = W_H + W_E + W_{BC} + W_V = \min, \qquad (1)$$

where W is the goal function of the CS, W_H is the power consumed by the heart, W_E is the power spent for erythrocyte generation, W_{BC} is the power spent for blood-mass transportation during locomotion, and W_V is the power consumed by the vascular-wall smooth muscles.

The energy-optimality criterion arises from the principle of the evolutionary survival in the course of natural selection. The decrease in the energy expenditure

---

[1] The article was submitted by the authors in English.

Russian State Technological University (MATI),
Orshanskaya ul. 3, Moscow, 121552 Russia

associated with functioning body organs and systems is profitable for both individual species and the population in general.

In comparison with the optimality criterion proposed previously [4], in (1) an additional term is included that accounts for the energy transformation in smooth vascular-wall muscles.

The mechanical work W_{mech} executed by smooth vascular-wall muscles for contraction is determined by the expression

$$W_{\text{mech}} = \sum_{n=0}^{N} P_n \Delta V_n,$$

where P_n is the blood pressure in the vessels of the nth generation, V_n is the blood-volume variation in these vessels, and N is the number of generations in the arterial system.

While varying peripheral vascular resistance, smooth vascular-wall muscles execute a certain work. Hence, the power consumed by these muscles is

$$W_V = \nu \frac{W_{\text{mech}}}{\eta_M} = \nu \sum_{n=0}^{N} \frac{P_n \Delta V_n}{\eta_M}, \qquad (2)$$

where η_M is the efficiency of the smooth muscles and ν is the variation frequency of the peripheral vascular resistance (vessel tone), stochastic vasomotions being not considered here.

According to the Poiseuille law,

$$P_n = R_n \dot{Q}, \qquad (3)$$

where $\dot{Q}$ is the blood flow rate and R_n is the resistance for vessels of 0th–nth generations:

$$R_n = \frac{8\mu}{\pi} \sum_{n=0}^{n} \frac{l_n}{r_n^4 m^n}. \qquad (4)$$

Here, l_n is the length of the nth-generation vessels, r_n is their radius, m is the branching coefficient, and μ is the

blood viscosity. Formula (4) does not allow for the local blood-flow resistance at branching points.

Substituting relationships (3) and (4) into expression (2), we obtain

$$W_V = \frac{8\mu}{r_0^4}\dot{Q}l_0\nu$$

$$\times \sum_{n=0}^{N} r_n^2 l_n m^n \varepsilon_n (2 - \varepsilon_n)(n+1)\frac{1}{\eta_M}, \qquad (5)$$

where l_0 and r_0 are the aorta length and radius, respectively, and ε_n is the strain of the nth-generation vessels.

The muscular efficiency is determined by the expression [5]

$$\eta_M = \frac{f(1-f)}{\frac{1}{2}\left(f + \frac{1}{4}\right) + 2(1-f)(1.2 + 0.2f)}. \qquad (6)$$

Here, $f = \dfrac{F}{F_0}$, and F and F_0 are the forces developed by a muscle in the case of its isotonic and isometric contraction, respectively.

The results obtained by Hill for a skeletal muscle are also applicable to a smooth muscle [6]. The dimensionless parameter f in expression (6) completely determines the muscular efficiency in the case of the isotonic contraction, and the efficiency η_M is approximated by a parabolic function

$$\eta_M = cf + df^2, \quad 0 \le f < 1, \qquad (7)$$

where c and d are certain constants.

In order to determine the parameter f, the stress distribution throughout the vascular wall needs be known. This distribution is described by equilibrium equations, by continuity equations, and by Hooke's law [7].

The Lamé problem is solved for a vascular wall after the muscle contraction has occurred and equilibrium has been attained:

$$\frac{d\sigma_r}{dr} + \frac{\sigma_r - \sigma_\varphi}{r} = 0, \quad \frac{d(r\varepsilon_\varphi)}{dr} = \varepsilon_r,$$

$$\varepsilon_r = \frac{1}{E}\sigma_r - \frac{1}{2E}\sigma_\varphi + \frac{1}{2}\varepsilon_n, \quad \varepsilon_\varphi = \frac{1}{E}\sigma_\varphi - \frac{1}{2E}\sigma_r - \varepsilon_n. \qquad (8)$$

Here, ε_r and ε_φ are the radial and tangential strains, σ_r and σ_φ are the radial and tangential stresses, and E is the Young's modulus.

The boundary conditions are

$$\sigma_r\big|_{r=r_n} = -P_n, \quad \sigma_r\big|_{r=r_n+\delta_n} = 0, \qquad (9)$$

where δ_n is the wall thickness for the nth-generation vessels.

Solving Eqs. (8) in combination with (9) with respect to σ_φ, we find

$$\sigma_\varphi = \frac{1}{2}E\varepsilon_n + \frac{1}{\gamma_n(2+\gamma_n)}$$

$$\times [P_n - E\varepsilon_n(1+\gamma_n)^2\ln(1+\gamma_n)] + E\varepsilon_n\ln\frac{r}{r_n}$$

$$+ \frac{(1+\gamma_n)^2}{\gamma_n(2+\gamma_n)\left(\dfrac{r}{r_n}\right)^2}[P_n + E\varepsilon_n\ln(1+\gamma_n)], \qquad (10)$$

where $\gamma_n = \dfrac{\delta_n}{r_n}$.

Using solution (10) and averaging it over r, we arrive at

$$\bar{f} = \frac{\bar{\sigma}_\varphi}{\sigma_0} = A\varepsilon_n + B\left(\frac{2+\gamma_n-\varepsilon_n}{\gamma_n}\right)(n+1), \qquad (11)$$

where σ_0 is the isometric stress,

$$A = \frac{1}{2}\frac{E}{\sigma_0}, \quad B = \frac{4\mu}{\pi}\frac{\dot{Q}l_0}{r_0^4\sigma_0}.$$

Thus, the goal function of the CS takes the form

$$W = \frac{8\mu}{\pi}\frac{\dot{Q}^2}{\eta_H}\sum_{n=0}^{N}\frac{l_n}{r_n^4 m^n}$$

$$+ \pi\left(\alpha\frac{W_0}{V_B} + \beta\frac{c_e}{T_e}\right)\sum_{n=0}^{N} r_n^2 l_n m^n$$

$$+ \frac{8\mu\nu\dot{Q}l_0}{r_0^4}\sum_{n=0}^{N} r_n^2 l_n m^n \varepsilon_n(2-\varepsilon_n)\frac{(n+1)}{\eta_M} = \min. \quad (12)$$

In solving optimization problem (12), the constraint for a relative variation in the total peripheral vascular resistance K should be taken into account in accordance with the physiological data of [8]:

$$\frac{R}{R^*} = K, \qquad (13)$$

where R is the total peripheral vascular resistance in the quiescent state and R^* is the total peripheral vascular resistance during maximal exertion.

In order to minimize goal function (12) with allowance for constraints (13), the Lagrange multiplier technique is used.
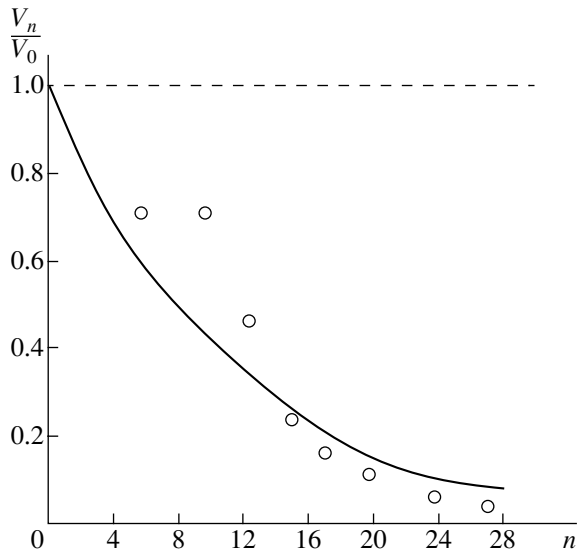
Vascular blood volume V_n as a function of the generation number n. Solid and dotted lines are the calculated dependences (with and without allowance for the energy transformations in vascular-wall vessels, respectively). Circles correspond to the experimental data of [15].

The optimal structural parameters r_n, γ_n, ε_n, and the Lagrange multiplier λ are determined by the expressions

$$r_{n_{\mathrm{opt}}} = \left[\frac{F}{G + \dfrac{H(n+1)^2}{1 - \xi(n+1)^2}} \right]^{1/6} m^{-n/3},$$

$$\gamma_{n_{\mathrm{opt}}} = p(n+1), \quad \varepsilon_{n_{\mathrm{opt}}} = q(n+1), \tag{14}$$

$$\lambda = D\frac{(N+1)(N+2)}{A(K-1)c},$$

where

$$D = 8\mu\nu\frac{\dot{Q}l_0^2}{r_0^2}, \quad F = \frac{16\mu}{\pi}\frac{\dot{Q}^2}{\eta_H}, \quad G = \pi\left(\alpha\frac{W_0}{V_B} + \beta\frac{c_e}{T_e}\right),$$

$$H = -\frac{64d}{c^2}\frac{\mu\nu\dot{Q}l_0 q}{r_0^4},$$

$$p = -4\frac{d}{c}B, \quad q = \frac{1}{2}\frac{K-1}{N+2}, \quad \xi = \frac{1}{4}q^2.$$

Knowing $r_{n_{\mathrm{opt}}}$, we can determine the optimal blood volume in nth-generation vessels.

The following numerical values of the model parameters for a human body were taken in the calculations: $E = 1 \times 10^4$ Pa, $K = 5$, $\dot{Q} = 1.3 \times 10^{-4}$ m^3 s^{-1}, $T_e = 1.7 \times 10^5$ s, $V_B = 7.5 \times 10^{-2}$ m^3, $W_0 = 83.7$ W, $c = 0.5$, $c_e = 4.5 \times 10^{15}$ m^{-3}, $d = -0.4$, $l_0 = 0.45$ m, $r_0 = 8 \times 10^{-3}$ m, $\alpha = 0.7$, $\beta = 1.310 \times 10^{-6}$ J, $\eta_H = 0.35$, $\mu = 3.6 \times 10^{-2}$ P, $\nu = 0.8$ Hz, $\sigma_0 = 2.9 \times 10^5$ Pa [9–14].

The optimal vascular blood volume as a function of the generation number is shown in the figure along with the experimental data of [15]. With allowance for the vascular-wall energy transformation, the theoretical results are in good agreement with experimental data. As seen in the figure, the effect of the vascular-wall energy transformation is most pronounced in terminal generations.

Thus, a decrease in the blood volume in terminal-generation vessels (except capillaries) reduces the energy consumed by the blood circulation system, provided that the energy requirements for the contraction of the vascular-wall smooth muscles are taken into account.

REFERENCES

1. D. Cohn, Bull. Math. Biophys. **16**, 59 (1954).
2. F. L. Chernous'ko, Prikl. Mat. Mekh. **41**, 376 (1977).
3. I. F. Obraztsov and M. A. Khanin, *Optimal Biomechanical Systems* (Meditsina, Moscow, 1989).
4. M. A. Khanin and I. V. Bukharov, J. Theor. Biol. **169**, 267 (1994).
5. A. V. Hill, Proc. Phys. Soc. London, Sect. B **159**, 297 (1964).
6. P. Hellstrand and R. J. Paul, in *Vascular Smooth Muscle: Metabolic, Ionic, and Contractile Mechanisms,* Ed. by M. F. Crass and C. D. Barnes (Academic, New York, 1982), pp. 1–36.
7. L. V. Nikitin, Izv. Akad. Nauk SSSR, Ser. Mekh. Tverd. Tela, No. 3, 154 (1971).
8. E. Asmussen, in *Handbook of Physiology. Respiration* (Amer. Physiol. Soc., Washington (D. C.), 1965), Vol. 2, pp. 939–978.
9. M. Rubner, in *Handbuch Der Normalen und Pathologischen Physiologie*, Ed. by Hrsg. von A. Bethe, G. von Bergmann, G. Embden, and A. Ellinger (Springer, Berlin, 1928), Vol. 5, pp. 17–27.
10. P. L. Altman, *Handbook of Circulation* (Saunders, Philadelphia, 1959).
11. R. J. Bing, Physiol. Rev. **45**, 171 (1965).
12. R. F. Tuma and M. P. Wiedeman, Bibl. Anat. **20**, 532 (1981).
13. P. F. Dillon and R. A. Murphy, Am. J. Physiol. **242**, 102 (1982).
14. R. H. Peters, *The Ecological Implications of Body Size* (Cambridge Univ. Press, Cambridge, 1983).
15. A. S. Iberall, Math. Biosci. **1**, 375 (1967).

<center>═══════ MECHANICS ═══════</center>

Pyramid Indentation into an Ideal Plastic Half-Space[1]

D. D. Ivlev*, Academician A. Yu. Ishlinskiĭ**, and R. I. Nepershin***

Received March 26, 2002

This paper deals with a self-similar solution to the problem of the indentation of regular square and triangular pyramids into an ideal plastic half-space. When deriving a solution, the full-plasticity condition for the Tresca yield criterion (Haar–Karman hypothesis) is used. The contact friction on pyramid faces is taken into account. The problem models the testing of hardened materials by rigid-pyramid indentation. The pressure on a pyramid and the shape of a plastic print are in reasonable agreement with experimental data. Results for modeling tests of materials by spherical indenters were presented in [1, 2].

We consider the problem of indentation of regular square and triangular pyramids into an ideal plastic half-space along the normal direction to the surface forming the half-space boundary. We introduce the Cartesian coordinate system $\{x, y, z\}$ with its z axis directed along the normal to this surface and along the pyramid axis. The direction of the x axis coincides with the normal to the middle point of a side of the square or a regular triangle that form the pyramid base on the half-space boundary $z = 0$ (Fig. 1).

In the case of regular pyramid indentation, the plastic-flow region has symmetry planes orthogonal to the half-space boundary. These planes pass through the pyramid edges and the face middle points. We consider the plastic region constrained by two symmetry planes, by a pyramid face, and by the half-space boundary. The Cartesian coordinates x, y, z, stresses, and displacement velocities are taken as dimensionless variables. In this case, we take the half-length of a side of a square or a regular-triangle base as a characteristic length. We also take the uniaxial compression yield stress of the plastic material as a characteristic stress and the pyramid

indentation velocity as a characteristic displacement velocity.

The full-plasticity condition for the pyramid-indentation problem in the space of principal stresses has the form

$$\sigma_1 = \sigma_2, \quad \sigma_3 = \sigma_1 - 1, \quad \sigma = \sigma_1 - \frac{1}{3}, \quad (1)$$

where σ is the mean stress.

We assume that the velocity vector of the plastic flow lies in the planes $y = \mathrm{const}$ orthogonal to the pyramid face and to the half-space boundary. This assumption is true for the symmetry plane $y = 0$ because of the symmetry condition for the plastic flow. For the planes $0 < y < 1$, this assumption ensures the geometric similarity of the plastic flow during pyramid indentation for all cross sections $y = \mathrm{const}$. For $y = 1$, the plastic region ahead of the pyramid face is reduced to the point that coincides with the point of the pyramid-edge intersection with the boundary $z = 0$ of the half-space. This is confirmed by the experiments with pyramidal indenters [3].
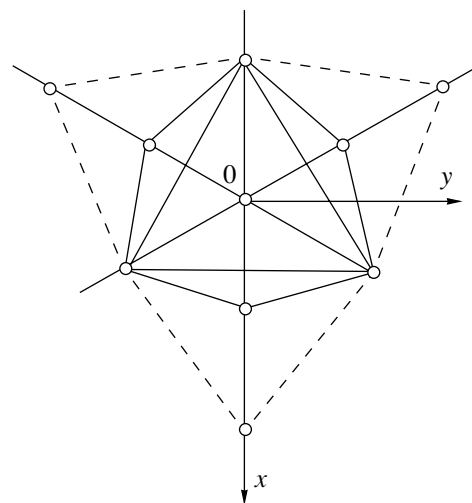

Fig. 1. Projection of a plastic print onto the plane $z = 0$ and plastic region boundaries (dashed lines) in the case of the indentation of a smooth triangle pyramid into the half-space $z \leq 0$.

---

[1] The article was submitted by the authors in English.

  * Yakovlev Chuvash State Pedagogical University,
    ul. Karla Marksa 38, Cheboksary, 428000 Russia

 ** Institute for Problems in Mechanics,
    Russian Academy of Sciences,
    pr. Vernadskogo 101, Moscow, 117526 Russia

*** Moscow State Academy of Instrument Engineering
    and Informatics,
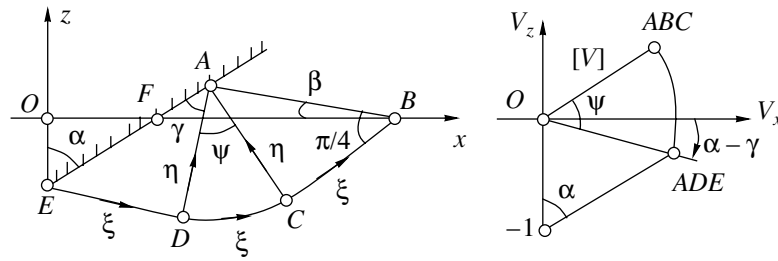   ul. Stromynka 20, Moscow, 107846 Russia
    E-mail: nepershin_r@pop.mtu.ru

Fig. 2. Slip-line field and the displacement-velocity hodograph in the plane $y = $ const.

The direction cosines of the stress σ_3 with the coordinate axes x, y, z are given by the relations

$$n_1 = \cos\theta, \quad n_2 = 0, \quad n_3 = \sin\theta,$$

where θ is the angle between the direction of the stress σ_3 and the x axis. Under condition (1), the nonzero components of the stress tensor are

$$\sigma_x = \sigma + \frac{1}{3} - \cos^2\theta, \quad \sigma_y = \sigma + \frac{1}{3},$$

$$\sigma_z = \sigma + \frac{1}{3} - \sin^2\theta, \tag{2}$$

$$\tau_{xz} = -\sin\theta\cos\theta. \tag{3}$$

In the planes $y = $ const, the direction of the principal stress $\sigma_2 = \sigma_y$ is parallel to the y axis. The slip lines ξ and η are defined by the differential equations

$$\frac{dz}{dx} = \tan\varphi \text{ for } \xi, \quad \frac{dz}{dx} = -\cot\varphi \text{ for } \eta. \tag{4}$$

In this case, the differential relations for stresses and displacement velocities coincide with Hencky's and Geiringer's equations [4]:

$$d\sigma - d\varphi = 0 \text{ along } \xi, \quad d\sigma + d\varphi = 0 \text{ along } \eta, \tag{5}$$

$$dV_\xi - V_\eta d\varphi = 0 \quad \text{along } \xi,$$

$$dV_\eta + V_\xi d\varphi = 0 \quad \text{along } \eta, \tag{6}$$

where φ is the angle between the tangent to the slip line ξ and the x axis and V_ξ and V_η are the projections of the velocity vector on the slip lines. The angles φ and θ are related to each other by the formula $\theta = \varphi - \frac{\pi}{4}$.

We now consider the plastic region and the boundary conditions of the problem in the plane $y = $ const (Fig. 2). The depth h of the pyramid indentation is defined by the relations

$$h = \frac{1-y}{\sqrt{3}\tan\alpha} \text{ or } h = \frac{1-y}{\tan\alpha}, 0 \le y \le 1, \tag{7}$$

for the triangular or square pyramid, respectively, where α is the angle of the pyramid-face inclination to the z axis. The normal and shear stresses are constant on the contact boundary AE. In the region ADE, the slip

lines are rectilinear and the stress state is homogeneous. In the region ACD, the rectilinear slip lines η form a centered fan with a singular point A. In the region ABC, the stress state is also homogeneous, and the boundary AB is free from the external normal stresses and shear stresses.

Under the full-plasticity condition, the material of the plastic region ABC is in the uniaxial compression stress state along the boundary AB:

$$\sigma_1 = \sigma_2 = 0, \quad \sigma_3 = -1, \quad \sigma = -\frac{1}{3} \quad \text{on } AB. \tag{8}$$

At the contact boundary AE, we specify the friction shear stress μ, which determines the inclination angle γ of the slip line η to the boundary AE:

$$\gamma = \frac{1}{2}\arccos 2\mu, \quad 0 \le \mu \le \frac{1}{2} \quad \text{on } AE. \tag{9}$$

The angles β and ψ are related to each other by the expression

$$\beta + \psi = \frac{\pi}{4} + \alpha - \gamma. \tag{10}$$

The angles α and μ are the problem parameters and, in accordance with the symmetry condition of the plastic flow in the z axis, must satisfy the inequality that follows from the limiting value $\frac{\pi}{2}$ of the vertex angle at the point E of the rigid region:

$$\alpha \le \frac{\pi}{4} + \frac{1}{2}\arccos 2\mu. \tag{11}$$

For a perfectly smooth pyramid $(\mu = 0)$, we have $\alpha \le \frac{\pi}{2}$, and for a completely rough pyramid $\left(\mu = \frac{1}{2}\right)$, we have $\alpha \le \frac{\pi}{4}$.

If the angle α exceeds limiting value (11), which depends on the contact friction, then a bump of the undistorted material arises on the pyramid faces. This bump forms a natural wedge with the inclination angle

$\alpha^* = \dfrac{\pi}{4}$. Afterwards, the plastic region slides along this wedge with the maximum friction shear stress. In this case, the pyramid pressure does not depend on the angle α. This is confirmed by the experiments [3] on the indentation of a rough nonlubricated square pyramid for the angles $\alpha > \dfrac{\pi}{4}$.

In order to find the angle β, we use the incompressibility condition that results in the equality of areas of the triangles *ABF* and *EOF*. Using the relation

$$\frac{h}{l} = \cos\alpha - \sqrt{2}\cos\gamma\sin\beta, \qquad (12)$$

where l is the length of the contact boundary *AE*, we arrive at the nonlinear equation in terms of the angle β

$$\sin\beta\left(\cos\beta + \frac{\sqrt{2}\sin\alpha}{\cos\gamma}\right) - \frac{1}{4}\frac{\sin 2\alpha}{\cos^2\gamma} = 0 \qquad (13)$$

with the exact solution $\beta = 0$ for $\alpha = 0$ and $\alpha = \dfrac{\pi}{2}$.

Within the range $0 < \alpha < \dfrac{\pi}{2}$, we find the angle β numerically solving Eq. (13) by Newton's iterative method. Then, we find the angle ψ and the contact-boundary length l from relations (10) and (12).

The velocity field in the region *AED* and the velocity discontinuity V at the point E and along the rigid-plastic boundary (Fig. 2) are defined by the continuity condition for the velocities normal to the pyramid face and to the rigid-plastic boundary. Equations (6) define constant velocities along the rectilinear slip lines η and rotation of the velocity discontinuity along the boundary *DC*, which is mapped on the velocity-hodograph plane by the circle arc with the radius V. From the plots shown in the velocity-hodograph plane, we find V and the velocity-vector projections onto the x and z axes:

$$V = \frac{\sin\alpha}{\cos\gamma}, \qquad (14)$$

$$V_x = [V]\cos\zeta, \quad V_z = [V]\sin\zeta,$$
$$\gamma - \alpha \leq \zeta \leq \frac{\pi}{4} - \beta. \qquad (15)$$

The average stress within the region *ADE* is found by integrating relation (5) along the slip line ξ using both the angle ψ defined by Eq. (10) and boundary condition (8):

$$\sigma = -\left(\frac{1}{3} + \frac{\pi}{4} + \alpha - \gamma - \beta\right). \qquad (16)$$

We can now find the normal pressure on the pyramid face from the first relation of formula (2) by orienting

the x axis along a normal to the pyramid face and using the angle $\theta = \gamma - \dfrac{\pi}{4}$ for the stress σ_3 and Eq. (16) for σ:

$$p = \frac{1}{2}(1 + \sin 2\gamma) + \frac{\pi}{4} + \alpha - \gamma - \beta. \qquad (17)$$

The vertical pressure related to the projection of the plastic-print area onto the plane $z = 0$ is

$$q = p + \mu\cot\alpha. \qquad (18)$$

We also find the vertical pressure related to the area of the pyramid base in the plane $z = 0$ from relationships (7), (12), and (18):

$$q_n = q\chi\sin\alpha,$$
$$\chi = (\sin\alpha - \sqrt{2}\cos\gamma\tan\alpha\sin\beta)^{-1}. \qquad (19)$$

The vertical force Q acting on the triangular and square pyramids is $\sqrt{3}\,q_n$ and $4q_n$, respectively.

We determine the height of the elevation of the plastic region on the pyramid face over the plane $z = 0$ and projection of the plastic-print boundary onto this plane from relations (7) and (12):

$$h^* = \sqrt{2}c(1-y)\chi\cos\gamma\sin\beta, \qquad (20)$$

$$x = c[y + (1-y)\chi\sin\alpha], \qquad (21)$$

where χ is defined in Eq. (19) and $c = \dfrac{1}{\sqrt{3}}$ or $c = 1$ for the triangular or square pyramids, respectively. The boundary of the plastic region in the plane $z = 0$ is defined by the relationship

$$x = c[y + (1-y)\chi(\sin\alpha + \sqrt{2}\cos\gamma\cos\beta)]. \qquad (22)$$

The boundaries of the plastic region and projections of the plastic print onto the plane $z = 0$, which were calculated from Eqs. (13), (21), and (22) for the smooth triangular pyramid with $\alpha = \dfrac{\pi}{3}$ and $\beta = 0.16$, are shown by dashed lines in Fig. 1.

The experiments performed in [3] on the indentation of triangular and square pyramids into hardened metals exhibit a linear increase in the required load and geometric similarity of the plastic-print shape. This result is consistent with the obtained self-similar solution to the problem. The predicted pressure on the projection of the plastic print in the plane $z = 0$ or the pressure related to the area of the pyramid base are the same for both the triangular and square pyramid. This conclusion is consistent with the experimental data presented in Table 1 of [3].

The results calculated according to Eqs. (20) and (21) on the elevation of the plastic region over the plane $z = 0$ and projections of the plastic print onto this plane in the cross section $y = 0$ for different angles α are in reasonable agreement with the experimental data of [3].

However, the predicted boundary of the plastic region in the cross section $y = 0$, which is calculated from Eq. (22), is considerably greater than the experimental boundary. Such a discrepancy can be explained by the rather small inclination angles of the free boundary of the plastic region to the half-space boundary. Another explanation is the existence of a smooth transition zone between the plastic-region boundary and the nondeformed boundary of the half-space. These facts can hamper the exact experimental determination of the plastic boundary.

The predicted pressures q_n as functions of the angle α, which were calculated by Eq. (19) for $\mu = 0$, 0.1, and 0.5, are compared in Fig. 3 with the experimental data of [3] on the indentation of a square pyramid with and without a lubricant into hardened copper. In this case, the stress–strain dependence is close to the model of a perfectly plastic body. The deviations of the predicted and experimental data lie within the accuracy range of the estimates for the contact friction and shear yield stress of the deformable material.
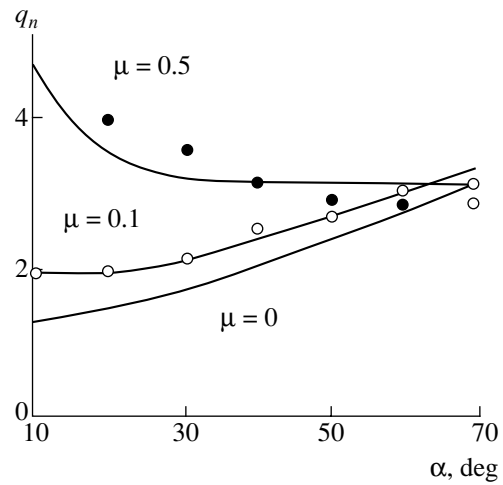
In the limiting case of $\alpha \longrightarrow \dfrac{\pi}{2}$ and $\mu = 0$, it follows from Eqs. (13) and (17)–(22) that $\beta = 0$, $q = q_n = 1 + \dfrac{\pi}{2}$, and $h^* = 0$. In this case, the print boundary coincides with the pyramid base. In addition, the plastic-region boundary in the plane $z = 0$ is determined by the equation $x = c(2 - y)$. This is the limiting case of the pressure of a smooth triangle and square flat die on a perfectly plastic half-space [4]. The limiting pressure $q \approx 1 + \dfrac{\pi}{2}$ on the lubricated square pyramid as $\alpha \longrightarrow \dfrac{\pi}{2}$, $h^* \approx 0$

Fig. 3. Pressure on the pyramid base as a function of the face inclination angle to the pyramid axis and experimental data for the lubricated ($\bigcirc$) and rough ($\bullet$) quadratic-pyramid indenters [3].

and the plastic region boundary $x \approx 2$ in the cross section $y = 0$ have been determined in the experiments of [3].

REFERENCES

1. A. Yu. Ishlinskiĭ, Prikl. Mat. Mekh. **8**, 201 (1944).

2. A. Yu. Ishlinskiĭ, *Applied Problems of Mechanics* (Nauka, Moscow, 1986), Vol. 1.

3. D. S. Dugdale, J. Mech. Phys. Solids **3**, 197 (1955).

4. D. D. Ivlev, A. Yu. Ishlinskiĭ, and R. I. Nepershin, Dokl. Akad. Nauk **381**, 616 (2001) [Dokl. Phys. **46**, 890 (2001)].

<hr>

MECHANICS

<hr>

On the Limiting Anisotropic State
of a Perfect Plastic Medium

B. G. Mironov

Presented by Academician A.Yu. Ishlinskiĭ March 18, 2002

Received March 25, 2002

A solution to the three-dimensional problem in the theory of perfect plasticity for an isotropic medium was obtained by Ishlinskiĭ [1, 4]. For the general case, the statically determinate states in this theory were found in [2]. In this study, we consider the limiting anisotropic state of a perfect plastic material.

1. The yield condition for the three-dimensional problem in the theory of perfect plasticity, in the general case, can be written in the form

$$f_k(\sigma_{ij}) = 0, \qquad (1.1)$$

where σ_{ij} are the stress-tensor components in the Cartesian xyz coordinate system.

The relationships between the principal stresses σ_i and the stress components σ_{ij} have the form

$$\sigma_{ij} = \sigma_1 l_i l_j + \sigma_2 m_i m_j + \sigma_3 n_i n_j. \qquad (1.2)$$

For the direction cosines, the relations

$$l_i l_j + m_i m_j + n_i n_j = \delta_{ij} \qquad (1.3)$$

are valid.

Using relationships (1.2), conditions (1.1) can be written in the form

$$f_k(\sigma_i, l_i, m_i, n_i) = 0. \qquad (1.4)$$

The presence of l_i, m_i, and n_i in relations (1.4) determines the directional properties and characterizes the anisotropy of a material.

We consider a case when relations (1.4) are independent of σ_i, i.e.,

$$f_k(l_i, m_i, n_i) = 0. \qquad (1.5)$$

We call a medium being described by relationship (1.5) limiting anisotropic.

*Yakovlev Chuvash State Pedagogical University,
Cheboksary, 428013 Russia*

According to [3], in the two-dimensional case, condition (1.5) has the form

$$\varphi = \text{const}, \quad \tan\varphi = \frac{2\tau_{xy}}{\sigma_x - \sigma_y}, \qquad (1.6)$$

where φ is the angle determining the direction of the first principal stress in the orthogonal xyz coordinate system. From condition (1.6), it follows that

$$(\sigma_x - \sigma_y)\cos 2\varphi - 2\tau_{xy} = 0. \qquad (1.7)$$

Condition (1.7) corresponds to the absence of shear stresses on the principal area elements.

In the general case, this condition is set in the form

$$\sigma_{12} = \sigma_x l_1 m_1 + \sigma_y l_2 m_2 + \sigma_z l_3 m_3 + \tau_{xy}(l_1 m_2 + l_2 m_1)$$
$$+ \tau_{yz}(l_2 m_3 + l_3 m_2) + \tau_{xz}(l_1 m_3 + l_3 m_1) = 0, \quad (1.8)$$
$$(123, lmn, xyz).$$

Hereafter, the symbol (123, lmn, xyz) implies that the missing equations are obtained by the cyclic permutation of 1, 2, 3, l, m, n, x, y, and z.

The three conditions (1.8), similarly to (1.7), are used below as relations that determine the behavior of the limiting anisotropic medium.

Furthermore, l_i, m_i, and n_i are assumed to be constant and independent of the coordinates x, y, and z.

Using the Maxwellian stress functions

$$\sigma_x = \frac{\partial^2 X_2}{\partial z^2} + \frac{\partial^2 X_3}{\partial y^2}, \quad \tau_{xy} = -\frac{\partial^2 X_3}{\partial x \partial y} \quad (xyz, 123), \quad (1.9)$$

we satisfy the equilibrium equations

$$\frac{\partial \sigma_x}{\partial x} + \frac{\partial \tau_{xy}}{\partial y} + \frac{\partial \tau_{xz}}{\partial y} = 0 \quad (xyz).$$

From (1.8), according to (1.9), we arrive at

$$l_3 m_3 \frac{\partial^2 X_1}{\partial y^2} - (l_2 m_3 + l_3 m_2)\frac{\partial^2 X_1}{\partial y \partial z} + l_2 m_2 \frac{\partial^2 X_1}{\partial z^2}$$

$$+ l_3 m_3 \frac{\partial^2 X_2}{\partial x^2} - (l_1 m_3 + l_3 m_1) \frac{\partial^2 X_2}{\partial x \partial z} + l_1 m_1 \frac{\partial^2 X_2}{\partial z^2}$$

$$+ l_2 m_2 \frac{\partial^2 X_3}{\partial x^2} - (l_1 m_2 + l_2 m_1) \frac{\partial^2 X_3}{\partial x \partial y} + l_1 m_1 \frac{\partial^2 X_3}{\partial y^2} = 0 \tag{1.10}$$

$$(123, lmn, xyz).$$

The characteristic surfaces $\mu(x, y, z) = C$ of system (1.10) can be found from the equations

$$l_1 \frac{\partial \mu}{\partial x} + l_2 \frac{\partial \mu}{\partial y} + l_3 \frac{\partial \mu}{\partial z} = 0 \quad (lmn). \tag{1.11}$$

The general solution to system (1.10) can be represented in the form

$$X_i = A_i X(l_1 x + l_2 y + l_3 z)$$
$$+ B_i Y(m_1 x + m_2 y + m_3 z) + C_i Z(n_1 x + n_2 y + n_3 z), \tag{1.12}$$

where the coefficients A_i, B_i, and C_i meet the relations

$$l_1 m_1 C_1 + l_2 m_2 C_2 + l_3 m_3 C_3 = 0 \quad (lmn, CAB). \tag{1.13}$$

In view of solution (1.12), it follows from (1.9) that

$$\sigma_x = (A_2 l_3^2 + A_3 l_2^2) \varphi_1(\xi)$$
$$+ (B_2 m_3^2 + B_3 m_2^2) \varphi_2(\eta) + (C_2 n_3^2 + C_3 n_2^2) \varphi_3(\zeta), \tag{1.14}$$

$$\tau_{xy} = -A_3 l_1 l_2 \varphi_1(\xi) - B_3 m_1 m_2 \varphi_{21}(\eta)$$
$$- C_3 n_1 n_2 \varphi_3(\zeta) \quad (xyz, 123), \tag{1.15}$$

where

$$\xi = l_1 x + l_2 y + l_3 z, \quad \eta = m_1 x + m_2 y + m_3 z,$$

$$\zeta = n_1 x + n_2 y + n_3 z, \quad \varphi_1(\xi) = \frac{d^2 X}{d\xi^2},$$

$$\varphi_2(\eta) = \frac{d^2 Y}{d\eta^2}, \text{ and } \varphi_3(\zeta) = \frac{d^2 Z}{d\zeta^2}.$$

The expression for the dissipation power of the mechanical energy has the form

$$N = \sigma_x \varepsilon_x + \sigma_y \varepsilon_y + \sigma_z \varepsilon_z$$
$$+ 2\tau_{xy} \varepsilon_{xy} + 2\tau_{yz} \varepsilon_{yz} + 2\tau_{xz} \varepsilon_{xz}.$$

According to (1.2),

$$N = \sigma_1 \varepsilon_1 + \sigma_2 \varepsilon_2 + \sigma_3 \varepsilon_3, \tag{1.16}$$

where

$$\varepsilon_1 = \varepsilon_x l_1^2 + \varepsilon_y l_2^2 + \varepsilon_z l_3^2 + 2\varepsilon_{xy} l_1 l_2$$
$$+ 2\varepsilon_{yz} l_2 l_3 + 2\varepsilon_{xz} l_1 l_3 \quad (xyz, lmn),$$

$$\sigma_1 = \sigma_x l_1^2 + \sigma_y l_2^2 + \sigma_z l_3^2$$
$$+ 2\tau_{xy} l_1 l_2 + 2\tau_{yz} l_2 l_3 + 2\tau_{xz} l_1 l_3 \quad (123, lmn, xyz).$$

The values of ε_1, ε_2, and ε_3 determine the deformation rates along the principal-stress components and, in the general case, do not coincide with the principal components of the strain rate.

The relationships for the associate law of plastic flow are determined from the condition for the extremum of the functional

$$A = N - \lambda_1 F_1 - \lambda_2 F_2 - \lambda_3 F_3,$$

where F_1, F_2, and F_3 are the right-hand sides of relations (1.8), and have the form

$$\varepsilon_x = \lambda_1 l_1 m_1 + \lambda_2 m_1 n_1 + \lambda_3 n_1 l_1, \tag{1.17}$$

$$2\varepsilon_{xy} = \lambda_1 (l_1 m_2 + l_2 m_1) + \lambda_2 (m_1 n_2 + m_2 n_1)$$
$$+ \lambda_3 (n_1 l_2 + n_2 l_1) \quad (123, lmn, xyz). \tag{1.18}$$

From (1.17) and (1.18), we obtain

$$\varepsilon_x + \varepsilon_y + \varepsilon_z = 0,$$

$$\varepsilon_1 = \varepsilon_x l_1^2 + \varepsilon_y l_2^2 + \varepsilon_z l_3^2 \tag{1.19}$$

$$+ 2\varepsilon_{xy} l_1 l_2 + 2\varepsilon_{yz} l_2 l_3 + 2\varepsilon_{xz} l_1 l_3 = 0 \quad (xyz, lmn, 123).$$

According to (1.8) and (1.19), we find that, along the directions of the principal stresses, the normal components of the strain rate are equal to zero.

It follows from (1.16) and (1.19) that, in the limiting anisotropic case, the dissipation power N of the mechanical energy is equal to zero due to the absence of adhesion.

Using the Cauchy formulas, we pass from the components of the strain rates to those of displacement rates:

$$\varepsilon_x = \frac{\partial u}{\partial x}, \quad \varepsilon_y = \frac{\partial v}{\partial y}, \quad \varepsilon_z = \frac{\partial w}{\partial z}, \tag{1.20}$$

$$\varepsilon_{xy} = \frac{1}{2}\left(\frac{\partial u}{\partial y} + \frac{\partial v}{\partial x}\right), \quad \varepsilon_{yz} = \frac{1}{2}\left(\frac{\partial v}{\partial z} + \frac{\partial w}{\partial y}\right),$$

$$\varepsilon_{xz} = \frac{1}{2}\left(\frac{\partial u}{\partial z} + \frac{\partial w}{\partial x}\right). \tag{1.21}$$

Then, from formulas (1.19)–(1.21), we have

$$l_1^2 \frac{\partial u}{\partial x} + l_1 l_2 \frac{\partial u}{\partial y} + l_1 l_3 \frac{\partial u}{\partial z} + l_1 l_2 \frac{\partial v}{\partial x} + l_2^2 \frac{\partial v}{\partial y}$$

$$+ l_2 l_3 \frac{\partial v}{\partial z} + l_1 l_3 \frac{\partial w}{\partial x} + l_2 l_3 \frac{\partial w}{\partial y} + l_3^2 \frac{\partial w}{\partial z} = 0 \tag{1.22}$$

$$(123, lmn, xyz).$$

The equations that make it possible to determine the characteristic surfaces $\nu(x, y, z) = C$ of system (1.22)
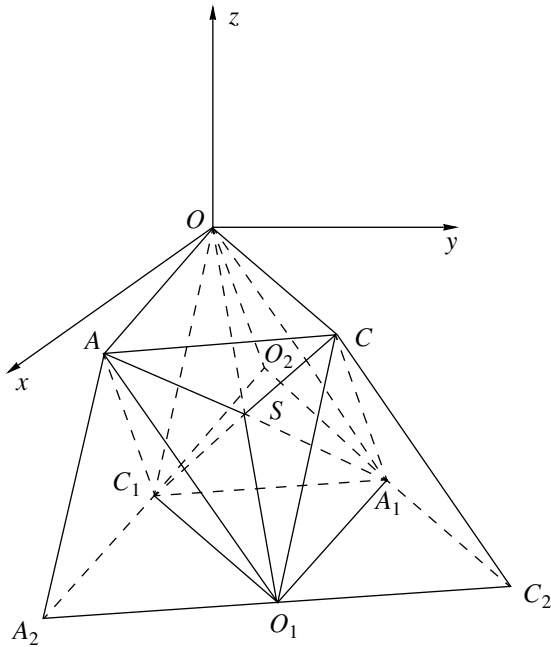
Figure.

are of the form

$$l_1 \frac{\partial v}{\partial x} + l_2 \frac{\partial v}{\partial y} + l_3 \frac{\partial v}{\partial z} = 0 \quad (lmn). \quad (1.23)$$

As is seen from Eqs. (1.11) and (1.23), the characteristic surfaces of systems (1.10) and (1.22) coincide.

The general solution to Eq. (1.22) can be written in the form

$$u = a_1 U(\xi) + b_1 V(\eta) + c_1 W(\zeta)$$
$$(uvw, xyz, 123), \quad (1.24)$$

where a_i, b_i, and c_i meet the relations

$$a_1 l_1 + a_2 l_2 + a_3 l_3 = 0,$$
$$b_1 m_1 + b_2 m_2 + b_3 m_3 = 0, \quad c_1 n_1 + c_2 n_2 + c_3 n_3 = 0. \quad (1.25)$$

2. We now consider the case when $A_1 = A_2 = A_3$, $B_1 = B_2 = B_3$, $C_1 = C_2 = C_3$, $a_i = m_i$, $b_i = n_i$, and $c_i = l_i$. Without the loss of generality, we assume that $A_i = B_i = C_i = 1$.

Then, from relationships (1.14), (1.15), and (1.24), we find

$$\sigma_x = (1 - l_1^2)\varphi_1(\xi)$$
$$+ (1 - m_1^2)\varphi_2(\eta) + (1 - n_1^2)\varphi_3(\zeta), \quad (2.1)$$

$$\tau_{xy} = -l_1 l_2 \varphi_1(\xi) - m_1 m_2 \varphi_2(\eta) - n_1 n_2 \varphi_3(\zeta)$$
$$(xyz, 123), \quad (2.2)$$

$$u = m_1 U(\xi) + n_1 V(\eta) + l_1 W(\zeta) \quad (uvw, 123). \quad (2.3)$$

We assume that, in the plane $z = 0$, stresses and displacement rates are set in the form

$$\sigma_z = p(x, y), \quad \tau_{yz} = \tau_{xz} = 0, \quad (2.4)$$

$$u = v = 0, \quad w = q(x, y). \quad (2.5)$$

According to relationships (2.1)–(2.3),

$$\sigma_x = \frac{1}{2}$$
$$\times [(1 - l_1^2)p(\xi) + (1 - m_1^2)p(\eta) + (1 - n_1^2)p(\zeta)], \quad (2.6)$$

$$\tau_{xy} = -\frac{1}{2}[l_1 l_2 p(\xi) + m_1 m_2 p(\eta) + n_1 n_2 p(\zeta)]$$
$$(xyz, 123), \quad (2.7)$$

$$u = m_1 m_3 q(\xi) + n_1 n_3 q(\eta) + l_1 l_3 q(\zeta),$$
$$v = m_2 m_3 q(\xi) + n_2 n_3 q(\eta) + l_2 l_3 q(\zeta), \quad (2.8)$$
$$w = m_3^2 q(\xi) + n_3^2 q(\eta) + l_3^2 q(\zeta).$$

Here, $p(\xi)$ and $q(\xi)$ are the continuations of the functions $p(x, y)$ and $q(x, y)$ along the planes $\xi = \xi_0$. Similarly, the same is valid for $p(\eta)$, $p(\zeta)$, $q(\eta)$, and $q(\zeta)$.

As an example, we consider the distribution of a constant pressure in the triangle AOC (see figure):

$$AO: l_1 x + l_2 y = 0, \quad OC: m_1 x + m_2 y = 0,$$

$$AC: n_1 x + n_2 y = d,$$

$$\sigma_z = p = \text{const inside the triangle } AOC$$

and $\sigma_z = 0$ outside the triangle AOC.

Then, in view of relationships (2.6) and (2.7), we have:
in the pyramid $SAOC$,

$$\sigma_x = \sigma_y = \sigma_z = p, \quad \tau_{xy} = \tau_{yz} = \tau_{xz} = 0;$$

in the pyramid $SACO_1$,

$$\sigma_x = \frac{p}{2}(1 + n_1^2), \quad \tau_{xy} = \frac{p}{2}n_1 n_2 \quad (xyz, 123);$$

in the pyramid $SAOC_1$,

$$\sigma_x = \frac{p}{2}(1 + l_1^2), \quad \tau_{xy} = \frac{p}{2}l_1 l_2 \quad (xyz, 123);$$

in the pyramid $SOCA_1$,

$$\sigma_x = \frac{p}{2}(1 + m_1^2), \quad \tau_{xy} = \frac{p}{2}m_1 m_2 \quad (xyz, 123);$$

in the zone $CSO_1C_2A_1$,

$$\sigma_x = \frac{p}{2}(1 - l_1^2), \quad \tau_{xy} = -\frac{p}{2}l_1l_2 \quad (xyz, 123);$$

in the zone $ASO_1A_2C_1$,

$$\sigma_x = \frac{p}{2}(1 - m_1^2), \quad \tau_{xy} = -\frac{p}{2}m_1m_2 \quad (xyz, 123);$$

in the zone $OSC_1O_2A_1$,

$$\sigma_x = \frac{p}{2}(1 - n_1^2), \quad \tau_{xy} = -\frac{p}{2}n_1n_2 \quad (xyz, 123).$$

In the rest of the zones, all the stress components are zero.

REFERENCES

1. A. Yu. Ishlinskiĭ, Uch. Zap. Mos. Gos. Univ., Mekhanika **117**, 90 (1946).

2. D. D. Ivlev, Dokl. Akad. Nauk **361**, 765 (1998) [Dokl. Phys. **43**, 809 (1998)].

3. M. A. Artemov and D. D. Ivlev, Mekh. Tverd. Tela, No. 3, 43 (1996).

4. A. Yu. Ishlinskiĭ, *Applied Problems in Mechanics* (Nauka, Moscow, 1986), Vol. 1, pp. 62–83.

Translated by Yu. Vishnyakov